Chemical Science

ROYAL SOCIETY OF CHEMISTRY

REVIEW

View Article Online
View Journal | View Issue

Check for updates

Cite this: *Chem. Sci.*, 2025, **16**, 18559

Towards commercialization: perspectives and challenges of solution-processed perovskite-based tandem photovoltaics

Jiaxiang Lv,†[a] Liyun Le,†[b] Shuo Yao,[a] Zengqi Huang*[a] and Yiwang Chen *[ac]

Received 15th July 2025
Accepted 8th September 2025

DOI: 10.1039/d5sc05266a

rsc.li/chemical-science

Over the past decade, single-junction perovskite solar cells (PSCs) have achieved remarkable progress, with power conversion efficiencies (PCEs) reaching 27.3% and approaching their efficiency limit. Perovskite-based tandem solar cells (PeTSCs) have garnered significant attention due to their potential to surpass the Shockley–Queisser (S–Q) limit of single-junction solar cells. Owing to their tunable bandgap, perovskite materials can serve as both narrow-bandgap rear cells or wide-bandgap front cells, enabling the formation of high-efficiency tandem architectures. However, several challenges remain in transitioning from single-junction to tandem solar cells (TSCs). This review highlights recent advances in solution-processed PeTSCs, covering the key issues from material engineering to subcell integration, including phase segregation, interface defects, energy loss, interconnection depletion, and stability. Furthermore, we discuss emerging research trends and provide insights into future challenges and commercialization prospects. Perspectives on the core aspects related to the future development of PeTSCs are provided.

1. Introduction

Photovoltaic technology has become the most promising candidate for converting light energy into electrical energy. Up to now, silicon (Si) solar cells have dominated the photovoltaic cell market on account of their high power conversion efficiency, stability, and mature large-scale production. However, inherent limitations of Si-based technologies, including rigidity, fixed bandgaps, high production costs, and energy-intensive vacuum deposition processes constrain their scalability potential. Since perovskite materials with a crystal

---

[a] Key Lab of Fluorine and Silicon for Energy Materials and Chemistry of Ministry of Education, Jiangxi Normal University, 99 Ziyang Avenue, Nanchang 330022, China. E-mail: ywchen@ncu.edu.cn; huangzq@jxnu.edu.cn

[b] National Key Laboratory of Uranium Resources Exploration-Mining and Nuclear Remote Sensing, East China University of Technology, 418 Guanglan Avenue, Nanchang 330013, China

[c] Film Energy Chemistry for Jiangxi Provincial Key Laboratory (FEC), Institute of Polymers and Energy Chemistry (IPEC), Nanchang University, 999 Xuefu Avenue, Nanchang 330031, China

† J. L. and L. L. contributed equally to this work.

Jiaxiang Lv

Jiaxiang Lv has been an MS student in Materials and Chemical Engineering at Jiangxi Normal University under the supervision of Prof. Yiwang Chen and Zengqi Huang since 2023. His research interests are perovskite/organic tandem solar cells.

Zengqi Huang

Zengqi Huang has been a professor of chemistry at Jiangxi Normal University since 2022. He received his PhD degree from Nanchang University in 2020. He then joined the Institute of Chemistry, Chinese Academy of Sciences (ICCAS) as a postdoctoral fellow and worked on green printing technology and its integration into photovoltaic devices from 2020–2022. He was a Junior Fellow of Beijing National Laboratory of Molecular Sciences. His present research interests include flexible perovskite optoelectronic devices and tandem solar cells.

structure of ABX_3 were discovered, they have garnered extensive attention due to their exceptional light absorption capabilities and easily adjustable bandgap (E_g), low-temperature solution preparation, low cost, and flexibility.[1–8] Although initial PCE stood at only 3.8%, continuous scientific research has led to substantial improvements in single-junction perovskite solar cell performance.[9] The PCE of the latest certified PSCs has reached 27.3% (Fig. 1a).[10] This rapid improvement in PCE adequately demonstrates the development potential of PSCs, and stimulates great interest from the scientific and industrial communities in the commercialization of perovskite photovoltaic technologies.

In single-junction photovoltaic devices, the primary energy loss mechanisms are attributed to sub-bandgap photon transmission and thermal relaxation of photoexcited hot carriers (Fig. 1b). Researchers have made many attempts to solve this problem, such as multiple exciton generation, hot carriers and tandem design. Among them, the most promising method is to develop tandem devices, and TSCs have also been proven to have better practical performance potential than the S–Q limit (33.7%) (Fig. 1c).[11,12]

The operational principle of perovskite-based tandem solar cells is founded on a strategy of spectral complementarity and electrical collaboration.[13] Through the monolithic integration of sub-cells possessing distinct bandgaps, the solar spectrum can be harnessed more effectively. Each sub-cell independently absorbs photons within its respective energy range, which can generate electron–hole pairs. Subsequently, charge carriers are separated by the built-in electric field, producing a photovoltage. This enables the additive combination of their respective open-circuit voltages, while the overall current is constrained by the poorer-performing sub-cell.[14] Due to the reduction of thermal loss and transmission losses, PCE can be increased to >40%, so people are paying more and more attention to tandem cells (Fig. 1d and e).[15]

The electrical coupling configuration between the front and rear subcells serves as a key criterion for classifying TSCs. Based on this principle, TSCs are generally categorized into two primary types: monolithic (2-terminal, 2T) TSCs and mechanically stacked (4-terminal, 4T) TSCs. 4T TSCs consist of independently fabricated subcells that are mechanically stacked, eliminating the need for current matching or ICL/tunnel junctions (TJ) structures. The architecture provides greater processing flexibility, allowing separate optimization of each subcell.[16–18] By contrast, monolithic 2T TSCs, featuring a vertically integrated structure with sequentially deposited layers, present a more cost-efficient and lightweight solution. By eliminating redundant conductive layers, it minimizes parasitic absorption losses associated with lateral current collection in transparent interlayers, as charge transport is confined to vertical conduction through the ICL. High-performance monolithic 2T TSCs fundamentally require efficient electrical coupling between the constituent subcells.[19–21] The ICL must simultaneously ensure efficient optical transmission, electrical conductivity, and mechanical stability between subcells. Under illumination, the front cell absorbs high-energy (short-wavelength) photons, while the rear subcell captures the transmitted low-energy (long-wavelength) photons, enabling complementary spectral utilization.[22] Additionally, since the quasi-Fermi levels of electrons and holes in the two subcells differ, the ICL must facilitate efficient recombination at the interface to ensure proper electrical interconnection. The optimal ICL must provide sufficient recombination sites and form an ohmic contact with the charge-extracting layers of each subcell to facilitate rapid electron–hole recombination, mitigating open-circuit voltage loss (V_{OC} loss) caused by charge accumulation. The ICL should exhibit low series resistance to minimize energy dissipation during charge transport.

Wide-bandgap (WBG) perovskite has been demonstrated to be a suitable material for constructing PeTSCs. With the rapid development of WBG PSCs, perovskite/Si, perovskite/Cu(In,Ga)Se_2 (CIGS), and all-perovskite TSCs have obtained the highest certified efficiency of 34.9%, 26.3%, and 30.1%, respectively.[23] Notably, the low-temperature solution treatment (<100 °C) of all-perovskite TSCs has an absolute advantage in terms of manufacturing flexibility, and significantly reduced production costs. These merits position all-perovskite TSCs as the most viable solution for future large-scale commercialization of high-efficiency, low-cost tandem photovoltaics.[11,24] Nevertheless, the WBG perovskite typically has a high Br-content (typically $\geq$30%), which induces phase segregation under continuous illumination to form I-rich and Br-rich phases.[25] The halogen phase segregation and interfacial defects will accelerate carrier recombination and increase voltage losses.[26] Moreover, the oxidation of Sn^{2+} to Sn^{4+} leads to high defect state density and material degradation. It will further affect the photoelectronic properties and stability of all-perovskite TSCs.[27] In addition to all-perovskite TSCs, emerging OSCs have become an attractive option for narrow-bandgap (NBG) rear cells due to their good near-infrared absorption and flexible solution processability. Recently, Li *et al.* utilized the ternary component of PM6:BTPSe-Ph4F: MO-ITIC-2F as rear cells to boost the certified PCE up to 25.7% for perovskite/organic tandem solar cells (PO-TSCs).[28] The development of perovskite or organic materials, combined

Yiwang Chen

Yiwang Chen is a full professor of chemistry at Nanchang University and Jiangxi Normal University. He received his PhD degree from Peking University in 1999. And he was a postdoctoral fellow at Johannes Gutenberg-Universität Mainz and Philipps-Universität Marburg in Germany. He was honored by the National Science Fund for Distinguished Young Scholars in 2014. He has been serving as the president of Gannan Normal University since 2022. His research interests include polymer/perovskite solar cells, hybrid supercapacitors, sodium ion batteries, intelligent elastomers, zinc–air batteries, and electrocatalysis.

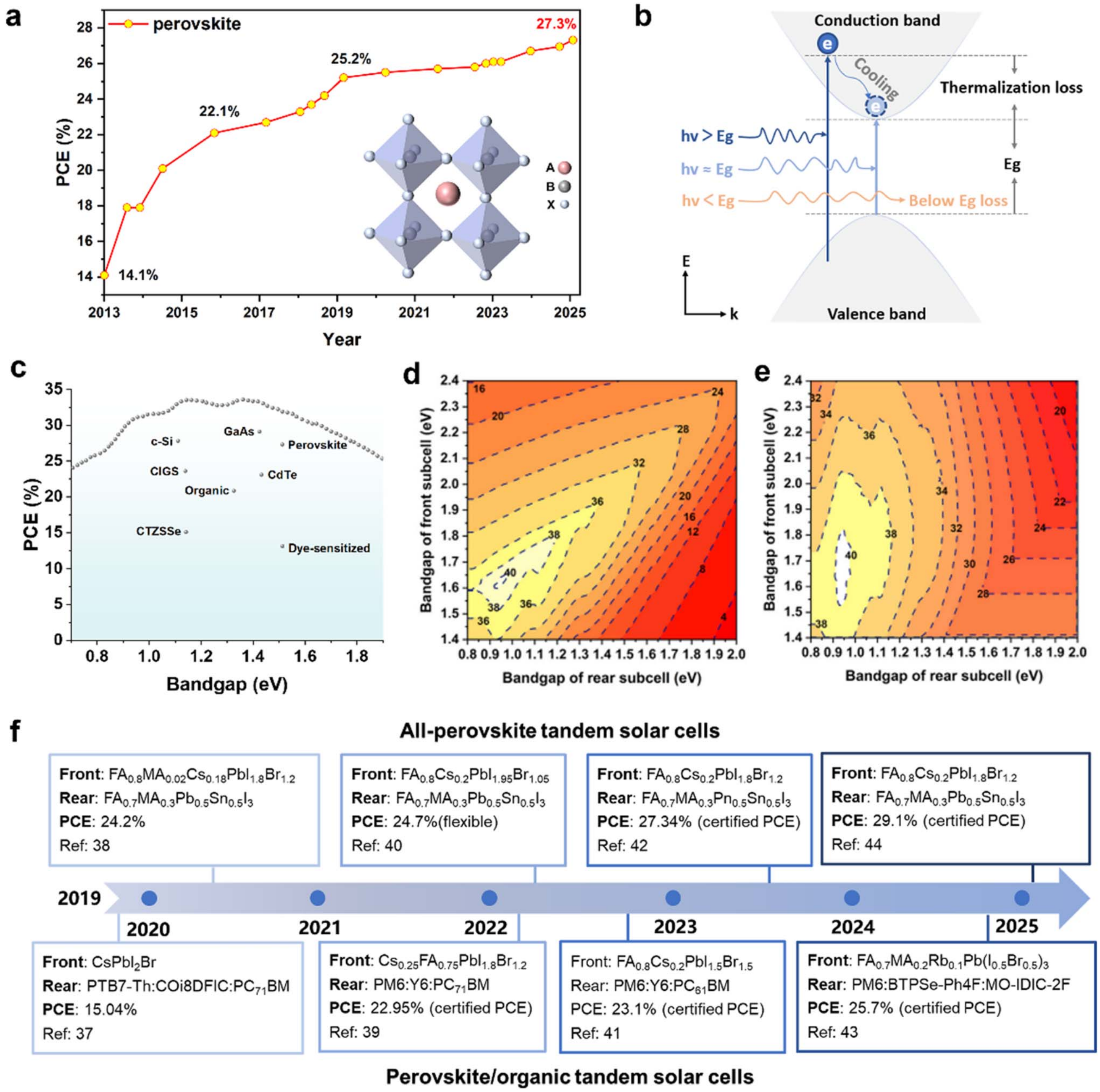

Fig. 1 (a) Three-dimensional crystal structure of perovskite, and PCE of PSCs released by the National Renewable Energy Laboratory. (b) Band diagram of the thermalization loss (*i.e.*, hot carriers generated by light-excitation [$h\nu$] higher than the bandgap [E_g], followed by cooling/relaxation) and below-band-gap loss (*i.e.*, $h\nu < E_g$, transmittance loss).[11] Copyright 2023, Elsevier. (c) The theoretical maximum efficiency of single-junction solar cells is calculated according to the S–Q limit, and single-junction solar cells based on Si and GaAs currently hold the record for the highest efficiency. PCE of single-junction solar cells released by the National Renewable Energy Laboratory. (d and e) Practical efficiency limits of two-junction solar cells with 2-terminal (d) and 4-terminal (e) configurations.[36] Copyright 2020, Elsevier. (f) Timeline and the PCE evolution of Pe-TSCs with different compositions of perovskite and organic active materials.[28–35]

with technical advances at ICL, rapidly increased the PCE of solution-processed PeTSCs in just a few years (Fig. 1f).[28–35]

In this review, we systematically summarize the key issues from material design to subcell integration of PeTSCs, and reveal the physical mechanism and materials science principle of efficiency improvement. To identify the important levers for further progress, we focus on the optimizations of wide-bandgap perovskite front subcells and narrow-bandgap perovskite or organic rear subcells before discussing the consequence of interconnecting layers for tandem devices. Finally, we identify the challenges associated with flexible configuration and large-area manufacturing tandem concepts, and offer insights into the emerging research directions and commercialization of solution-processed PeTSCs.

2. Bandgap tuning and interface engineering for WBG perovskite front cells

2.1 Bandgap tuning of WBG perovskite

2.1.1 Composition (ABX_3). As the front cell of PO-TSCs, the crystal structure of WBG PSCs is ABX_3. WBG PSCs can adjust their bandgap to match the back cell by adjusting different chemical compositions. The conduction band is mainly dominated by B-p orbitals, and the valence band is composed of B-s and X-p orbitals. While the A-site cation does not have much effect on the band, it can affect the bandgap by affecting the lattice size.[37,38] A, B and X sites have a significant impact on the bandgap of the perovskite material, which also leads to the fact that WBG PSCs usually have complex components. Their different ionic properties will compete with each other to enhance and complicate the crystallization process of the film, forming different morphologies/geometries. Thus, it is challenging to understand the mechanism of WBG PSC film formation and control the morphology and characteristics of the film. Although the wider the bandgap of perovskite, the greater its limiting V_{OC}, the crystalline nucleation of the perovskite is determined based on supersaturation. And crystal growth is mainly driven by ion diffusion into the formed nucleus. In general, by altering the I:Br ratio, it is possible to adjust the E_g between 1.48 eV and 2.3 eV (Fig. 2a).[39] The structural integrity of perovskite crystals necessitates precise optimization of halide stoichiometry (X = I/Br) to achieve a Goldschmidt tolerance factor (t) approaching the ideal range of $0.9 < t < 1.0$, thereby stabilizing the cubic phase through balanced ionic radii matching between A-site cations and $[BX_6]^{4-}$ octahedra (Fig. 2b).[40,41] However, considering the low solubility of bromide and the small ionic radius of Br^- ($r = 1.96$ A) compared to I^- ($r = 2.20$ A), a high concentration of Br content can accelerate one of the crystallization processes of perovskites. As a result, there are intrinsic defects in WBG perovskite.[42,43] The high defect state density and photoinduced phase segregation of WBG perovskite cause large V_{OC} loss of WBG PSCs. Therefore, several optimization strategies have been developed, which can be summarized as additive engineering, interface engineering, and mixed cation engineering, to solve the above problems and further reduce V_{OC} loss and increase PCE.

2.1.2 Additives. Additive engineering is one of the effective methods to passivate defects. To achieve high efficiency and stability, it is essential to apply additive engineering to PSCs. Additive engineering improves the efficiency and stability of perovskites by controlling nucleation and crystal growth, while for WBG perovskite, a high concentration of Cs or Br will significantly accelerate the crystallization process, resulting in poor crystallicity, a rough surface, and greater defect state density of perovskites, which greatly limits its V_{OC} improvement and photostability (Fig. 2c).[26,44,45] Adding additives into

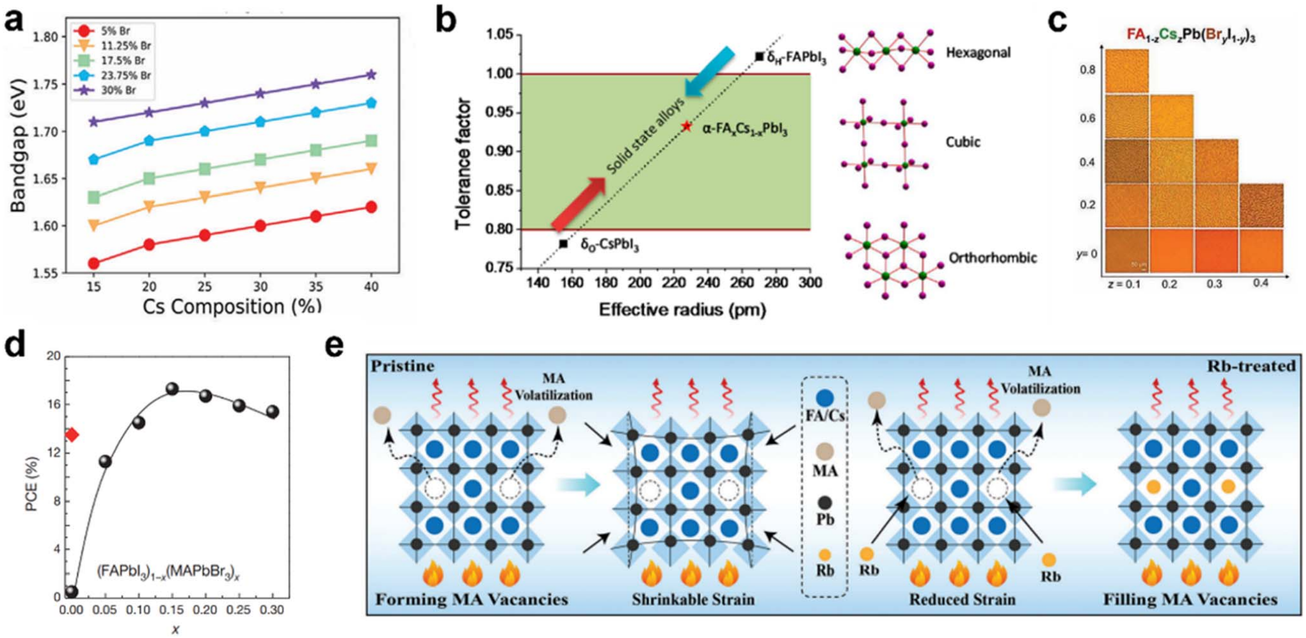

Fig. 2 (a) E_g *versus* perovskite composition for $Cs_xFA_{1-x}Pb(Br_yI_{1-y})_3$.[39] Copyright 2016, The American Association for the Advancement of Science. (b) Correlations between the tolerance factor and crystal structure of perovskite materials.[40] Copyright 2016, American Chemical Society. (c) Optical images showing perovskite film morphologies at varying Cs/Br contents.[55] Copyright 2021, Springer Nature. (d) PCE values for cells using $(FAPbI_3)_{1-x}(MAPbBr_3)_x$ materials, which were annealed at 100 °C for 10 min (black line); the red diamond indicates the PCE value for the cell fabricated using pure $FAPbI_3$ ($x = 0$); annealing was performed at 150 °C for 10 min to form the black perovskite phase.[48] Copyright 2024, John Wiley and Sons. (e) Schematic diagram of filling vacancy defects and relieving lattice strain during annealing of the WBG perovskite film.[53] Copyright 2025, American Chemical Society.

perovskite precursor solutions facilitates controlled crystallization kinetics, enlarged grain size, and reduced grain boundary density in perovskite thin films. Simultaneously, surface and grain boundary defects can be effectively passivated. For optimal application of additive engineering in perovskites, interactions between the additive and the perovskite precursor solution must be considered. First, the organic cations in halide perovskites are mainly composed of ammonium functional groups. The ammonium functional group interacts with the $[BX_6]^{4-}$ octahedron through hydrogen bonds, in which the change in the A-site cation mainly affects the phase or crystal structure, and does not significantly change the band structure and band edge charge carriers.[40,46] Employing mixtures of multiple cations has emerged as an effective strategy for enhancing the performance and stability of perovskite layers. For instance, $FAPbI_3$, commonly used in perovskite solar cells (PSCs), undergoes a phase transition from the δ-phase (non-perovskite) to the α-phase (perovskite) at 150 °C. However, due to lattice contraction, the α-phase can be stabilized at lower temperatures when a smaller cation, such as MA, is introduced into the FA position. Seok *et al.* demonstrated that the mixed FA^+/MA^+ cation system in $(FAPbI_3)_{1-x}(MAPbBr_3)_x$ improves perovskite film morphology and optimizes fabrication protocols in PSCs. Finally, the efficiency and stability of PSCs are improved (Fig. 2d).[47] The small radius of the A-site cation can shrink the perovskite crystal structure and the $[PbX_6]^{4-}$ octahedron, strengthening the A-site cation–halogen bond. The use of smaller cations at the A site increases the bandgap of the lead halide perovskite and can be improved. In addition, it is found that rubidium is suitable for crystal structure formation without additional defects. It can increase the ion migration barrier and further inhibit ion migration through lattice distortion. Yang *et al.* found a lattice strain adjustment strategy for high-performance WBG PSCs. Rubidium (Rb) cations were introduced to fill the A-site vacancies caused by methylammonium volatilization, which alleviated the shrinkage strain of the perovskite crystal. The reduced lattice distortion and increased halide ion migration barrier lead to homogeneous mixed halide perovskite films (Fig. 2e).[48] However, excessive addition of Cs^+ is damaging to the perovskite structure and causes the film to decompose quickly in air. In addition, excess Cs^+ will cause the phase transition temperature of perovskite to become higher. Yuan *et al.* investigated the degree of influence of A-site cations on the overlap of metal halide orbitals. Such changes in metal–halide bonding have direct effects on valence and conduction band positions, bandgaps, and the stability of the perovskite lattice.[49] In addition to cations smaller than FA, larger cations including guanidinium (GA), imidazolium (IA), and dimethylammonium (DMA) are also used as additives. Among them, the ionic radius of the commonly used large cation GA is about 278 pm, which is slightly larger than the tolerance factor.[50] However, incorporating GA^+ into perovskites increases hydrogen bonding within the inorganic framework, forming a highly stable three-dimensional (3D) crystal structure. This enhanced stability improves carrier lifetime and inhibits ion migration.

In addition to cationic doping, some researchers improve the performance of perovskite by adding anionic additives. Thiocyanate (SCN^-) can control the defect tolerance and charge carrier trapping, and reduce the GB of perovskite thin crystals, which will not have a great impact on the band gap of perovskites.[51,52] Zhou *et al.* proposed a combined application of lead thiocyanate ($Pb(SCN)_2$) and olamine hydrochloride (OAmCl) for the perovskite precursor solution. While SCN^- is capable of crystallizing, it is easy to form PbI_2 defects, and OAmCl has the potential to hinder the production of PbI_2. The formation of interface dipoles through surface assembly promotes the N-type characteristics on perovskite surfaces, thereby facilitating enhanced carrier extraction efficiency. The device efficiency is 21.55% and the fill factor (FF) is 86.03% (the bandgap is 1.65 eV).[53] In addition to SCN^- ions, which effectively increase grain size, MACl additives are also commonly employed to enhance the crystallinity and uniformity of perovskite films. Snaith *et al.* proposed that MACl used in perovskite will lead to the formation of Cl^- rich intermediate phases, promote the crystalline growth of perovskite, and reduce the bulk defects and photoelectric properties of perovskites.[54]

2.1.3 Phase segregation. Phase segregation in the WBG PSC is the most pressing bottleneck for the stability of PeTSCs. The bandgap of mixed halide perovskites is mainly adjusted by changing the composition of the halide, for example, it can be used to achieve a bandgap of 1.79 eV with a I : Br (3 : 2) mixed halide.[29] However, with the increase in the relative content of Br in perovskites, the perovskite phase tends to separate into I-rich and Br-rich domains under illumination (Fig. 3a), forming a Br-rich perovskite with a higher bandgap and I-rich perovskite with a lower bandgap.[33] The energy difference serves as the thermodynamic driving force for halide segregation.[45] And the significant valence band offset between I-rich and mixed phases readily locates and traps holes. Charges pooling from the mixed WBG phase into I-rich regions dissipate energy, reducing the achievable V_{OC} in high-Br-content PSCs. Charges in the well-mixed WBG phase pool into the I-rich region, losing energy in the process and thereby reducing the achievable V_{OC} of the high Br content PSCs. This funnel effect leads to a high charge carrier density in the I-rich phase, which in turn leads to very prevalent low-energy photoluminescence. In addition, due to the low saturation of bromide, the Br-rich region will accelerate the crystallization of perovskite, and the bromide-rich region in the perovskite structure will lead to an increase in trap density and the existence of a large number of deep-level defects, which results in severe non-radiative composite loss.[38,56] Interestingly, once back in the dark, the entropy-driven mixing of halides brings the system back to homogeneous conditions, and despite a reversible material transition, the carrier lifetime is too short relative to the ionic dynamics to allow the system to return to its initial state. Photoinduced phase segregation was first discovered in 2015 by Hoke *et al.*, who observed that mixed halide perovskites would redshift under light (Fig. 3b).[25,57] A large number of experimental results show that the composition and electronic structure of WBG perovskite will change under light. Macrometrically, segregation of mixed halide

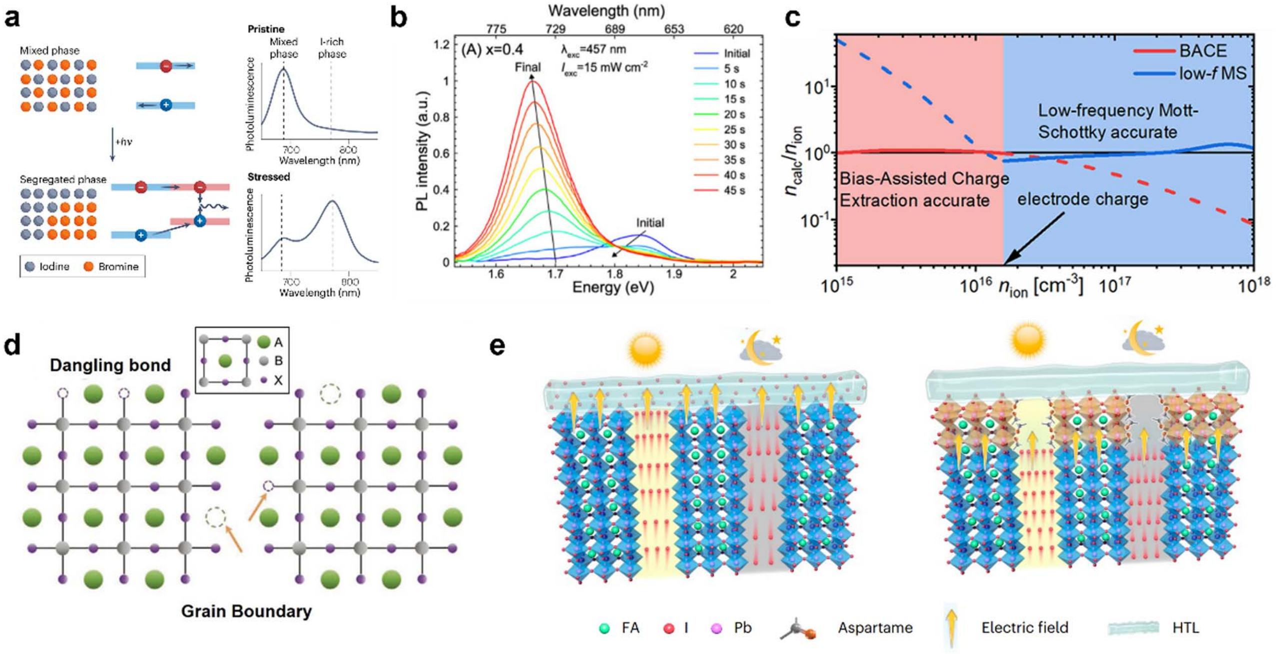

Fig. 3 (a) Schematic illustration of illumination-triggered halide segregation (left), corresponding energy-level diagrams (middle), and measured photoluminescence spectra (right) for both the pristine phase and light-exposed segregated phase. Following light-induced segregation, the photoluminescence spectrum develops a second peak at a wider wavelength, corresponding to an I-rich phase, and the peak at shorter wavelengths, the mixed phase emission, becomes smaller in comparison.[33] Copyright 2022, Springer Nature. (b) $MAPb(I_{0.6}Br_{0.4})_3$ photoluminescence (PL) spectra in 5 second segments over 45 seconds of continuous wave (CW) illumination ($\lambda_{exc} = 457$ nm, $I_{exc} = 15$ mW cm^{-2}) at 300 K.[57] Copyright 2020, Elsevier. (c) Bias-assisted charge extraction (BACE) and modified Mott–Schottky (MS) analysis at low frequencies provide ion density values for perovskite photovoltaic devices.[59] Copyright 2023, American Chemical Society. (d) Schematic illustration of a crystal lattice with vacancies (dangling bond) at surfaces and grain boundaries.[66] Copyright 2022, John Wiley and Sons. (e) Schematic diagram for inhibition of iodide ion migration in the control (I) and target (II) devices.[63] Copyright 2024, Springer Nature.

perovskites is favorable for a lower Gibbs free energy, which is represented by

$$\Delta G_{\text{mix}} = \Delta H_{\text{mix}} - T\Delta S_{\text{mix}}$$

where H, T, and S correspond to the enthalpy, temperature, and entropy, respectively. When the free energy is negative, the mixed halide perovskite will be more stable. In general, external stimuli can be used, such as adding bias or light, to increase ΔH_{mix} and change the free energy, so that phase segregation of WBG perovskite occurs. At the microscopic level, all phase segregation is related to ion migration, which is closely related to morphology. Studies have shown that halogen anions have the lowest ion migration energy in perovskites, this means that the halogen anion is more likely to be offset than the A-site cation and B-site cation, which leads to phase segregation in WBG PSCs.[56–58] Mobile ions can lower device performance and stability by impeding charge extraction and screening the internal electric field. Due to the complex ion composition of the WBG perovskite, the internal ion migration problem is difficult to solve. Stolterfoht *et al.* conducted a low-frequency MS analysis to demonstrate that light induction produces phase segregation and can eliminate ion density. It is dependent on the internal field distribution in the layer stack, able to accurately determine the movement of CV charges (Fig. 3c).[59] Experimental studies have indicated that the iodine vacancies (V_I^+) and interstitial iodine defects (I_i^-) exhibit extremely low migration activation energy. Furthermore, Barboni revealed that V_I^+ formation occurs *via* the neutralization of I_i^- by photogenerated holes, with such defects preferentially accumulating at perovskite grain boundaries (GBs). Under prolonged thermal stress, it will lead to the degradation of perovskite and halide vacancies, forming more GBs. The higher concentration of positive space charge near the GBs may serve as the initial driving force for phase segregation (Fig. 3d).[60] This leads to phase segregation and facilitates the high mobility of iodine under thermal stress. Subsequent iodine diffusion along the perovskite surface and into the hole transport layer (HTL) significantly degrades device performance and stability. To mitigate these effects, increasing grain size and passivating boundary defects can increase the activation energy (E_a) for ion migration while suppressing phase segregation. For instance, introducing cationic dopants such as Cs^+ or Rb^+ promotes perovskite crystal growth, thereby enlarging grain size and improving stability. Defects can also be blunted by thiocyanate ions (SCN^-) to reduce halide migration pathways. Li *et al.* found that incorporating a small amount of SCN^- into perovskite films enabled its entry into the lattice, forming an I/Br/SCN alloy phase and occupying iodine vacancies, thereby modifying the crystal structure and optical properties. In particular, the addition of SCN^- to the perovskite lattice significantly increases the spatial steric hindrance, thereby greatly increasing the energy barrier for I^- migration and effectively inhibiting ionic migration.[61] The results demonstrate that steric hindrance effects can be efficiently mitigated through ion migration.[62] Moreover, prolonged illumination induces phase segregation, as photogenerated electrons and holes drive halogen ion migration under an electric field. Due to the differences in mobility and chemical potential of different halogen ions, they will redistribute in the material under the action of photogenerated charge carriers, thus causing phase segregation. Additionally, photoexcitation may cause the interaction between the halogen vacancy and the halogen gap to form a Frenkel pair defect, and the iodine on the bromine gap will migrate faster to the free iodine site to induce phase segregation. Based on this, research on realizing WBG PSCs with balanced charge transport is expected to suppress phase segregation. The internal electric field of perovskite can be controlled by controlling the doping. Han *et al.* induced an electric field inside the perovskite by precisely controlling the doping depth, which counteracted ion migration while enhancing carrier separation, thus suppressing phase segregation (Fig. 3e).[63] Due to the presence of tensile strain caused by lattice mismatch between the I^- and Br^- perovskite lattices, WBG perovskite may exhibit lower ion mobility E_a than their normal counterparts.[42,64] Moreover, a higher Br^- ratio introduces excess halide vacancies, creating ion migration channels and recombination centers. Reducing the Br content modifies the lattice volume and alleviates strain. Notably, the unit cell volume decreases significantly from I to Br to Cl, suggesting that partial substitution of Br^- with Cl^- can effectively control strain, thereby enhancing the activation energy (E_a) for ion mobility. Hence, phase segregation is the primary problem in manufacturing efficient and stable WBG PSCs.[65]

2.2 Interface engineering

2.2.1 Surface passivation. Extensive research has focused on improving radiative recombination and reducing non-radiative recombination in perovskite.[54,56,67] A variety of methods exist for localized charge carriers *via* quantum confinement[68] and ion doping,[69] or enhancing photon state density using metamaterials to boost the rate of radiation recombination.[70] In addition, the trap-assisted non-radiative recombination rate can be reduced by the recrystallization of perovskites[71] or the chemical passivation of defects.[72]

It is theoretically shown that the dominant intrinsic defects formed in the perovskite layer are shallow-level defects.[73] However, it has been demonstrated that mitigating defects in perovskite films is crucial for enhancing the performance and stability of PSCs. Notably, high-density surface defects at polycrystalline grain boundaries drive degradation of the perovskite structure. These surface defects likely originate from the evaporation of volatile organic components during thermal annealing, and therefore surface passivation is essential.[74,75] The majority of the passivated molecules on the surface are spin-coated on the perovskite film, and the resulting film exhibits changes in its surface chemical and physical properties, which affect the interface-induced recombination loss. Surface defects can be mitigated through the interaction among relevant molecular species. You *et al.* developed phenethylammonium iodide (PEAI), an organic halide salt, as a surface passivation additive for 3D perovskite structures during the post-processing of hybrid perovskite materials (Fig. 4a).[76] This approach demonstrated significant effectiveness in mitigating surface defects within perovskite films. Due to the strong intermolecular forces such as hydrogen bonds between small molecules and π–π stacking, most interface passivation will induce self-aggregation. This aggregation can be alleviated by introducing additional steric groups. Chen *et al.* weakened the self-aggregation initiated by intermolecular hydrogen bonds through the ester group, and the aggregation could be dispersed by heating to form a mesh insulating layer with random openings, thus greatly increasing the charge transport capacity (Fig. 4b).[77] In addition, the chalcogenide-based functional ligands exhibit strong binding to deep-level Pb^{2+} defects and halogen vacancies, demonstrating superior interfacial passivation capability. Huang *et al.* explained that the flat molecular structure of chalcogenide-based functional ligands would hinder their ability to fully encapsulate or trap defects on the perovskite surface that could exacerbate non-radiative recombination.[78] Large organic conjugated molecules enable near-100% internal luminescence efficiency and provide stable surface passivation in perovskite films. Nevertheless, these molecules might restrict the movement of charge carriers. The impact of organic ligand conjugation on the performance of PSCs remains challenging.[79]

In addition, the construction of interface 2D/3D heterostructures *via* long-chain alkylamines is widely used to blunt defects, prevent ion migration, and inhibit phase segregation of PSCs (Fig. 4c).[80,81] When the quasi-2D ($n \geq 2$) perovskite layer is directly constructed on the Cs and FA WBG perovskite thin film, the WBG PSCs achieve a power conversion efficiency of 19.6% and open circuit voltage of 1.32 V, and the all-perovskite TSC shows a stable PCE of 28.1%.[82] These 2D/3D structures were formed by spin-coating ligand solution onto the surface of perovskite. The V_{OC} loss of the WBG PSCs was limited by using the halide amine in surface posttreatment. In addition, Zhao *et al.* tuned 2D perovskite phase purity on 3D WBG perovskite using phenethylammonium bromide (PEABr) post-treatment at controlled annealing temperatures. This approach can passivate surface defects and optimize the surface electric field. The results show that the 1.77 eV WBG PSC achieves a PCE of 17.72% and a high V_{OC} of 1.284 V, and a four-terminal (4-T) all-perovskite TSC is constructed to obtain a PCE of 25.17%.[83] These 2D passivation layers passivate perovskite surface defects, thereby enhancing device PCE. However, the diffusion of organic ligands in the passivating layer will damage the 3D perovskite structure of the perovskite at high temperatures, which will affect the stability and efficiency of PSCs.[84] Besides, a more stable interface structure of corresponding PSCs can be constructed by introducing aniline and its fluorinated derivatives.[85] On the one hand, the influence of organic amines on the internal structure of perovskite is still controversial. On the

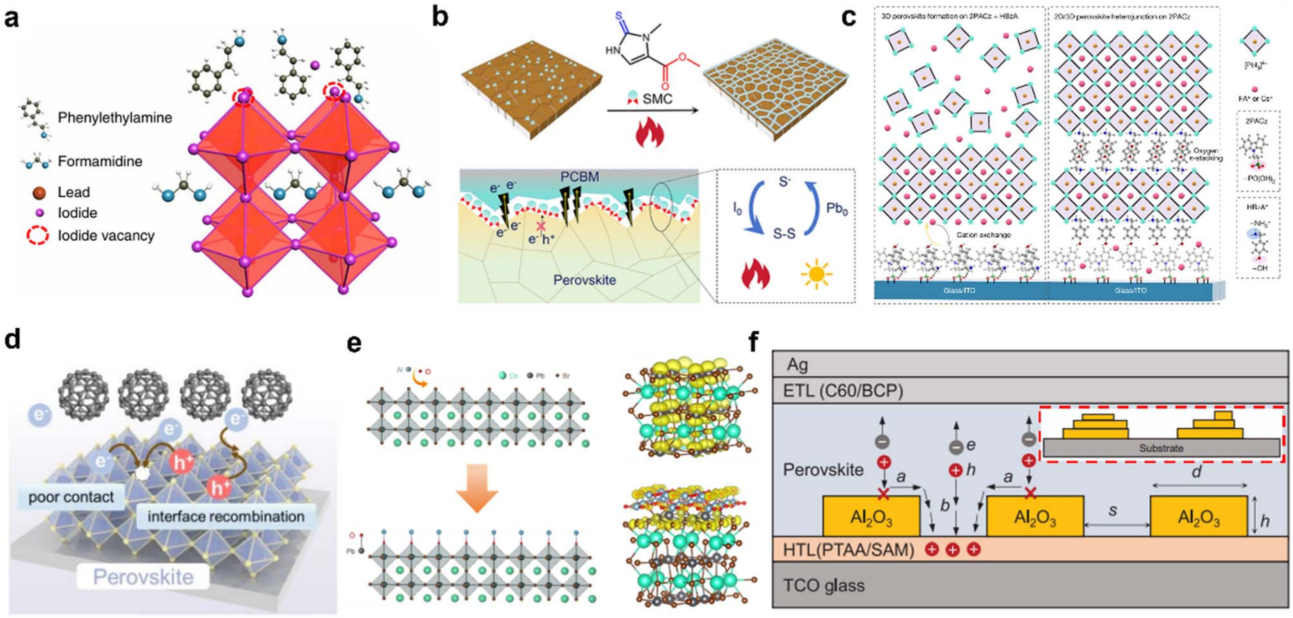

Fig. 4 (a) Underlying passivation mechanism of the PEAI layer for the perovskite film.[76] Copyright 2019, Springer Nature. (b) Schematic diagram of the SMC molecular post-treatment process and distribution.[77] Copyright 2024, American Chemical Society. (c) The mechanism of 3D perovskite formation on indium tin oxide (ITO)/(2PACz + HBzA) and cation exchange at the bottom interface (left); a 2D/3D heterojunction on the ITO/2PACz bottom contact (right).[80] Copyright 2024, Springer Nature. (d) Schematic of the perovskite/C_{60} surface layer without passivation. (e) Schematic diagram showing the chemical modification of the $CsPbBr_3$ perovskite with Al_2O_3 (left); real-space distributions of the densities of electronic states at conduction band minima of the bare and Al_2O_3-modified $CsPbBr_3$ perovskites (right).[91] Copyright 2022, John Wiley and Sons. (f) Schematic description of the PIC device structure.[92] Copyright 2023, The American Association for the Advancement of Science.

other hand, organic amines react with excess PbI_2 on the surface of perovskites and form low-dimensional perovskites. The relevant mechanism needs to be further discussed.

Beyond defect passivation, interfacial recombination critically influences device performance, particularly in TSCs. C_{60}, $PC_{61}BM$, and ZnO are commonly employed as electron transport layers (ETLs) in inverted PSCs. Notably, the perovskite/C_{60} interface suffers from poor contact[86] and inefficient energy level alignment,[87] with these limitations becoming increasingly pronounced upon device expansion (Fig. 4d). To address this challenge, researchers have introduced interfacial layers between perovskite and C_{60}. Chen *et al.* demonstrated that 2-aminoethyl hydrochloride (AET-HCl) forms low-dimensional phases, simultaneously suppressing non-radiative recombination and optimizing interfacial energy level alignment. This approach yielded WBG ($\sim$1.67 eV) PSCs with a high V_{OC} of 1.25 V and a stabilized PCE of 20.62%.[88] Similarly, lithium fluoride (LiF) interlayers significantly enhance the performance of PSCs, though the passivation mechanisms remain incompletely understood. Korte *et al.* demonstrated that LiF introduces interfacial dipoles and fixed positive charges, reducing hole concentrations and improving energy level alignment between C_{60} and perovskite.[89] Conversely, Lee *et al.* revealed that aging induces Li^+ migration into the perovskite bulk while F^- remains at the interface. The mobile Li^+ occupies interstitial sites, causing lattice expansion that improves the FF and induces n-type doping near the surface. This creates an extended depletion region and built-in electric field that facilitates efficient electron extraction.[63,90] Radiative recombination efficiency serves as a critical determinant of perovskite luminescence properties, though quantifying the intrinsic radiative recombination rate remains challenging. Moving beyond conventional passivation strategies, Schmidt *et al.* developed an interfacial engineering approach through chemical modification to construct perovskite-oxide heterostructures. The analysis of excited-state dynamics and electronic band structures demonstrated that Al_2O_3 modification significantly enhances exciton binding energy and increases local electron state densities at perovskite surfaces, which can boost radiative recombination efficiency (Fig. 4e).[91]

Al_2O_3 serves as a versatile dielectric material in PSCs, which can function both as an upper-interface passivation layer and an ultrathin insulating buffer at the bottom interface. Recently, Xu *et al.* proposed a porous insulator contact (PIC) strategy, inspired by local contacts in Si photovoltaics, wherein a $\sim$100 nm Al_2O_3 interlayer was introduced between the perovskite and HTL. This architecture featured stochastic nanoscale apertures formed *via* solution-processed Al_2O_3 nanoplate assembly, reduced the perovskite/HTL contact area by $\sim$25%, and suppressed surface recombination velocity from 64.2 cm s^{-1} to 9.2 cm s^{-1}. The PIC simultaneously enhanced perovskite crystallinity and minimized non-radiative losses, enabling a champion PCE of 25.5% (Fig. 4f).[92]

2.2.2 Bottom interface.

While top interface modification effectively passivates surface defects and suppresses ion migration, the bottom interface remains a critical challenge due to its propensity for defect-induced non-radiative recombination, which significantly deteriorates device performance and stability. The modification of the bottom interface is complicated by two key factors: (1) the dissolution of pre-deposited interfacial molecules by polar solvents (*e.g.* DMF and DMSO) in perovskite precursor solutions, and (2) the difficulty of *in situ* defect characterization compared to that of the top interface.[93–96] Additionally, the rapid crystallization of perovskite films generates a high density of defects, predominantly localized at grain boundaries and interfaces, further exacerbating charge recombination losses.[97,98] The rapid crystallization exacerbates defect formation at the bottom interface, due to its role as the termination site of perovskite nucleation and film growth.[99] Consequently, the interface is frequently plagued by incomplete coverage, non-uniform nucleation, and poor interfacial contact. This invariably results in a higher defect density and inferior electronic properties compared to the surface region or the bulk material.[100,101] These defects are predominantly deep-level defects, which induce severe non-radiative recombination of charge carriers, significantly degrading the photovoltaic performance of the device. Furthermore, residual strains (typically categorized as compressive or tensile) are commonly present in perovskite films. The strains originate from multiple factors, including the coefficient of thermal expansion (CTE) mismatch between perovskite and charge transport materials, lattice mismatch with substrates, temperature gradients, light/bias stimulation, phase transitions, and grain boundaries (Fig. 5a).[102,103] Strain in perovskite films significantly influences the band structure, carrier mobility, bandgap, ion migration, and defect formation energy. Studies indicate that tensile strain increases the bandgap, whereas compressive strain reduces it.[104] Adjusting cation stacking patterns can enhance carrier mobility and mitigate microstrain.[105,106] Additionally, compressive strain increases the activation energy for ion migration, while tensile strain lowers it, potentially exacerbating non-radiative recombination and degrading the stability of PSCs.[107] To address these issues, interfacial molecular engineering is crucial for trap passivation and strain release. Chen *et al.* employed adamantane derivatives (2-adamantanone (AD) and 1-adamantane carboxylic acid (ADCA)), and 1-adamantaneacetic acid (ADAA) to modify the SnO_2/perovskite interface. These molecules effectively passivated defects, relieved interfacial strain, and improved device performance. The steric hindrance of the C═O interaction with perovskite and SnO_2—determined by the distance between the carbonyl group and the adamantane ring—decreased sequentially from AD to ADCA to ADAA. This steric-hindrance-dependent strategy revealed that stronger interfacial chemical interactions correlate with enhanced defect passivation, strain relaxation, and device performance.[108]

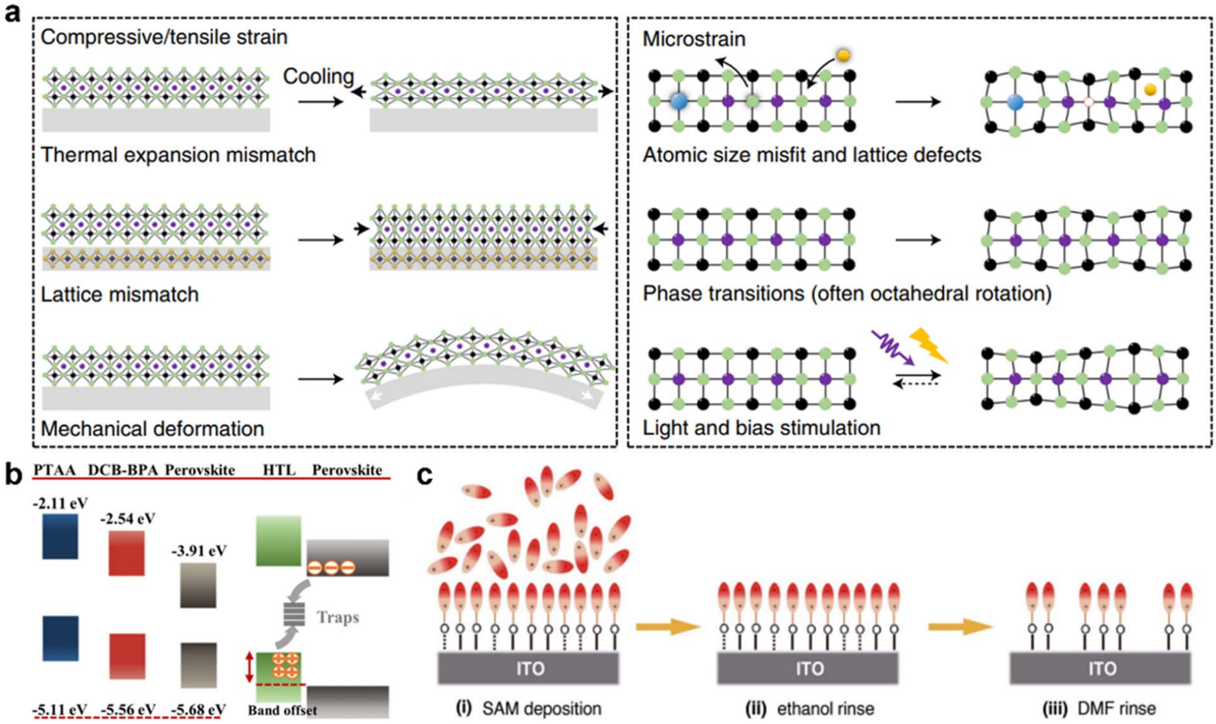

Fig. 5 (a) Origins of strain in halide perovskites. Representations of compressive/tensile strain (left) and microstrain (right) mechanisms are illustrated. Blue and purple spheres denote A-site cations (*e.g.*, Cs^+, MA^+, and FA^+); black and green spheres represent metal cations (*e.g.*, Pb^{2+} and Sn^{2+}) and halide anions (*e.g.*, Cl^-, Br^-, and I^-), respectively. Orange spheres indicate substrate atoms. The red dashed circle is a vacancy, and the yellow sphere represents the extrinsic dopant that causes a defect.[102] Copyright 2021, Springer Nature. (b) Energy level diagram between different HTLs and the perovskite.[115] Copyright 2024, Royal Society of Chemistry. (c) Schematic of SAM adsorption and desorption on hydroxyl-functionalized ITO, with sequential solvent rinsing (ethanol followed by DMF). The dotted line represents a weak hydrogen bond.[116] Copyright 2024, The American Association for the Advancement of Science.

Conventional hole transport materials (HTMs) such as poly [bis(4-phenyl)(2,4,6-trimethylphenyl)amine] (PTAA), nickel oxide (NiO_x), and poly(3,4-ethylenedioxythiophene):polystyrene sulfonate (PEDOT:PSS) often suffer from significant V_{OC} loss, limiting the performance of WBG PSCs and their application in PeTSCs.[109–111] Consequently, self-assembled monolayers (SAMs) particularly [2-(9*H*-carbazol-9-yl)ethyl]phosphonic acid (2PACz) and its derivatives have emerged as promising alternative HTMs, which improve charge extraction and reduce V_{OC} loss, thereby enhancing the PCE of PSCs due to several advantages: (1) ultrathin nature reduces series resistance;[112,113] (2) ordered molecular alignment generates interfacial dipole moments that enhance hole extraction;[109,111,113] (3) they minimize interfacial recombination losses;[93,113] and (4) they simultaneously passivate bottom interface defects and promote high-quality perovskite crystal growth. These merits, combined with their facile synthesis, tunable energy levels, and compatibility with large-area fabrication, make SAMs particularly attractive for both single-junction and tandem PSCs, with growing applications in OSCs as well. Among them, Hayase *et al.* modified PTAA with 4,3BuPACz to form the PTAA/SAM bilayer, and the results demonstrated that this measure improved the film quality of WBG perovskite. This approach mitigates film distortion (reducing lattice disorder) and charge recombination site density. The modified PTAA layer further enhances charge carrier collection. The PCE of WBG PSCs reaches 16.57%.[114] In addition to the SAM modifying strategy, Zhao *et al.* designed a novel SAM (4-(5,9-dibromo-7*H*-dibenzo[*c*,*g*]carbazol-7-yl)butyl) phosphonic acid (DCB-BPA) to replace PTAA. Compared with PTAA, DCB-BPA reduces the non-radiative reorganization of the interface and the shift in the valence band between perovskite and the HTL. It further improves the quality of the bottom interface, which is beneficial to the subsequent growth of WBG perovskite. The single-junction WBG PSCs obtain a V_{OC} up to 1.339 V and certified PCE of 18.88%, and exhibit a low V_{OC} loss of 431 mV with respect to the bandgap (Fig. 5b).[115]

Although SAMs demonstrate good intrinsic light and thermal stability, the performance of PSCs has shown inconsistent long-term stability compared to conventional HTMs. This limitation primarily stems from the dependence of SAM assembly on surface hydroxyl groups of transparent conducting oxides (TCOs), where weak physical adsorption can lead to desorption in polar solvents like DMF. Therefore, Han *et al.* developed an ALD strategy to enhance SAM anchoring stability. They created robust binding sites for trimethoxysilane-based SAMs, enabling strong tridentate attachment to the substrate. This approach significantly improved device stability while maintaining efficient charge transport (Fig. 5c).[116]

2.2.3 Electrode interfaces. The electrode layer is a photogenerated carrier collection layer, which plays an important role in the photovoltaic performance of PSCs. The energy level matching at the interfaces affects the charge extraction efficiency of PSCs. Electrons transfer from the conduction band minimum (CBM) of perovskites to either the lowest unoccupied molecular orbital (LUMO, for organic materials) or CBM (for inorganic materials) of the ETL, prior to collection at the cathode.[117,118] Under optimal interface conditions where minimal energy barriers exist at both the ETL/perovskite and cathode/ETL interfaces, free electrons can be efficiently extracted from the perovskite layer into the ETL and subsequently collected at the cathode. Therefore, electrode materials in PSCs play an important role in determining device efficiency and stability. Among them, noble metals are widely employed as electrode materials due to their excellent electrical conductivity and superior chemical stability.[119,120] However, the utilization of noble metals is limited by their high costs and susceptibility to degradation, especially corrosion caused by iodine ions from the perovskite layer (Fig. 6a).[121] Upon reaching the counter electrode *via* the ETL, iodine ions oxidize to iodine, corroding the metal electrode and permeating the perovskite layer, which accelerates degradation.[122] Meanwhile, metal ions diffuse through the ETL into the perovskite layer, further accelerating the material degradation (Fig. 6b).[123] The electrode is corroded and forms inert compounds, such as silver iodide. The corrosion not only destroys the integrity of the electrodes but also reduces the long-term stability of the device. The corrosion can significantly hinder charge extraction through the charge transport layer (CTL) while simultaneously inducing dipole formation at the interface.[124,125] Contact between the ETL and a high-work-function metal induces charge transfer, resulting in upward energy band bending and a Schottky barrier that obstructs electron extraction. It has been shown that adding a buffer layer between the CTL and electrode can effectively solve such problems. The selection of materials mainly depends on the inherent water-repellence, density, and chemical stability of these boundary materials. For example, researchers developed a rational design by substituting the expensive 2,2′,7,7′-tetrakis(*N*,*N*-*p*-dimethoxyphenylamino)-9,9′-spirobifluorene (spiro-OMeTAD) with an inorganic copper(I) thiocyanate/reduced graphene oxide (CuSCN/rGO) composite. The rGO layer acts as an active buffer layer that effectively suppresses the interfacial ion migration at the top interface. PSCs with a fluorine-doped tin oxide (FTO)/TiO_2/$CsFAMAPbI_{3-x}Br_x$/CuSCN-rGO/Au structure were fabricated. The synergistic CuSCN/rGO hybrid system achieved comparable PCE to conventional spiro-OMeTAD-based devices, while offering superior cost-effectiveness and enhanced charge extraction, establishing a promising pathway for high-performance, low-cost perovskite photovoltaics.[126] rGO demonstrates significant advantages in interfacial charge extraction and device passivation; its surface chemistry presents a critical trade-off: the oxygenated moieties facilitate hole extraction through dipole-induced band alignment yet simultaneously induce charge localization *via* electrostatic interactions. This intrinsic conflict between hole selectivity and interfacial charge transport kinetics fundamentally limits the simultaneous optimization of extraction efficiency and charge transfer to the substrate. In addition, bathocuproine (BCP) serves as a widely utilized buffer layer in PSCs, primarily attributed to its deep valence band maximum (VBM) that energetically impedes hole transport, thereby effectively suppressing carrier recombination at the interface.[127,128] It acts as a barrier layer, preventing the diffusion of harmful species into the perovskite absorber and inhibiting the egress of degradation products.[129] However, due to the rapid crystallization of BCP, it tends to accumulate and form small regions on the PCBM surface, resulting in poor coverage and pinholes (Fig. 6c). Despite the paucity of BCP alternative

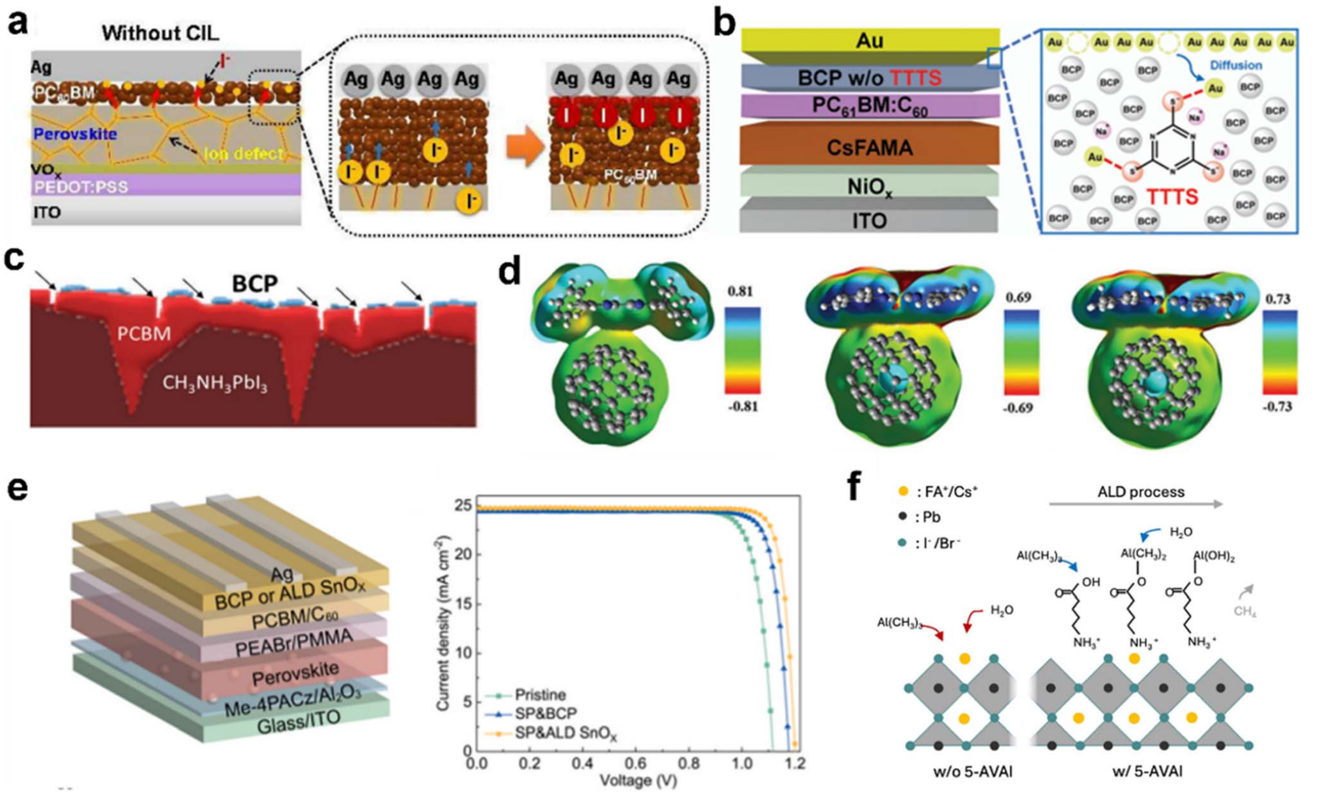

Fig. 6 (a) The reference structure of p–i–n PHJ PSCs and the cathode degradation process.[121] Copyright 2016, Royal Society of Chemistry. (b) Device structure and schematic of the BCP layer with TTTS.[123] Copyright 2022, Royal Society of Chemistry. (c) A schematic of the different passivation effects by BCP.[127] Copyright 2018, John Wiley and Sons. (d) Interactions between C_{60} and BCP, BCP-m1, and BCP-m2 are depicted in panels.[130] Copyright 2025, John Wiley and Sons. (e) Device structure of the inverted PSCs (left). Typical *J*–*V* curves of pristine, SP&BCP and SP&ALD-SnO_x devices (right).[134] Copyright 2024, Elsevier. (f) Schematic showing the perovskite surface with passivation ligands exposed to trimethyl aluminum (TMA) and water during Al_2O_3 deposition.[135] Copyright 2025, Elsevier.

development, the functional group modification strategy offers a viable pathway to enhance both structural ordering and electronic performance in PSCs. Seo *et al.* repositioned the existing distorted phenyl group on BCP to a more optimal location, protecting the pyridine's nitrogen and creating a more flat backbone configuration (Fig. 6d).[130]

Besides, some researchers use ALD technology to prepare uniform and dense films such as TiO_2, Al_2O_3, and SnO_x at low temperatures.[131–133] For instance, Qiu *et al.* demonstrated that the incorporation of compact SnO_x effectively suppresses volatile species escape from perovskite, mitigates moisture infiltration, and inhibits ion migration. Owing to its dense morphological structure and uniform surface coverage, SnO_x serves as an efficient permeation barrier in PSCs, significantly enhancing the operational stability of photovoltaic devices. Thus, devices with a structure of ITO/Me-4PACz/Al_2O_3/$Cs_{0.05}MA_{0.1}FA_{0.85}PbI_{2.9}Br_{0.1}$/PEABr/PMMA/PCBM/$C_{60}$/ALD-$SnO_x$/Ag showed excellent stability. The device achieves a champion PCE of 25.70% (certified 24.23%), along with a high V_{OC} of 1.202 V and FF of 86.41% (Fig. 6e).[134] However, research studies indicate that inadequate nucleation of metal oxides in ALD processes may stem from insufficient reactive sites available for ALD initiation, leading to instability in surface-modified ligands. Chen *et al.* attached the hydroxyl group in 5-ammonium pentanoate iodide (5-AVAI) to the perovskite surface, providing anchor sites for subsequent Al_2O_3 deposition. The stability of the modified devices is substantially improved. The encapsulated WBG PSCs can maintain 90% of their initial PCE over 1000 hours of thermal aging at 55 °C under 1-sun illumination (Fig. 6f).[135] It should be noted that the decomposition of perovskite materials can be triggered when the ALD deposition temperature surpasses 60 °C, as lower temperatures are critical for maintaining structural integrity during encapsulation processes. As discussed, the formation of a uniform and continuous electrode buffer layer exerts an indispensable influence on enhancing the stability of PSCs, providing an effective solution to one of the most critical stability challenges in perovskite photovoltaics.

3. Design of stable NBG perovskite or organic rear subcells

3.1 NBG perovskite subcells

3.1.1 Materials. Compared to other TSCs, all-perovskite TSCs offer the unique advantage of combining two perovskite subcells with tunable bandgaps (1.65–1.70 eV and 1.80–1.85 eV, ideal for top-cell integration) while utilizing cost-effective precursor materials. The high spectral tunability, coupled with significant PCE improvements in single-junction devices, makes them a promising candidate for high-performance tandem devices.[136,137] The perovskite rear cell with an NBG typically exhibits an energy gap of approximately 1.24 eV, representing the narrowest bandgap that has been achieved to date in high-efficiency metal halide perovskite photovoltaics.[138] These materials demonstrate an extended spectral absorption range, facilitating superior photon harvesting capabilities, thus improving the PCE. The most widely studied NBG perovskite materials are Sn-based or Sn–Pb mixed perovskites. While Sn-based perovskites exhibit advantages such as low toxicity and an ideal bandgap, the high chemical reactivity leads to rapid, poorly controlled crystallization, which affects the performance and stability of devices. Sn^{2+} oxidation persists even in oxygen-deficient environments.[139,140] In contrast, Sn–Pb hybrid perovskites demonstrate superior photovoltaic performance and stability, with single-junction PCE reaching up to 23% (Fig. 7a).[138] Sn–Pb perovskites are particularly suitable for all-perovskite TSCs, enabled by the bandgap bowing effect, which ensures optimal alignment with WBG PSCs. The above-mentioned effect arises from variations in energy levels and lattice strain–Sn incorporation induces compressive strain and octahedral distortion, modifying the bandgap. However, the underlying mechanism remains debated; for instance, $MASn_{0.75}Pb_{0.25}I_3$ exhibits an E_g of 1.17 eV, whereas $MASn_{0.25}Pb_{0.75}I_3$ shows 1.23 eV (Fig. 7b).[141] The stability of such perovskites can be preliminarily evaluated using the Goldschmidt tolerance factor (t), which is defined as follows:

$$t = \frac{r_A + r_X}{\sqrt{2} \times (r_B + r_X)}$$

where r_A, r_B, and r_X represent the ionic radii of the A-site cation, the B-site metal cation, and the X-site halogen anion, respectively. A value of $t \approx 1$ corresponds to an ideal cubic perovskite structure, with the stable range empirically established between 0.825 and 1.059. Due to the smaller ionic radius of Sn^{2+} compared to Pb^{2+}, Sn–Pb perovskites exhibit t values approaching unity, with stability further enhanced at higher Sn-doping ratios. Nevertheless, Pb incorporation remains crucial to stabilize Sn^{2+} against oxidation.[142] Despite these structural advantages, Sn–Pb perovskites face significant challenges including Sn^{2+} oxidation, non-uniform nucleation, and rapid crystallization. Current research focuses on synergistic strategies combining oxidation suppression[143] and defect passivation[144] to improve the performance of devices.

3.1.2 Suppression of Sn oxidation. The oxidation of Sn^{2+} is generally attributed to a composite factor involving its intrinsic electronic properties, perovskite lattice defects, and external environment. Electronically, the high-lying highest occupied molecular orbital (HOMO) of Sn^{2+} facilitates electron loss. Structurally, defects such as Sn^{2+} and iodine vacancies not only act as trapping centers for free electrons, promoting the generation of charge carriers, but also lead to p-type self-doping and lattice instability. Furthermore, external factors including oxygen, moisture, and common solvents accelerate the oxidation rate of Sn^{2+}.[145] The environmental stability of Sn–Pb perovskites against oxygen and moisture is paramount for their

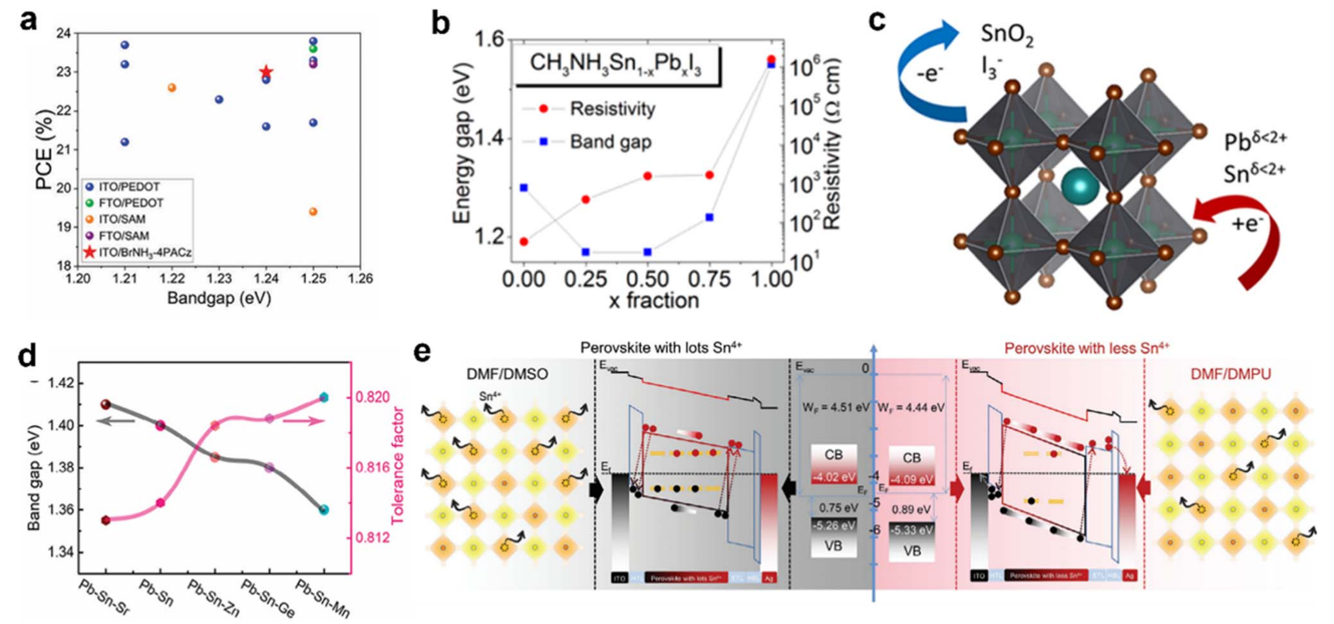

Fig. 7 (a) Literature summary of PCE of NBG devices fabricated on different HTLs over the last 4 years.[138] Copyright 2025, American Chemical Society. (b) Dependence of resistivity and optical bandgap of $CH_3NH_3Sn_{1-x}Pb_xI_3$ on the x fraction is summarized.[141] Copyright 2014, American Chemical Society. (c) X-ray photoelectron spectroscopy reveals two new observations post-thermal annealing that accompany previously reported Sn^{4+} evolution: (i) the formation of I_3^- intermediates preceding I_2 loss at the surface and (ii) evidence of under-coordinated tin and lead surface sites ($Sn^{\delta<2+}$and $Pb^{\delta<2+}$, respectively) under inert and ambient conditions.[147] Copyright 2020, American Chemical Society. (d) Bandgap and tolerance factor values of Pb–Sn–B inorganic perovskites.[148] Copyright 2024, John Wiley and Sons. (e) Energy level schematic diagrams for DMSO- and DMPU-treated perovskite films.[150] Copyright 2023, John Wiley and Sons.

implementation in all-perovskite TSCs. The primary degradation pathway involves the facile oxidation of Sn^{2+} to Sn^{4+}, attributable to the low standard reduction potential (+0.15 V) of the Sn^{4+}/Sn^{2+} couple relative to Pb^{4+}/Pb^{2+} (+1.67 V). This oxidation tendency arises from the absence of lanthanide contraction in Sn, which lacks 4f electrons to effectively shield the 5s/5p valence electrons, resulting in poor outer-shell electron stabilization and consequent vacancy formation.[146]

The most straightforward approach for enhancing the stability of Sn–Pb perovskite devices is through advanced encapsulation. However, conventional packaging methods remain insufficient due to surface-adsorbed oxygen species that trigger Sn oxidation (Fig. 7c).[147] Since complete suppression of oxidation is unattainable, researchers have focused on improving intrinsic oxidation resistance while developing optimized encapsulation techniques. Therefore, additive engineering and surface modification have been widely employed to suppress degradation in Sn–Pb perovskites. B-site co-doping effectively tailors band structures and stabilizes perovskite phases. For instance, Zhang *et al.* developed ternary Pb–Sn–B (B = Ge, Zn, Mn, Ba) inorganic perovskite thin films, with Pb–Sn–Mn exhibiting superior performance, achieving a PCE of 14.34%. Further efficiency enhancement to 17.12% was realized through benzohydroxamic acid (BHA) additive engineering (Fig. 7d).[148] However, achieving uniform B-site dopant distribution remains challenging, often resulting in localized compositional variations that degrade material performance. Thus, optimizing compositional homogeneity could provide an additional pathway to suppress Sn oxidation in Sn–Pb perovskites. Sn–Pb mixed perovskite films typically exhibit compositionally graded profiles with Sn-enriched surfaces, which promote oxidation and accelerate charge recombination. Wang *et al.* demonstrated that diamine additives selectively chelate Sn-atoms, effectively redistributing them from the surface to achieve a more balanced Sn : Pb ratio and enhance oxidation resistance. By incorporating 1,2-diaminopropane, they further improved the spatial homogeneity of the passivation layer, yielding a champion PCE of 23.9%.[149]

Current additive engineering approaches fail to fully eliminate trap states in Sn–Pb perovskites, underscoring the need for more robust oxidation suppression strategies. Conventional solvents like DMF and DMSO exhibit oxidizing properties that promote Sn^{2+} oxidation, while the inherently low solvation capacity of tin halides demands alternative solvents. *N*,*N*′-dimethylpropylurea (DMPU) has emerged as a promising candidate due to its high polarity and low oxidation potential, significantly reducing Sn^{4+} content. The DMPU treatment leads to an upward shift in the Fermi level and CBM, which improve the n-type character of the perovskite film. This enhancement of the built-in electric field promotes charge separation and extraction. Additionally, the increased n-type character and reduction of defect states (such as Sn^{4+} vacancies) suppress trap-assisted non-radiative recombination and prolong carrier lifetime. These changes facilitate more efficient charge separation, transport, and collection, ultimately leading to significant enhancements in V_{OC}, FF, and overall device efficiency (Fig. 7e).[150,151] The oxidation mechanisms of Sn^{2+} remain incompletely understood, with evidence suggesting dual pathways: a direct oxygen reaction and iodine-deficiency-mediated oxidation, where I_2 generation accelerates Sn^{2+} oxidation under illumination, irreversibly degrading the performance of devices.[146,152] Ge *et al.* demonstrated that succinic acid (AA) enhances Sn^{2+} stability by increasing local electron density while forming hydrogen-bond networks with iodide ions, suppressing halide migration and achieving a 28.6% PCE in all-perovskite TSCs.[153] While reducing agents effectively inhibit Sn^{2+} oxidation and passivate defects, research has predominantly focused on their reducing capacity rather than the role of oxidation byproducts. This is a critical knowledge gap requiring further investigation.

In conclusion, the facile oxidation of Sn^{2+} represents a fundamental challenge for Sn–Pb perovskite applications, which involve complex interactions among environmental, chemical, and structural factors. Critical factors encompass intrinsic defects, compositional engineering, and interfacial concentration gradients. Developing effective modification strategies requires a deeper mechanistic understanding of these oxidation processes.

3.1.3 Defect passivation. Despite significant research efforts to enhance the PCE of Sn–Pb PSCs, their performance remains substantially inferior to that of Pb-based perovskite devices, which currently hold a certified efficiency record of 27.3%.[10] This discrepancy is primarily related to the structure of Sn^{2+} and severe oxidation, which can lead to a high density of defect states in both the bulk and surface of perovskite crystals during preparation and application (Fig. 8a).[30,140] To improve the performance, a deeper understanding of defect formation mechanisms in Sn–Pb perovskites is essential. Notably, Sn–Pb perovskites exhibit distinct crystallization kinetics compared to Pb-based analogs, which result in heterogeneous compositional distribution. The rapid crystallization induced by Sn-precursors promotes defect formation, including pinholes, cracks, and impurities, which degrade the quality of film and performance. These challenges have impeded the development of efficient all-perovskite TSCs, highlighting the need for crystallization-rate modulation strategies to achieve high-quality Sn–Pb perovskite films. Fang *et al.* employed functional *N*-(carboxyphenyl) guanidine hydrochloride molecules to modulate crystallization kinetics and grain growth in Sn–Pb perovskites. The additive also acts as an oxidative stabilization agent, effectively suppressing Sn^{2+} oxidation through coordination-mediated electron shielding, thereby enhancing environmental stability. As a result, the certified PCE of all-perovskite tandem solar cells reached 27.35%, with single-junction Sn–Pb devices achieving 23.11%.[154] Similarly, low-dimensional Sn-based perovskite exhibits enhanced oxidation resistance and can serve as an effective antioxidant additive in Sn–Pb perovskite. For instance, SnF_2 improves Sn–Pb perovskite quality through multiple mechanisms: (1) alleviating lattice distortion,[155,156] (2) reducing Sn^{2+} oxidation-induced defect density,[157] and (3) precisely modulating crystallization kinetics to enable highly oriented growth with superior crystallinity.[158] However, a major disadvantage of SnF_2 is interfacial F^- accumulation, which can impede charge transport and necessitates the exploration of

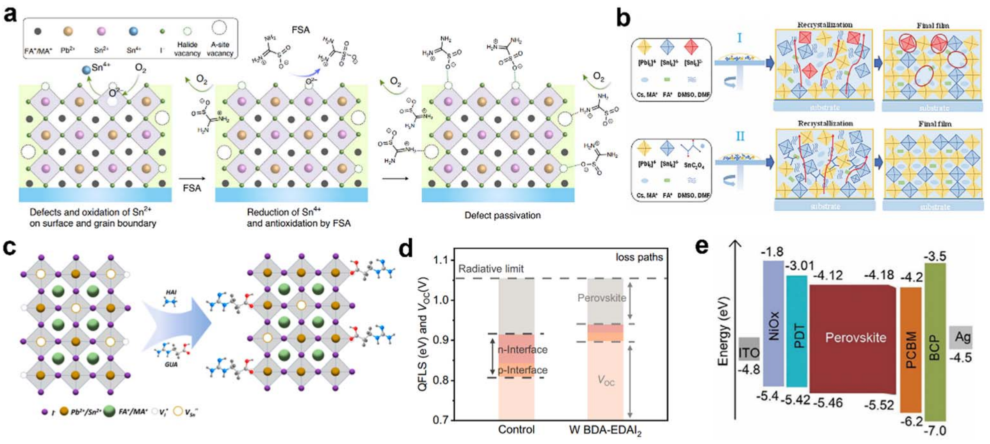

Fig. 8 (a) Schematic of FSA-enabled antioxidation and defect passivation at grain surfaces (film surface and grain boundaries) in Sn–Pb perovskite films. A-site represents the monovalent cation in the perovskites.[30] Copyright 2020, Springer Nature. (b) Schematic diagram of the possible evolution of nucleation or crystallization during the film formation of perovskite with or without SnC_2O_4 treatment.[159] Copyright 2024, John Wiley and Sons. (c) Schematic illustration of defect passivation of Sn–Pb perovskite by GUA and HAI.[165] Copyright 2022, American Chemical Society. (d) Voltage loss mechanism for the control and BDA-$EDAI_2$ modified devices.[167] Copyright 2024, Springer Nature. (e) Schematic energy level of the PSC.[168] Copyright 2020, John Wiley and Sons.

alternative additives. Other Sn halides and Lewis based additives indicate similar benefits in modulated crystallization and defect passivation. Notably, Sn(II) oxalate (SnC_2O_4) effectively coordinates unbound Sn^{2+} and Pb^{2+}, delaying crystallization and reducing Sn vacancy defects. In contrast to SnF_2, the oxalate anion ($C_2O_4{}^{2-}$) provides effective defect passivation and oxidation suppression without causing charge transport limitations, as it avoids the issue of anion segregation.[159]

In addition to additive approaches, solvent engineering offers an effective strategy to regulate the nucleation and growth kinetics of Sn–Pb perovskite crystals. A critical distinction lies in the crystallization barriers: Sn-based perovskites are predominantly limited by the high desorption energy barrier of DMSO molecules, whereas Pb-based perovskites exhibit significantly lower DMSO desorption energy during crystallization.

By precisely controlling the DMSO-to-metal cation (Pb^{2+} and Sn^{2+}) molar ratio during solution processing, the crystallization kinetics can be finely tuned, enabling synchronous crystallization and reduced defect density in Sn–Pb perovskite films. However, DMSO presents inherent limitations—it may induce partial oxidation of perovskite films and offers insufficient suppression of crystallization kinetics. Consequently, the exploration of alternative solvents remains imperative for optimizing Sn–Pb perovskite fabrication.

The performance of perovskite-based devices is strongly influenced by both bulk and surface defects. In Sn–Pb perovskites, surface defect formation is primarily induced by A-site cation depletion, Sn–I bond fracture, and Sn^{2+} oxidation. Effective surface passivation strategies must simultaneously coordinate with surface Sn-ions and suppress Sn^{2+} oxidation.[152,160] Chen *et al.* introduced 4-bromophenylurea (BPU) or 4-bromophenylthiourea (BPSU) into the Sn–Pb perovskite precursor solution, which interacts with precursor components to form clusters, accelerating nucleation while delaying crystal growth, thereby improving surface crystallinity. This approach yielded a certified efficiency of 27.17% for all-perovskite TSCs and 23.87% for Sn–Pb perovskite single-junction devices.[161] Furthermore, Lewis bases can effectively passivate perovskite surface defects through the functional groups. For instance, the hydroxyl group in eco-friendly glucose (Gl) interacts with perovskite surfaces, which can suppress defect states. Similarly, carbonyl groups (C=O) coordinate with Sn^{2+}/Pb^{2+}, promoting vertically oriented 2D perovskite structures that inhibit Sn^{2+} oxidation through structural confinement effects.[151,162] Small molecules containing multiple Lewis-basic functional groups, such as cyanoacetyl hydrazine (CAH) with its carbonyl (C=O), amine (NH_2), and cyano (C≡N) groups, form strong chemical bonds with Sn^{2+}. This interaction reduces defects and enhances charge transport. These passivation mechanisms are enabled by localized lone-pair electrons on nitrogen, oxygen, or phosphorus atoms, which effectively coordinate undercoordinated Sn^{2+} and Pb^{2+} cations. Such passivation strategies successfully mitigate Sn migration and vacancy formation, which are known to cause deep-level defect recombination. Optimized 2D/3D Sn-based PSCs utilizing this approach have demonstrated a PCE of 15.06%.[163]

The above-mentioned defects can significantly affect the optoelectronic performance and stability of the devices. Surface passivation strategies effectively mitigate the defects, which can enhance both device performance and long-term stability. Lee *et al.* treated the upper surface of the Sn–Pb perovskite film with ethylenediamine (EDA), and EDA could coordinate with Sn^{2+} and Pb^{2+}. The interaction between neutral EDA and Sn–Pb perovskite surfaces may influence both coordination stability and the passivation of surface defects. Finally, the EDA modification yielded device efficiencies of over 23% for single-junction PSCs.[164] Brabec *et al.* found that hydrazine iodide (HAI) acts as a post-treatment on the perovskite surface, and βguanidinium propionic acid (GUA) was added to perovskite as an additive to achieve double passivation and significant reduction of Sn^{4+} compounds on the surface. The PCE of modified Sn–Pb PSCs reaches 20.5% (Fig. 8c).[165] Surface reconstruction can be achieved by introducing structural analogs of perovskite components. Li *et al.* demonstrated this approach through post-treatment with 1-(4-fluorophenyl)piperazine (1-4FP), where amine groups formed hydrogen bonds between adjacent perovskite grains, resulting in high-quality films. This strategy enabled Sn–Pb all-inorganic perovskite devices to reach a record efficiency of 17.19% for a bandgap below 1.4 eV.[166]

Considering the multifaceted origins of defects in Sn–Pb perovskite, relying on a single modification strategy is insufficient for complete defect suppression. Chen *et al.* demonstrated a dual-passivation approach using 1,4-butanediamine (BDA) and ethylenediamine diiodide ($EDAI_2$), where BDA passivates Sn^{4+}-related defects while $EDAI_2$ mitigates organic cation and iodide vacancy defects. This strategy yielded high-performance devices with PCEs of 22.65% ($E_g = 1.25$ eV) and 23.32% ($E_g = 1.32$ eV), and enabled all-perovskite TSCs with a certified efficiency of 28.49% ($V_{OC} = 2.12$ V; FF = 83.88%) (Fig. 8d).[167] Besides single-interface passivation, cooperative strategies across multiple interfaces further enhance defect suppression. Yan *et al.* introduced piperazine-1,4-diium tetrafluoroborate (PDT) at the bottom interface to improve energy-level alignment with the HTL, while 2D $Ti_3C_2T_x$ MXene top passivation further optimized the performance of the device, achieving a PCE of 20.45% (Fig. 8e).[168] While polycrystalline perovskite defects predominantly accumulate at grain boundaries, single-crystal perovskite thin films present an alternative research avenue. Although current approaches can modulate crystallization processes and improve film quality, the fundamental mechanisms underlying Sn–Pb perovskite film formation remain incompletely understood. Further investigation of these mechanisms could provide valuable insights for developing novel materials to achieve high-quality perovskite films.

3.2 NBG organic subcells

3.2.1 Materials and morphology. The PCE of OSCs remained stagnant until the advent of NFAs. In particular, the development of the Y-series improves the PCE of OSCs to 20% (Fig. 9a). NFAs are fundamentally characterized by extended π-conjugated architectures and pronounced intramolecular charge-transfer effects, which enhance the absorption capacity in the visible and near-infrared regions. This research further enhances the viability of OSCs for implementation in tandem device structures.[169,170] NFAs typically constructed through strategic integration of electron-donating (D) and electron-withdrawing (A) molecular components, demonstrate superior photovoltaic characteristics. Among them, the A–DA′D–A type 1 acceptors composed of D and A units become the focus of extensive investigation in organic photovoltaics research. The A–DA′D–A acceptor features a highly symmetric and planar rigid fused-ring core (DA′D), which is linked to strong electron-withdrawing end groups *via* π-conjugation, forming an extended conjugated framework.[171] This planar and rigid structure facilitates dense and ordered molecular packing, which promotes electron transport and enhances charge carrier mobility in the film.[172] Furthermore, the energy levels of the HOMO and the lowest unoccupied molecular orbital (LUMO) can be systematically tuned by modifying the chemical structures of the central core D unit and A unit. This enables optimal alignment with the perovskite band energy, which reduces voltage losses and improves the open-circuit voltage.[173] In addition, diverging from the constrained 3D π-conjugation of fullerenes, NFAs provide unprecedented molecular design flexibility. By engineering π-conjugated skeletons, electron-withdrawing terminals, and solubilizing alkyl chains, key parameters including optical bandgaps, energy levels, and solution processability can be precisely tuned to enhance photovoltaic performance. Strategic molecular engineering approaches including (i) aromatic fused-ring expansion to extend conjugation systems, (ii) enhanced π–π stacking interactions in central donor cores, (iii) π-bridging between donor–acceptor segments, and (iv) establishment of quinone resonance structures can be used to broaden absorption bandwidths, intensifyphoton harvesting efficiency, and facilitate 3D charge transport networks, ultimately leading to significant bandgap reduction through synergistic electronic structure modulation. Li *et al.* extended the conjugation of the small-molecule acceptor Y6 by inserting double bonds between its central core and end groups, thereby red-shifting its absorption to 1050 nm and reducing its bandgap from 1.33 eV to 1.21 eV (Fig. 9b).[174] However, device efficiency decreases with a narrowing bandgap.

Conventional morphological regulation strategies aimed at enhancing crystalline ordering in NFAs often paradoxically induce intermolecular excitonic quenching in OSCs, resulting in diminished photoluminescence quantum yield (PLQY) and elevated non-radiative recombination losses due to intensified trap-assisted charge carrier annihilation mechanisms. Sun *et al.* precisely regulated the crystallinity and PLQY of non-fullerene acceptor L8-BO through asymmetric alkyl chain positioning on the thiophene unit, and obtained L8-BO-C4. By introducing the ternary component L8-BO-C4-Br, the device optimization is further realized, and the certified PCE is proved to be 20.1% (Fig. 9c).[175] Side-chain engineering has emerged as an effective strategy for tuning intermolecular packing without compromising the backbone's optoelectronic properties, potentially enabling reduced energy loss. Notably, C-architectured NFAs incorporating uncondensed A-units demonstrate comparable optoelectronic merits to benchmark Y6 derivatives, particularly manifesting intense near-infrared photon harvesting (800–1000 nm range) and narrower optical bandgaps (1.25–1.35 eV). The electron-withdrawing character of apical substituents in the structures exerts a pronounced influence on critical photovoltaic parameters, including exciton dissociation efficiency and charge transport anisotropy.[176,177] Li *et al.* designed and synthesized three small molecule acceptors (FF24-Cl, FM24-Cl, and MM24-Cl) with difluorine, fluorine and methyl and dimethyl groups as apical substituents, respectively. Due to the ideal molecular packing and phase separation size of FM24-Cl,

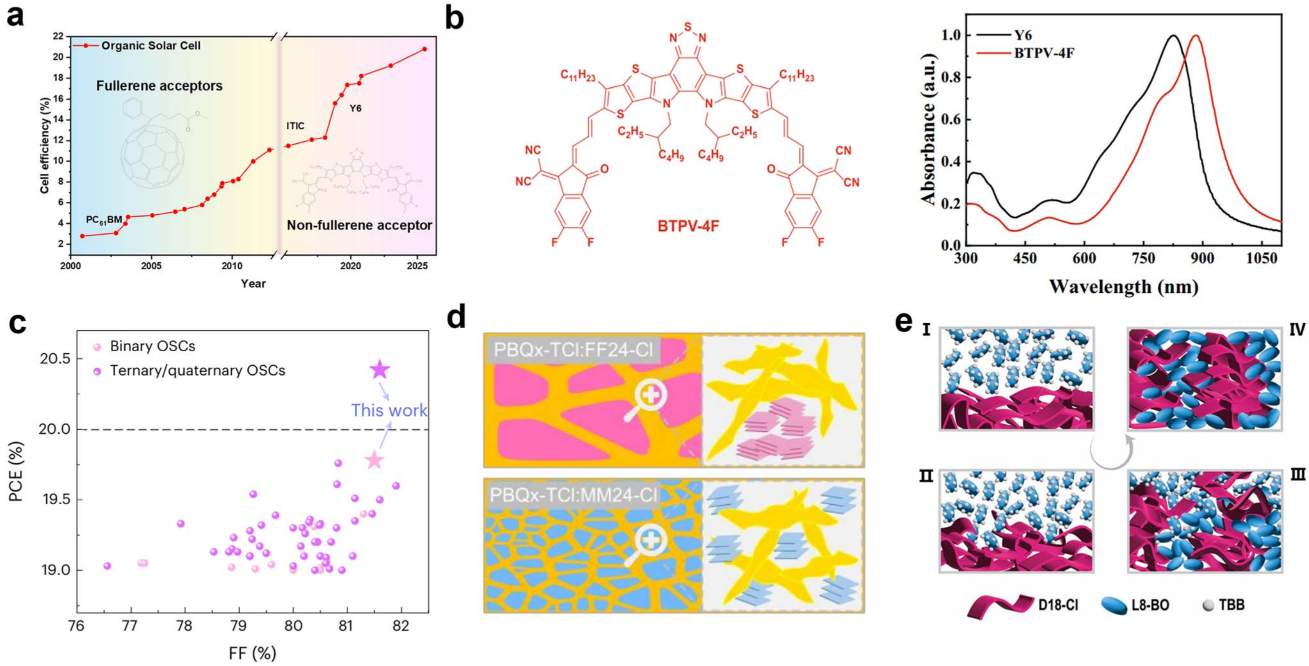

Fig. 9 (a) Development roadmap of OSCs since 2001, and short-circuit current density (J_{SC}) *versus* V_{OC} values of ITIC- and Y6-type NFA-based single-junction OSCs. PCE of OSCs released by the National Renewable Energy Laboratory. (b) Molecular structures of the acceptors BTPV-4F and absorption spectra of the BTPV-4F and Y6 films.[174] Copyright 2021, Springer Nature. (c) Comparison of the PCEs of single-junction OSCs presented in this work and the literature.[175] Copyright 2025, Springer Nature. (d) Schematic diagrams of the blend film based on PBQx-TCl:FF24-Cl/MM24-Cl.[178] Copyright 2024, Royal Society of Chemistry. (e) Schematic illustration of the distinction status from solution to the thin film.[182] Copyright 2023, John Wiley and Sons.

the OSCs with PBQx-TCl as the donor and FM24-Cl as the acceptor show the best exciton dissociation and charge transport performance, thus achieving a PCE of 18.30% (Fig. 9d).[178] The electron-withdrawing character of the apical substituents in NFAs critically influences photovoltaic properties.

Although NFAs exhibit highly ordered molecular packing, their incorporation into blend films alters certain crystalline characteristics. Mainly, the molecular packing in the blend film may be affected by other components. For example, the molecular packing of NFAs can be controlled through peripheral halogen engineering to optimize their performance.[179] Some research studies demonstrate that thermal annealing of NFAs at varying temperatures induces distinct polycrystalline states, significantly modifying their structural properties. Furthermore, the morphology of bulk heterojunction (BHJ) blend films determines the PCE of OSCs by affecting the excitonic dissociation efficiency, charge carrier transport, and material interface properties. The uncontrolled phase separation in BHJ active layers leads to unstable morphological configurations, significantly degrading the optoelectronic performance of the device. Thus, it is very important to precisely control the morphology of the photoactive layer. An effective approach employs additives to control the molecular packing and aggregation morphology of donor and acceptor materials.[180,181] Among them, solid additives with high volatility and easy removal characteristics can prevent excess additive residues and maintain the desired active layer state. Kan *et al.* employed 1,3,5-tribromobenzene (TBB), a solid additive base, which has the characteristics of high volatility and low cost, combined with thermal annealing to adjust the vertical phase of D18-Cl/L8-BO-based OSCs. A PCE of 18.5% is achieved by adding OSCs to TBB (Fig. 9e).[182] Liu *et al.* developed 2-bromo-1,4-dichlorobenzene (VCB), a phase-transformable additive that transitions from liquid to highly volatile solid *via* chlorine atom isomerization on a benzene core. The strategy enables precise control over molecular aggregation during different stages of film formation, facilitating ordered molecular packing and optimized vertical composition distribution. As a result, PM6:L8-BO-based OSCs achieved a PCE of 19.51%.[183] In addition to the chemical material structure of binary components, non-radiative recombination and trap-assisted charge recombination also limit the further improvement of the efficiency of OSCs. In order to improve the performance of OSCs, the modification method is used to reduce the non-radiative recombination. Particularly effective is the incorporation of a third component, which expands spectral absorption, augments light absorption, betters crystallinity/phase separation and aligns energy levels, thereby boosting the photovoltaic efficiency of OSCs. Kan *et al.* incorporated the wide-bandgap polymer donor PTzBI-dF as a third component into the D18:Y6-based binary device. PTzBI-dF induced a favorable crystal structure that optimized the donor–acceptor network crystallinity and phase separation, ultimately achieving a PCE of 18.84%.[184] Although ternary OSCs can significantly enhance PCE, challenges remain. The uncontrolled distribution of third components in BHJ devices often reduces energy transfer efficiency and may disrupt the active layer morphology. Liu *et al.* developed a local deposition strategy to fabricate bulk heterojunctions with controllable third component distribution (CDBHJ). Compared to traditional BHJ devices, the CDBHJ system demonstrates enhanced energy transfer efficiency from 46.5% to 66.8%, achieving an outstanding PCE of 18.29%.[185] Due to the high stability of fullerene acceptors in the polymer donor phase, incorporating fullerene derivatives as a third component in ternary active layers can reduce polymer aggregation. The miscibility of fullerene and NFA suppresses excessive NFA crystallization.[186] Facchetti *et al.* investigated two fullerene derivatives, ET18 and PCBM, as the third component in the PD:Y6 blend films. These fullerene derivatives can be combined with NFA to significantly improve the material morphology.[187]

Through the synergistic optimization of material design and morphology regulation, PO-TSCs are expected to break through the double bottleneck of efficiency and stability. It becomes the core direction of the next generation of photovoltaic technology. However, the coupled mechanisms between organic phase separation and perovskite degradation under thermal/humidity conditions remain insufficiently understood. Developing *in situ* crosslinking strategies to suppress interfacial ion migration represents a critical research direction.

3.2.2 **Phase separation.** Phase separation in OSCs denotes the formation of compositionally distinct donor and acceptor domains within the active layer through physical or chemical interactions. As a critical morphological feature, it governs device performance by determining charge generation, transport, and collection efficiencies. On the one hand, the large phase separation size leads to the recombination of excitons in the diffusion process, which cannot be effectively separated, and influences the continuous channel of electron transport, ultimately reducing electron mobility and the FF.[188,189] An exciton may fail to reach the donor–acceptor (D/A) interface within its limited diffusion length. On the other hand, too small phase separation size is not conducive to the formation of an interpenetrating network structure, impairing charge transport and increasing exciton recombination due to insufficient charge escape pathways (Fig. 10a).[189,190] Ideal phase separation can make the donor and acceptor form a continuous interpenetrating network structure, maximizing exciton dissociation at abundant interfaces while maintaining efficient charge transport pathways.[191] The morphological evolution of BHJ films is fundamentally governed by several key factors, including the intrinsic properties of the material, the donor–acceptor stoichiometry, and the post-deposition treatment scheme, which all work together to regulate the phase separation kinetics in organic photovoltaic composites.

Recent studies reveal that molecular design strategies critically influence the film formation kinetics in OSCs, enabling precise control over phase separation within the active layer. Given that active layer morphology directly determines OSC photovoltaic performance, this control is essential for device optimization. Hou *et al.* designed a non-fullerene receptor HLG by using hydrophobic 1,2,4, 5-tetrafluoro-3 – (2-ethylhexyl) oxygen benzene as the side chain. The fluorinated substitutions enhance the acceptor's surface energy, promoting favorable phase separation in the active layer. The PB2:HLG:BTP-eC9-based OSCs exhibit an impressive PCE of 19.5%.[192] Current high-efficiency OSCs based on A–DA′D–A-type SMAs are mainly processed with toxic halogen solvents like chloroform or chlorobenzene. When non-halogen solvents are used to process the active layer of OSCs, the small molecule acceptors exhibit excessive aggregation during film formation, leading to unfavorable large-scale phase separation. Therefore, developing effective strategies to suppress molecular aggregation and achieve optimal phase-separated domains in non-halogen solvent systems remains a critical challenge. Li *et al.* synthesized two isomeric giant molecule acceptors (GMAs, EV-i, and EV-o) with an extended longer alkyl side chain (ECOD), where the π-spacer was strategically attached to either the inner (EV-i) or outer (EV-o) carbon of the phenyl end group to enhance non-halogenated solvent processability. When processed with *o*-xylene, the PM6:EV-o blend exhibited severe phase separation due to excessive acceptor aggregation, resulting in poor photovoltaic performance (PCE = 2.5%). In contrast, the PM6:EV-i system formed optimal nanoscale phase-separated domains, effectively suppressing charge recombination and achieving a remarkable PCE of 18.27%.[193]

The photogenerated excitons in organic photovoltaic systems undergo directional migration toward donor–acceptor (D–A) heterojunctions prior to charge separation. Due to the intrinsic exciton diffusion length limitation (<10 nm), efficient free carrier generation requires nanoscale phase separation with characteristic dimension sizes below ∼20 nm (twice the exciton diffusion length) to ensure complete exciton harvesting.[194,195] The phase separation size in the active layer exhibits dependence on the D/A ratio within the constituent materials, making compositional tuning a direct and effective strategy for morphology control. Sun *et al.* achieved the highest PCE of 16.1% for a PBT1-C-2Cl:Y6-based binary device by controlling the D/A ratio. Increasing the donor content enhanced Y6 aggregation and π–π stacking while enabling precise control of the phase-separation scale (Fig. 10b).[196] Increasing the acceptor proportion enhances exciton generation. However, the generated excitons are not necessarily all effective excitons. Typically, excitons do not play a role until they dissociate into free carriers. If the presence of excess excitons at the D–A interface hinders the exciton diffusion and dissociation process, such problems can be solved by increasing the D–A interface area.[195,197] In recent OSC research, precise modulation of the D/A ratio has emerged as a fundamental and widely adopted methodology for engineering the phase-separated morphology within the active layer, thereby optimizing the photovoltaic performance of these devices.

Precisely controlling the ideal bicontinuous donor is extremely challenging because the process of BHJ film formation is closely related to various preparation conditions. The dynamic nature of active-layer film formation often leads to undesirable phase separation during thermal annealing. For NFAs, aggregation behavior exhibits strong temperature dependence: excessively low annealing temperatures hinder the formation of well-ordered interpenetrating networks, while

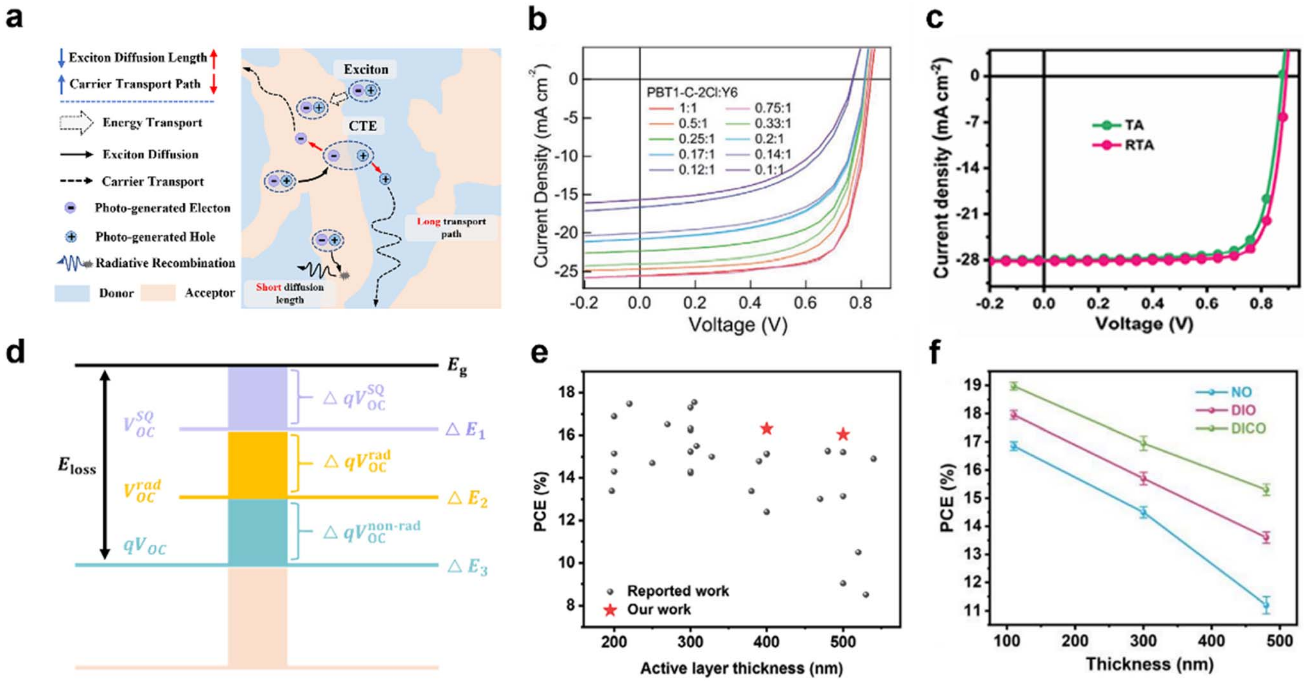

Fig. 10 (a) Charge carrier dynamics in a conventional BHJ film. (b) J–V characteristics of opaque devices with different D/A weight ratios under simulated AM 1.5 G irradiation (100 mW cm^{-2}).[196] Copyright 2020, John Wiley and Sons. (c) Schematic diagram of normal TA and RTA for the active layer. Schematic diagram of energy loss of OSCs according to Shockley–Queisser theory.[198] Copyright 2024, John Wiley and Sons. (d) Schematic diagram of energy loss of OSCs according to Shockley–Queisser theory. (e) The development of PCEs with different thicknesses of active layers.[208] Copyright 2024, John Wiley and Sons. (f) The dependence of PCEs on the active layer thickness.[209] Copyright 2020, Royal Society of Chemistry.

prolonged or high-temperature annealing induces excessive phase separation. Traditional thermal annealing relies on bottom-up conductive heating, which indirectly affects the active layer and limits precise morphological control. In contrast, direct thermal conduction to the active layer could enable finer morphological tuning. Therefore, developing novel annealing methods is critical for advancing OSC performance. Zhang *et al.* designed an innovative annealing method for preparing films called reverse thermal annealing (RTA), mainly by inverting the active layer on the annealing table. This annealing method can retard the evaporation of residual solvent while optimizing phase separation and vertical component distribution within the active layer. The enhanced morphology significantly reduces non-radiative recombination losses, enabling the PM6:L8-BO-X devices to achieve an efficiency improvement from 18.98% to 19.91% (Fig. 10c).[198]

BHJ films frequently demonstrate vertical phase separation, which critically controls charge transport and nonradiative composite losses in OSCs. The active layer formation represents a dynamic non-equilibrium process involving competing mechanisms, necessitating fundamental investigations into crystallization kinetics and interfacial evolution pathways. While state-of-the-art fabrication methods primarily utilized thermal evaporation, aerosol deposition, and solution-treated film transfer strategies, significant limitations remain in achieving optimal D–A organization. The primary limitation lies in precisely controlling the delicate balance between acceptor self-aggregation and material compatibility, which ultimately determines device efficiency and operational stability.

3.2.3 Energy loss.

The PCE of OSCs is fundamentally limited by energy loss (E_{loss}), which mainly manifests as thermodynamic loss ($\triangle E_1$), radiation compound loss ($\triangle E_2$) and non-radiation compound loss ($\triangle E_3$) (Fig. 10d).[199–201] These losses will directly affect the V_{OC} and PCE of the device. A critical approach involves optimizing the energy level alignment between the HOMO of the donor and LUMO of the acceptor, as this interfacial energetics governs charge extraction efficiency. Consequently, precise energy level matching represents a key parameter for minimizing E_{loss} and enhancing device performance.[202] Despite significant progress in developing A–D–A-type NFAs, most of the polymer donors have problems such as energy level mismatch and different material quality, which hinder the further improvement of OSC device performance. For example, Sun *et al.* designed an A–DA′D–A type acceptor, PEH-F. The energy level of a donor (PTQ11) aligns with that of the PEH-F acceptor, while the PTQ11:PEH-F-based OSCs attain a minimal E_{loss} of 0.511 eV and demonstrate effective exciton separation. Finally, the PTQ11:PEH-F-based binary device achieves an excellent PCE of 19.73%. As mentioned above, the majority of research focuses on developing new units to fine-tune the energy levels of materials. While such advances demonstrate the effectiveness of molecular design in energy-level optimization, challenges persist in material reproducibility and morphological control during film formation.

Consequently, developing direct strategies to precisely tune polymer donor energy levels remains crucial for minimizing E_{loss} and advancing OSC performance.[203]

Nonetheless, there are many uncertain factors in the research of new materials, including poor reproducibility due to morphological instability during film formation. Thus, developing straightforward strategies to precisely modulate polymer donor energy levels represents a critical research direction for minimizing E_{loss} in OSCs.[204,205] Among them, the introduction of electron-deficient units as the third component can optimize energy level matching and reproducibility simultaneously. Duan *et al.* designed a donor polymer (PBFBX) based on the electron-deficient 5,6-difluorobenzo[*c*][1,2,5]oxadiazole (ffBX). The energy level of donor PBFBX can be regulated by increasing the content of ffBX, leading to reduced E_{loss}. The PCE of the PBFBX-20:Y6-BO-based device is 17.5%, and the repeatability of the device is improved.[206] The suppression of electron–phonon coupling can be achieved by reducing the free volume ratio, and concurrently strengthening lattice ordering, thereby diminishing non-radiative recombination losses. This strategy was demonstrated in the molecular design of AQx-H, where the incorporation of cyclohexane effectively inhibits excessive molecular aggregation, widens spectral absorption, and optimizes energy level alignment. The modifications enabled AQx-H-based devices to attain a V_{OC} of 0.923 V and the best PCE of 19.5%, showcasing an effective approach for minimizing E_{loss}.[207]

The interface electronic structure and E_{loss} mechanisms, as critical physical properties of OSCs, are essential for understanding the operational principles of OSCs. This understanding serves as a cornerstone for formulating innovative strategies to enhance their photovoltaic performance. Device engineering including structural design, process optimization, and interface modulation, represents a key approach for advancing OSC technology.

A core focus of structural design lies in optimizing the active layer thickness and interfacial treatment, which synergistically enhance device performance by balancing charge generation, transport, and extraction efficiencies. The active layer thickness needs to balance the light absorption and carrier transmission efficiency. An excessively thin active layer reduces photon absorption efficiency and shortens charge carrier diffusion lengths, leading to increased recombination losses. In addition to the charge recombination problem, the too thick active layer can also lead to an increase in the diffusion length of charge carriers in the cell, reducing the generation of effective carriers, and may also lead to poor contact between the transport layer and the active layer (Fig. 10e).[208] To obtain the best battery performance, the thickness of the active layer should be controlled within an appropriate range. The performance-thickness trade-off in OSCs originates from the conflicting requirements of optical absorption (needing thick layers) and charge collection (limited by short exciton diffusion lengths in BHJs). And the low exciton diffusion length leads to severe charge recombination of the device. Yang *et al.* demonstrated that the solvent additive, 1,5-diiodocycloctane (DICO), can effectively extend the exciton diffusion distance of BHJ films. This enabled PM6:L8-BO-based OSCs to achieve thickness-insensitive performance, maintaining a high PCE of 19.1% even with a 110 nm active layer (Fig. 10f).[209] Beyond alterations to the active layer, interfacial engineering enhances OSC performance. Researchers have explored electrode interface modifications by optimizing the surface energy levels of electrodes, notably through techniques such as ultraviolet-ozone treatment and SAMs. These interfacial adjustments effectively improve charge transport properties by enhancing carrier extraction efficiency at critical device interfaces.[210,211] Device engineering of OSCs is gradually breaking through the limitation of efficiency and stability through multi-scale collaborative optimization.

4. Present status of solution-processed PeTSCs

4.1 Perovskite/perovskite TSCs

4.1.1 Optical design. All-perovskite TSCs represent a promising route to surpass the S–Q limit of single-junction PSCs, with a certified PCE reaching 30.1%. To overcome the inherent S–Q limitation of single-junction devices, optimizing the optical design by leveraging perovskites' tunable optoelectronic properties is essential. This involves maximizing light absorption, carrier transport, and interface characteristics to enhance efficiency. Specifically, the optical design targets broad solar spectrum absorption through spectral splitting between the WBG and NBG perovskite subcells. In this design, the front WBG subcell primarily absorbs high-energy photons in the UV-visible range (300–750 nm), while the rear NBG subcell efficiently captures near-infrared photons (>750 nm). The structure enhances spectral utilization by minimizing transmission losses and suppressing carrier thermalization losses characteristic of single-junction devices. By synergistically optimizing photon management across complementary spectral regions, this approach significantly suppresses energy dissipation and enhances PCE.[137,212]

While all-perovskite TSCs exhibit enhanced spectral utilization, their J_{SC} typically underperforms compared to that of their single-junction counterparts. This limitation is derived from the intricate current-matching requirements between the WBG front subcell and NBG rear subcell, where mismatched photocurrent generation induces compounded losses in tandem configurations.[30,154] The reduced J_{SC} originates primarily from thermodynamic losses in the front subcell and insufficient infrared photon harvesting in the rear subcell. To mitigate these issues, bandgap engineering through compositional adjustments enables precise spectral responsivity tuning, and thickness optimization of photoactive layers balances absorption depth with carrier extraction efficiency. Coordinated optimization of these parameters is essential to align current generation across subcells, thereby minimizing parasitic losses characteristic of TSCs.

Traditionally, high-efficiency PSCs mainly adopted the structure of n–i–p. The p–i–n structure is mainly applied to all-perovskite TSCs. This shift stems from the limitations of Spiro-

OMeTAD, the HTL material used in record-efficiency n–i–p single-junction PSCs. Compared to the C_{60} ETL in p–i–n devices, Spiro-OMeTAD exhibits strong parasitic absorption and significant interfacial reflection, leading to substantial optical losses in all-perovskite TSCs. To address these challenges, Ye *et al.* developed a hole-selective transparent passivation contact by introducing crosslinkable p-type small molecules into the antisolvent process. The interface reflection and parasitic absorption are effectively reduced. The resulting device achieves one of the highest independently certified PCEs reported for n–i–p perovskite/Si TSCs (Fig. 11a).[213] Furthermore, other studies have reported the construction of double-sided battery structures based on optical design. By employing TCOs as back electrodes, these devices enable simultaneous light absorption from both front and rear sides, significantly enhancing photon harvesting efficiency.[214]

Interface reflection losses significantly degrade the spectral absorption efficiency in all-perovskite TSCs. Currently, two primary strategies are employed to mitigate these losses: (1) implementation of front-side anti-reflection coatings to minimize photon escape, and (2) incorporation of light-trapping architectures (*e.g.* textured or curved structures) to enhance internal light absorption. Fang *et al.* developed a nanostructured composite interlayer by depositing highly dispersed tin fluoride oxide nanoplates (NP-FTO) onto a glass substrate, followed by ALD of a thin SnO_2 coating. The incorporation of NP-FTO architecture demonstrated dual functionality, effectively reducing optical reflection, while simultaneously modulating perovskite crystallization dynamics. The optimized optical structure enabled an all-perovskite TSC with a certified PCE of 28.2% (Fig. 11b).[215]

4.1.2 Carrier recombination dynamics. Despite the rapid development of all-perovskite TSCs, their performance remains limited due to carrier recombination dynamics. Carrier dynamics is predominantly governed by three interrelated mechanisms: carrier transfer, transport and recombination processes, which can be described by drift-diffusion models.[216,217] All-perovskite TSCs are composed of two perovskites exhibiting analogous carrier dynamics to single-junction PSCs. Photon absorption with energies exceeding the bandgap ($E \geq E_g$) promotes electronic transitions from the valence band, triggering either exciton formation or direct generation of mobile charge carriers through band-to-band transitions.[104,218] Energetic carriers above the CBM or below the VBM undergo thermalization to band edges through electron-phonon coupling (processes 1 and 2 in Fig. 11c).[219] Thermal relaxation of the charge carriers leads to energy loss in the device. Photogenerated charge carriers within the perovskite undergo

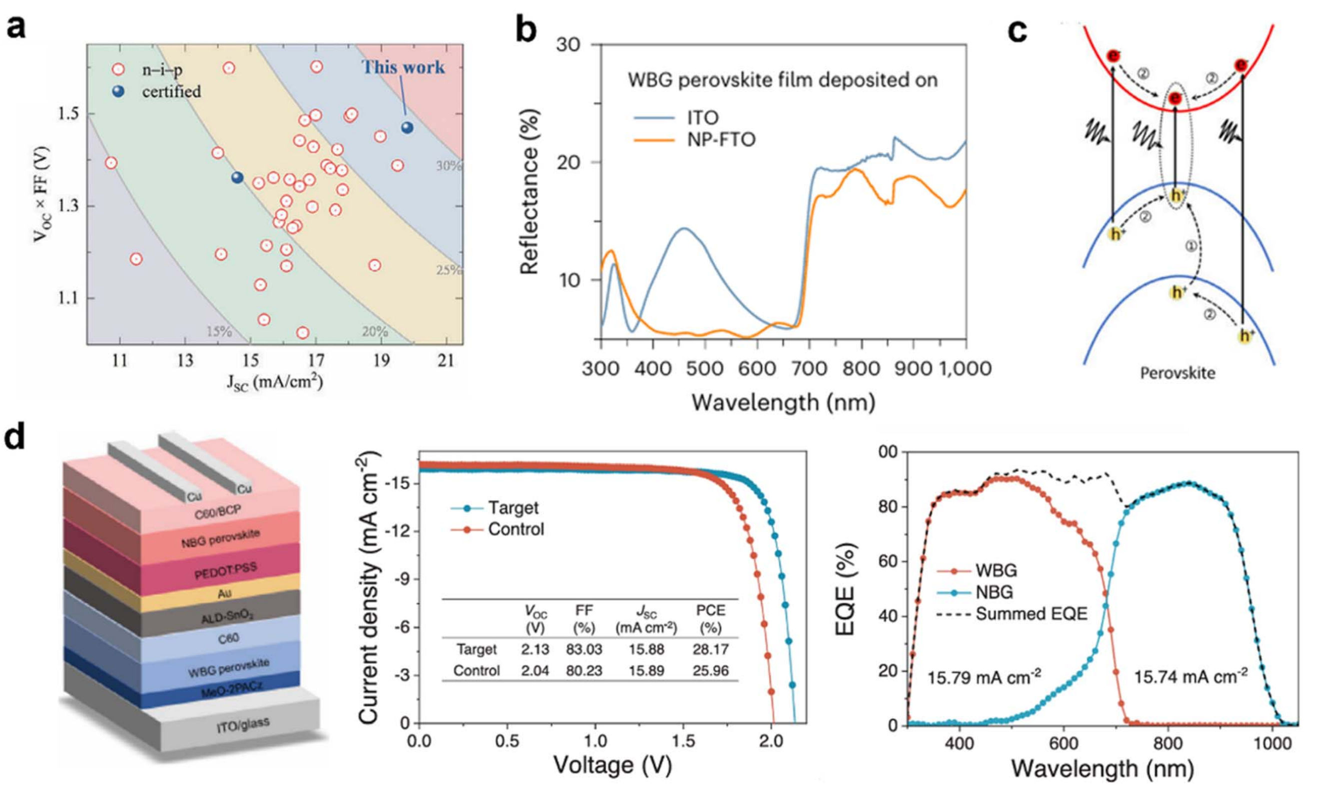

	V_{OC} (V)	FF (%)	J_{SC} (mA cm^{-2})	PCE (%)
Target	2.13	83.03	15.88	28.17
Control	2.04	80.23	15.89	25.96

Fig. 11 (a) Comparisons of n–i–p perovskite/silicon TSCs in terms of J_{SC} *vs.* $V_{OC} \times$ FF product.[213] Copyright 2025, John Wiley and Sons. (b) Reflectance spectra of WBG perovskite films deposited on ITO and NP-FTO.[215] Copyright 2025, Springer Nature. (c) Schematic illustration of charge-carrier generation, relaxation, and sub-band transition in the halide perovskite semiconductor.[219] Copyright 2022, John Wiley and Sons. (d) The device structure schematic diagram, *J*–*V* curves of control and target all-perovskite TSCs, and EQE spectra of the best tandem device.[221] Copyright 2024, John Wiley and Sons.

diffusion-drift transport mechanisms, migrating toward the perovskite and CTL interface under the influence of the built-in potential gradient. At the interface, the built-in electric field promotes carrier injection into the CTL, where subsequent carrier diffusion is collected at the device electrodes. However, part of the charge carriers generated by the WBG front cell and the NBG rear cell of the all-perovskite TSCs will migrate into the ICL. Previous studies reported that charge carriers from different subcells will be transferred to TCO or metal layers for recombination. The reason for this occurrence could be that, in contrast to the CTL, TCO and the metal layer exhibit greater carrier conductivity, which provides a preferential recombination pathway for carrier transport.[220]

However, the recombination position of charge carriers remains to be studied, as energy losses during diffusion critically limit device performance. Xu *et al.* demonstrated a defect passivation strategy employing the molecular modifier 4-(trifluoromethyl) benzhydrazide (TFH), which simultaneously mitigates defect-mediated recombination in Sn–Pb perovskite films and provides chemical anchors at the perovskite interface, thereby promoting the transport of charge carriers (Fig. 11d).[221] In addition, non-radiative recombination in the WBG subcell significantly degrades all-perovskite TSC performance. Mitigating bulk defects in the perovskite layer suppresses this recombination loss. Previous studies indicate that perovskite crystals with the (100) orientation have higher carrier mobility and lower defect density than perovskite crystals with the (110) or (111) orientation.[35] Li *et al.* developed a crystallization-modification strategy using nicotinamide and its derivative additive, where isonicotinamide (IA) molecules preferentially induced epitaxial growth along the (100) crystallographic plane in WBG perovskite films. Finally, an efficient WBG PSC was prepared, with an efficiency of 19.34% and a V_{OC} of 1.342 V. The efficiency of the optimized all-perovskite TSCs reached a PCE of 28.53%.[222]

In all-perovskite TSCs, the ICL governs device performance through its influence on carrier dynamics. Charge carriers transferred from both subcells to the ICL undergo significant recombination, which can severely limit overall efficiency. However, asymmetric carrier injection between subcells (manifested as imbalanced electron and hole amounts) induces residual charge accumulation at the ICL/perovskite interfaces. This interfacial charge accumulation generates parasitic electric fields that obstruct carrier extraction, resulting in the splitting of the Fermi level and the E_{loss} at the ICL, ultimately reducing V_{OC} and FF through enhanced non-radiative recombination pathways. To mitigate this, some studies have introduced dense ALD-SnO_x layers in the ICL to suppress halogen ion migration and prevent electrode corrosion-induced carrier accumulation.[134,223] Zhao *et al.* developed an ICL of C_{60}/SnO_2/IZO/PEDOT:PSS to protect the bottom films. Based on this ICL structure, the all-perovskite TSC with an area of 1.044 cm^2 achieved a certification efficiency of 26.4%.[224] The V_{OC} loss at the ICL provides a critical diagnostic metric for assessing charge-carrier equilibrium in all-perovskite TSCs, directly reflecting the balance of photogenerated carriers in series-connected junctions.

4.2 Perovskite/organic TSCs

4.2.1 Optical design. In addition to all-perovskite TSCs, PO-TSCs have emerged as promising alternatives, leveraging the non-toxicity, near-infrared absorption, and mechanical flexibility of OSCs. While early PO-TSC development was limited by the modest efficiency of OSCs, recent advances in NFAs (*e.g.* Y6) and polymer donors (*e.g.* PM6 and D18) have significantly improved OSC performance. Although PO-TSCs currently exhibit lower efficiencies than other PeTSCs, the organic rear cells offer unique advantages in spectral tuning through flexible acceptor design. WBG PSCs in PO-TSCs efficiently harvest photons across the visible and near-infrared (300–750 nm) spectra, while NBG OSCs extend absorption beyond 750 nm. By synergistically broadening the spectral response, PO-TSCs surpass the efficiency limits of single-junction devices. Theoretical calculations suggest that optimal bandgap tuning could push PO-TSC efficiencies toward ~40% (Fig. 12a).[11]

The bandgap of WBG PSCs can be precisely tuned from 1.6 to 2.3 eV through compositional engineering at the A, B, and X sites. While a 1 : 1 I : Br ratio yields an optimal 1.85 eV bandgap, excess Br content accelerates crystallization kinetics, introducing intrinsic defects and light-induced phase segregation.[26,46,225] Therefore, bandgap optimization must balance spectral matching with OSC subcells against material stability.[25] The optical thickness of WBG PSCs in PO-TSCs critically influences both photon absorption and charge transport. Increasing the perovskite layer thickness induces a redshift in the absorption spectrum, while thinner films promote more efficient charge carrier extraction. An optimal thickness must therefore balance these competing effects to maximize tandem device performance.

The optimal bandgap selection for OSCs is dependent on the spectral complementarity with WBG PSCs in a tandem structure. Through ternary blending strategies employing NBG NFAs, the OSC absorption range can be precisely tuned. The strategy of introducing the third component is mainly through the complementary absorption of two narrow- bandgap NFA receptors, thereby broadening the near-infrared absorption range. Bo *et al.* introduced BTP-eC9-4F and L8-BO as receptors, which could effectively improve the absorption of near-infrared photons. The ternary OSCs based on D18:BTP-eC9-4F:L8-BO achieved a PCE of 19.2%. When integrated into PO-TSCs, the overall device efficiency was enhanced to 24.5%, demonstrating the effectiveness of this material combination for tandem applications (Fig. 12b).[226] Unlike perovskites, where free carriers are generated directly, OSCs rely on exciton dissociation at donor–acceptor interfaces.[227] However, introducing a third component can complicate film growth, potentially degrading film quality and increasing exciton recombination losses. To solve this problem, the third component should promote crystallization, enhance charge transfer states, and improve molecular packing order, thereby reducing non-radiative recombination. Zhu *et al.* designed an acceptor, AQx-2F, featuring low recombination energy, suppressed electron–phonon coupling, and reduced exciton binding energy. The champion ternary OSCs based on D18:AQx-2F:eC9 achieve the

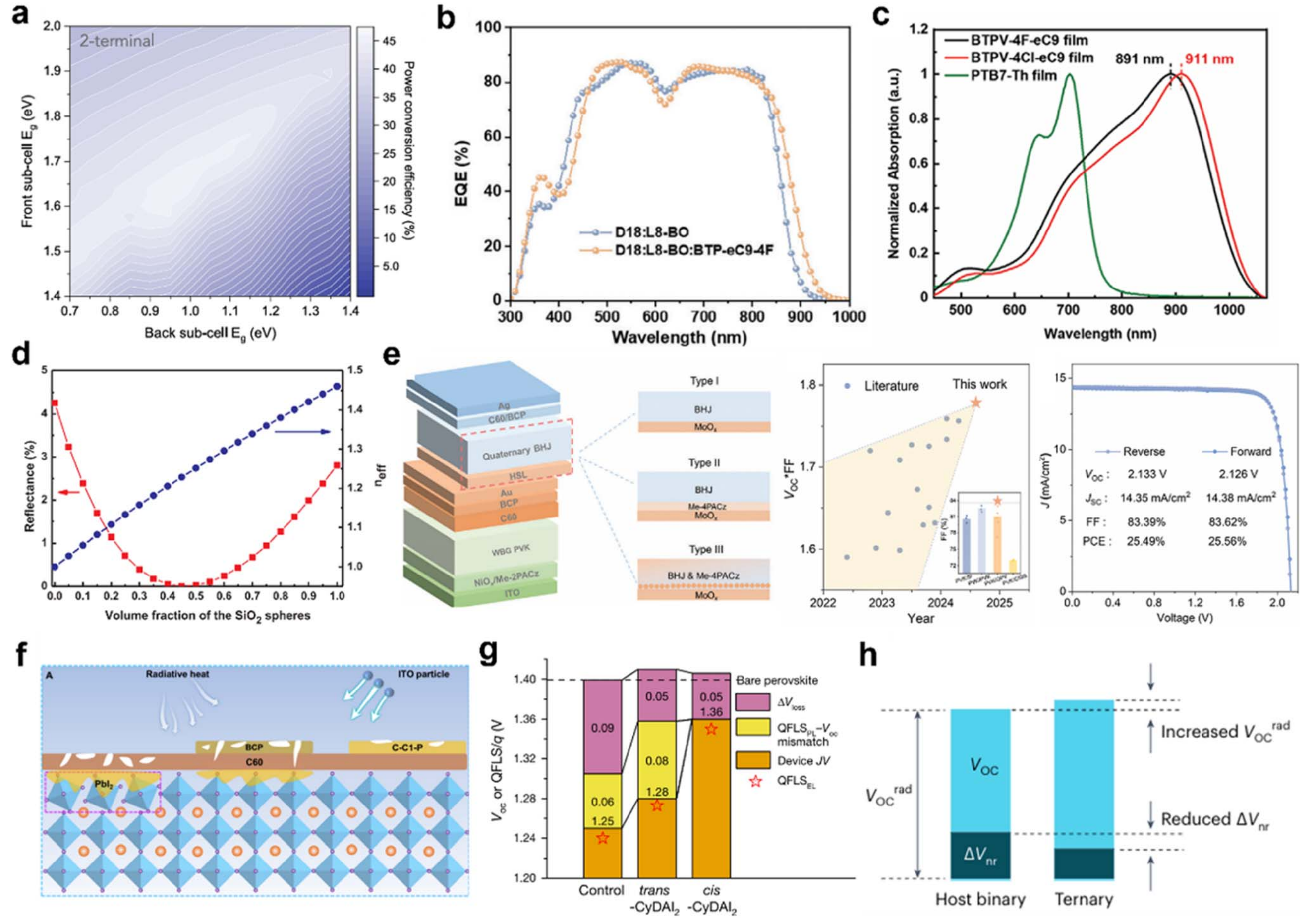

Fig. 12 (a) S–Q limit of TSCs with 2-terminal configurations.[11] Copyright 2023, Elsevier. (b) EQE spectra of the binary and ternary OSCs.[226] Copyright 2024, John Wiley and Sons. (c) Absorption spectra of the films of PTB7-Th, BTPV-4F-eC9, and BTPV-4Cl-eC9.[229] Copyright 2022, John Wiley and Sons. (d) Reflectance for quarter-wave thickness silica coating on glass. The effective refractive index n_{eff} of the coating is plotted on the right axis.[231] Copyright 2018, Elsevier. (e) Device configuration of PO-TSCs; the red frame highlights the ICL structure with different HSLs in an organic subcell; summary of the V_{OC}-FF product of reported high-performance PO-TSCs. Inset: summary of FFs of reported high-performance perovskite/silicon TSCs, perovskite/perovskite TSCs, PO-TSCs, and perovskite/CIGS TSCs; J–V curves of champion PO-TSCs at forward and reverse scans.[232] Copyright 2024, John Wiley and Sons. (f) A schematic illustration of the mechanism of protecting perovskite from damage during the ITO sputtering process.[236] Copyright 2023, John Wiley and Sons. (g) Voltage losses are summarized by comparing QFLS$_{PL}$ (from film PLQY), QFLS$_{EL}$ (from device ELQY), and device V_{OC}. Except for the cis-CyDAI$_2$-treated PSCs, a QFLS$_{PL}$–V_{OC} mismatch is observed, whereas QFLS$_{EL}$ aligns with the V_{OC}.[28] Copyright 2024, Springer Nature. (h) Strategies to improve the V_{OC} in 2T OSCs: the improved V_{OC} can result from both increased V_{OC} rad and reduced ΔV_{nr}.[243] Copyright 2023, Springer Nature.

highest certified PCE of 20.6% and V_{OC} of 0.937 V.[228] The A–DA′D–A structured NBG small molecule acceptors were selected for the rear subcell to achieve optimal band alignment with the WBG perovskite front subcell. Li *et al.* designed a small molecule acceptor, BTCV-4Cl-eC9, by substituting fluorine atoms with chlorine at the A-terminal group. This structural modification effectively broadened the absorption spectrum of the material. The NBG OSC based on PTB7-Th:BTPV-4Cl-eC9 achieves a J_{SC} of 28.6 mA cm^{-2}. Finally, the optimized PO-TSC delivers a PCE of 22.0% (Fig. 12c).[229] At the same time, bandgap narrowing often exacerbates non-radiative recombination and reduces exciton dissociation efficiency, thereby limiting device performance. Therefore, broadening the absorption spectrum while maintaining a high V_{OC} remains a critical strategy for enhancing photovoltaic efficiency. In contrast to all-perovskite TSCs, PO-TSCs combine flexibility, design versatility, and cost efficiency. The organic rear subcell not only provides encapsulation but also introduces distinct optical properties that are pivotal for optimizing device performance. In the $CH_3NH_3PbI_3$ ($MAPbI_3$) perovskite film, only 65% of the incident light will be absorbed, and the remaining loss is mainly light escape from the device and light reflection.[230] So to obtain higher PCE, it is necessary to optimize the device structure.

Sunlight enters the device through the glass substrate, where inherent surface reflections inevitably reduce light absorption. To mitigate this loss, an anti-reflection coating can be employed. For instance, a SiO_2 nanosphere-based nano-coating was demonstrated to achieve 96.1% maximum light transmittance, enabling $MAPbI_3$-based PSCs to reach a PCE of

15.82% (Fig. 12d).[231] The PCE of PO-TSCs shows strong angular dependence, decreasing significantly under oblique light incidence. This performance degradation primarily results from increased optical losses and aggravated non-radiative recombination at wide incidence angles. Most existing studies focus exclusively on normal incidence conditions, but investigations of angular-dependent performance remain scarce. Developing effective strategies to mitigate these angular-dependent loss mechanisms is therefore crucial for advancing the practical application of PO-TSCs.[210]

4.2.2 **Interconnection depletion.** In PO-TSCs, the ICL plays a crucial role in device performance and stability. An optimal ICL design must satisfy three key requirements: (1) high optical transparency with minimal parasitic absorption, (2) balanced charge transport between subcells to prevent carrier accumulation, and (3) effective chemical protection. For solution-processed PO-TSCs, solvent orthogonality is particularly critical to prevent dissolution of the underlying perovskite layer during subsequent organic cell deposition. In PO-TSCs, orthogonal solvents are used to prepare PSCs and OSCs, which enable sequential processing without compromising either sublayer.

Charge carrier imbalance between the perovskite and organic active layers can induce significant charge accumulation, thereby reducing the FF in PO-TSCs. To mitigate this issue, optimizing charge transport dynamics between subcells is essential for achieving high-performance devices. Zhu *et al.* introduced Me-4PACz into the BHJ, where it spontaneously self-assembled at the bottom interface to form a MoO_x/Me-4PACz double-hole transport layer structure in the ICL. This modification improved energy level alignment and enhanced charge extraction efficiency. The resulting PO-TSCs with a C_{60}/BCP/Au/MoO_x/Me-4PACz structure achieved a PCE of 25.56% (certified 24.65%) and a FF of 83.62% (Fig. 12e).[232] Sputtering and ALD are widely employed for fabricating metal oxide films in ICL. Among them, TCO is an excellent material, which attracts much attention due to its outstanding light transmittance and excellent conductivity. It exhibits a transmittance exceeding 90% across both the visible and near-infrared spectral regions. TCO currently employed in perovskite solar cells primarily consists of three types: ITO, FTO, and aluminum-doped zinc oxide (AZO). Each of these materials exhibits distinct characteristics and varies in terms of performance and cost. In addition to the mentioned three types, alternative TCO materials are also being actively explored within the research community.[233] For example, Hou *et al.* developed a high-transmittance ICL comprising BCP/IZO/MoO_x, where the sputtered IZO layer exhibited superior surface coverage and increased recombination sites, thereby enhancing charge recombination efficiency. The resulting PO-TSCs achieved a PCE of 23.6%.[31] Riedl *et al.* employed ALD to fabricate an InO_x-based recombination layer, which formed a highly compact interfacial structure. It simultaneously establishes ohmic contact and minimizes optical losses. The resulting PO-TSCs obtained a PCE of 24.0% with a V_{OC} of 2.15 V.[33] However, sputtering may induce film damage due to high-energy ion bombardment, while ALD typically incurs higher fabrication costs.[234] Optimizing device fabrication processes remains crucial for advancing TSCs. Recent studies demonstrate that evaporated ultrathin metal films offer a promising alternative approach. Au films enhance device efficiency and stability *via* improved ohmic contacts and majority carrier recombination, and their high cost and electron barrier limitations restrict large-scale applications. The commonly used Ag film has a suitable energy barrier, but there will be corrosion problems and serious parasitic absorption problems.[124,125] Therefore, researchers have developed an Ag/Au bilayer architecture that simultaneously optimizes the electron energy barrier for efficient carrier tunneling while maintaining high optical transparency. As a result, PO-TSCs exhibit an excellent PCE of 23.26%.[235] However, the implementation of ICLs based on thin metal layers may introduce significant optical losses, which will seriously affect the efficiency of the TSC device and J_{SC} of the rear cell. Tan *et al.* developed a dual-functional organic molecule, 4,7-bis((4-vinylbenzyl)oxy)-1,10-phenanthroline (denoted as C1), as a sputtering buffer layer (SBL). Upon thermal cross-linking, the styrene groups in C1 exhibit exceptional sputtering resistance. Moreover, C1 possesses high electron mobility, effectively mitigating sputtering-induced damage and interfacial charge accumulation in the ICL. The resulting PO-TSC achieves a PCE of 24.07% (Fig. 12f).[236]

4.2.3 **Reducing voltage loss.** PO-TSCs integrating WBG PSCs and NBG OSC subcells with an ICL exhibit lower efficiency than alternative tandem structures. This diminished performance is primarily attributed to significant V_{OC} losses, which originate from two critical components: (1) inherent limitations in the WBG PSCs and (2) suboptimal characteristics of the NBG OSCs. Specifically, V_{OC} losses in WBG PSCs arise from interfacial recombination and halide segregation under operational conditions, while NBG OSCs suffer from non-radiative recombination due to insufficient energy-level alignment and morphological instability in the active layers.[61,82,83,115] These collective challenges hinder the realization of ideal V_{OC} additivity and current matching, ultimately constraining the efficiency of PO-TSCs. As discussed, the Br-rich composition in WBG perovskite subcells induces phase segregation under illumination while generating high defect densities, both contributing to significant V_{OC} losses. Recent strategies to mitigate these losses focus on suppressing phase segregation and minimizing defect formation. Tao *et al.* effectively suppressed phase segregation in WBG PSCs through the synergistic action of $Pb(SCN)_2$ and 2-thiopheneethylammonium chloride (TEACl). The incorporation of $Pb(SCN)_2$ modulated crystallization kinetics, yielding larger perovskite grains with reduced boundaries, thereby minimizing phase segregation. Meanwhile, TEACl passivates the surface defects of WBG PSCs. The modified PO-TSCs exhibit a PCE of 22.29% and a V_{OC} of 2.072 V.[234] The incorporation of additives can effectively tune optoelectronic properties, and it may also perturb perovskite crystallization dynamics, potentially exacerbating non-radiative recombination losses. Concurrently, surface defects in perovskites act as dominant carrier trapping centers, and the defects may induce ion migration in the perovskite, resulting in V_{OC} losses in WBG PSCs and compromising the efficiency and stability of PO-TSCs. Chen *et al.* developed a tryptophan (TRP) molecule-assisted iodine capture strategy to suppress UV-light-induced degradation and phase segregation, caused by halogen ion migration from the NiO_x side. The optimized charge transport and minimized non-radiative recombination at the interface boost the efficiency up to 19.04% with a V_{OC} of 1.30 V, which is the highest V_{OC} for the NiO_x-based WBG PSCs without a SAM.[237] These challenges highlight the crucial need for surface passivation strategies to suppress recombination and enhance interfacial charge extraction.

In WBG PSCs, serious interface recombination predominantly occurs at the perovskite/C_{60} interface, where surface states induce pronounced band bending at the electron quasi-Fermi level. Li *et al.* designed a *cis*-passivating agent, 1,4-diammonium diiodide (*cis*-$CyDAI_2$), which elevates the perovskite surface Fermi level, thereby suppressing band bending at the electron quasi-Fermi level and improving contact with the electron transport layer. Finally, the modified PO-TSCs obtained a certified PCE of 25.7% (Fig. 12g).[28]

In OSCs, energetic disorder and trap states promote non-radiative recombination and reduce the quasi-Fermi level splitting (QFLS), leading directly to V_{OC} loss. Inferior charge carrier mobilities result in imbalanced transport, enhanced recombination, and increased series resistance, which constrain the FF and further limit the V_{OC}.[238,239] Moreover, the organic active layer is susceptible to phase separation, molecular rearrangement, and chemical degradation upon exposure to light, heat, or air, resulting in performance instability.[228] These disadvantages are especially pronounced in NBG OSCs. Therefore, when employed as the bottom cell in perovskite–organic tandem solar cells, systematic optimization of material design and interface engineering is essential to mitigate these issues.

In PO-TSCs, the rear subcell typically employs ternary OSCs, where a third component is incorporated into the binary blend to extend the spectral absorption range and enhance photocurrent generation.[240,241] Subsequent studies revealed that incorporating the third component can enhance V_{OC}, although the underlying mechanism remains unclear. The V_{OC} mechanism in ternary OSCs is more complex than in binary systems, primarily due to third component-induced variations in morphology and exciton dissociation. Currently, no established model fully explains V_{OC} tunability across different OSC structures.[185,186,242] While most studies correlate V_{OC} with the charge transfer state energy (E_{CT}), they often neglect the influence of acceptor components on recombination processes. Notably, non-radiative recombination-induced voltage loss (ΔV_{nr}) significantly deteriorates OSC performance. Component aggregation leads to exciton quenching, thereby enhancing non-radiative recombination. When the third component has a significant effect on the binary OSC, high compatibility between the third component and the main binary blend is required. In addition, when the third component will not have a significant effect on the morphology of the binary blend, the third component can be controlled to reduce the ΔV_{nr} by affecting the CT state of the binary blend (Fig. 12h).[243] A significant problem with the ternary strategy is the modulation of the vertical phase morphology of the blend, and proper modulation of this morphology can enhance vertical charge transport.[244] Adding a third component may induce alloy-phase formation in donor or acceptor matrices. When localized at the D/A interface, it may form an isolated phase, resulting in morphological heterogeneity and increased V_{OC} loss. Consequently, precise control over the morphology of the active layers remains a critical challenge requiring further investigation.[245] To mitigate V_{OC} losses and enhance efficiency in PO-TSCs, further development of novel materials, device architectures, and processing methods remains crucial. These advancements will significantly advance the technologies of PO-TSCs.

5. Interconnecting layers

The ICL serves as a critical functional component in 2T TSCs, which enables efficient current transport and voltage optimization by bridging subcells with different bandgaps. This necessitates detailed optimization of both the spectral management to maximize infrared transmittance to the rear cells and the current matching conditions at the maximum power point (MPP) to ensure balanced photocurrent generation. To satisfy the performance requirements, an optimal ICL must simultaneously exhibit high electrical conductivity for effective carrier collection, excellent optical transparency across the solar spectrum, robust chemical inertness, and compatibility with scalable low-cost processing methods.[36,246,247] Furthermore, advanced ICL designs should incorporate dual protective functionalities, which can protect underlying layers from environmental degradation while mitigating solution processing-induced interfacial damage during subsequent device fabrication steps.

The main structure of ICL in PeTSCs is divided into P–N, P–TCO–N, and P–metal–N. The latter two architectures are predominantly employed in current designs. The first structure introduces a significant potential barrier at the P–N junction when perovskite-generated charge carriers migrate toward the ICL. This diode-like effect substantially compromises the performance of TSCs. To address this limitation, efficient carrier transport through the ICL and rapid recombination must be achieved. Quantum tunneling facilitates direct interband electron transfer between the conduction band of the front cell's ETL and the valence band of the rear cell's HTL. Crucially, incorporating a highly conductive interlayer within the P–N junction enhances tunneling-assisted carrier recombination efficiency, which can improve the FF of devices. The ICL in TSCs presents critical challenges including parasitic absorption, solvent-induced degradation, energy level misalignment, and ion migration-induced instability. The incorporation of transparent conductive oxides or metallic components in ICLs enhances parasitic absorption due to the fundamental relationship between the absorption coefficient (α) and free electron density (n), where $\alpha \propto n$, as shown in the formula,

$$\alpha = \sigma n$$

where σ is the absorption cross-section. Enhanced doping concentration tends to amplify optical absorption in material systems. The functional characteristics of TCO films are composition-dependent, as exemplified by Sn-doped ITO. At optimal Sn doping levels, carrier density is elevated *via* substitutional incorporation, whereas excessive doping surpasses the solubility threshold, inducing lattice strain, mobility degradation, and uneven distribution. Zn, Ce, and other metals can be doped to prepare high-performance TCO films.[248] Current research strategies predominantly focus on reducing the thickness of TCO layers as the primary approach for modulating tunneling phenomena while suppressing parasitic absorption in optoelectronic devices.[249] In the P–metal–N structure, the metallic layer exhibits a higher n value relative to the TCO component, leading to a substantially elevated α. Optical transmittance is critically thickness-dependent for Ag layers, with Ag films displaying markedly inferior performance compared to their Au counterparts. This disparity has established Au as the prevailing metallic electrode in such configurations, despite persistent challenges associated with its prohibitively high material cost.

The fabrication of TSCs typically employs low-temperature solution processing, which inevitably subjects the functional layers to solvent-induced degradation. A critical challenge lies in preventing solvent penetration from the spin-coating process of rear cells into the ICL, which necessitates the incorporation of dense barrier layers. Stranks *et al.* demonstrated an innovative ICL architecture using SnO_x/C_{60}/2PACz with graphene substitution for conventional metal layers, effectively mitigating solvent infiltration issues.[250] While sputtered ITO remains the predominant choice for tunneling junctions in reported TSCs, the magnetron sputtering process often damages underlying films. This highlights the need for protective buffer layers. Tan *et al.* employed ALD to fabricate a compact SnO_2 barrier, simultaneously incorporating a metal interlayer to enhance carrier tunneling recombination. This approach yielded all-perovskite TSCs with a certified efficiency of 24.8%.[251]

Photoinduced halide migration can lead to undesirable interactions between halide ions and metallic components in the ICL, a challenge observed in both tandem and single-junction architectures. Therefore, the choice of ICL metals must prioritize not only optimal energy-level alignment but also intrinsic resistance to halide-induced chemical degradation. To mitigate carrier diffusion, introducing a dense barrier layer (such as ALD-SnO_x films) can effectively suppress undesired charge transport. Moreover, minimizing lateral conductivity in the ICL is critical to prevent the unintended lateral transport of un-recombined carriers, which may otherwise contribute to leakage pathways. However, excessive reduction in transverse conductivity, particularly in ultrathin films, can induce shunting, adversely affecting the FF and PCE of the devices.[249] Thus, optimizing the ICL requires a balanced approach to suppress leakage channels while maintaining sufficient conductivity for efficient charge collection.

6. Outlook and prospects for solution-processed PeTSCs

6.1 Further improvement in PCE (especially for flexible PeTSCs)

The continuous improvement of PeTSC efficiency remains a key research priority, with material optimization and interface engineering playing crucial roles. Recent studies highlight the importance of developing advanced active layer materials, implementing additive strategies, and precisely controlling interfacial properties to enhance the performance of devices. Tables 1 and 2 summarize key developments in PeTSCs, covering device structures, key improvements, and photovoltaic parameters (V_{OC}, J_{SC}, FF, and PCE). In WBG PSCs, performance losses are primarily attributed to interfacial issues, particularly at the bottom interface, which significantly affects perovskite crystallization. However, further understanding the bottom interface presents greater challenges than the top interface, and its fundamental mechanisms remain incompletely resolved. Addressing these challenges requires simultaneous development of crystallization-promoting additives and tailored interface layers that guide optimal perovskite growth. The ICL represents another important component, where uncertainties regarding charge carrier recombination pathways limit systematic optimization. Among available options, transparent conducting oxide-based ICLs show particular promise for industrial-scale manufacturing due to their excellent conductivity, transparency, and process compatibility. Mitigating sputtering-induced damage during deposition remains a significant challenge that requires innovative protective interlayer solutions.

In addition to the high efficiency, PeTSCs have also demonstrated broad prospects for application in flexible electronics. Notably, the perovskite thin films undergo microstructural evolution under mechanical strain, which indicates surface wrinkling and interfacial delamination that affect the PCE and operational stability of devices.[101,252,253] The inherent brittleness makes them prone to crack formation under stress. While Young's modulus typically reflects material rigidity, brittle perovskite films may fracture even at low modulus values, necessitating both low stiffness and enhanced ductility for flexible applications.[254] Furthermore, weak interlayer adhesion promotes interface failure during repeated bending. The thermal expansion coefficient mismatch between perovskite films and flexible substrates generates strain-induced performance degradation, where tensile stress promotes crack propagation while compressive stress induces interfacial delamination. Addressing the challenges requires simultaneous optimization of mechanical properties and interfacial engineering.[253–256] Huang *et al.* incorporated liquid crystal elastomer interlayers into flexible devices, toughening charge-transfer channels through mesocrystalline arrays. Photopolymerization of the diacrylate monomer and dithiol-terminated oligomer stabilized molecular alignment. This optimization improved charge collection and suppressed interfacial recombination, achieving efficiencies of 23.26% for rigid devices and 22.10% for their flexible counterparts.[1]

The high absorption coefficient of perovskite materials enables ultra-thin films (<1 μm), but the thickness exacerbates stress concentration during substrate bending, which accelerates strain-induced structural degradation. Such mechanical instability critically compromises interfacial integrity during dynamic operation, demanding innovative approaches for robust flexible architectures.[257,258] Furthermore, weak interlayer

Table 1 Summary of perovskite/organic TSCs

Year	Device structure	V_{OC} (V)	J_{SC} (mA cm^{-2})	FF (%)	PCE (%)	Ref.
2019	ITO/SnO_2/$CsPbI_2Br$/PTAA/MoO_3/Au/ZnO/PTB7-Th:CO_i8DFIC:$PC_{71}BM$/MoO_3/Ag	1.710	11.98	73.40	15.04	29
2020	ITO/NiO_x/$FA_{0.8}MA_{0.02}Cs_{0.18}PbI_{1.8}Br_{1.2}$/C60/BCP/Ag nanoparticle/MoO_x/PBDBT-2F:Y6:$PC_{71}BM$/TPBi/Ag	1.902	13.05	83.10	20.60	36
2022	ITO/2PACz/$FA_{0.6}MA_{0.4}PbI_{1.8}Br_{1.2}$/$C_{60}$/BCP/Ag/$MoO_x$/PTB7-Th:BTPV-4Cl-eC9/PDINN/Ag	1.880	15.70	74.6	22.00	229
2022	ITO/MeO-2PACz/$FA_{0.8}Cs_{0.2}PbI_{1.8}Br_{1.2}$/C60/ALD-$SnO_2$/Au/PEDOT:PSS/PM6:Y6/PFN-Br2/Ag	2.072	13.95	77.29	22.29	234
2022	ITO/NiO_x/BPA/$Cs_{0.25}FA_{0.75}PbI_{1.8}Br_{1.2}$/$C_{60}$/BCP/CRL/$MoO_x$/PM6:Y6:$PC_{71}BM$/PNDIT-F3N/Ag	2.065	14.87	74.70	22.94	31
2023	ITO/NiO_x/2PACz/$Cs_{0.25}FA_{0.75}PbI_{1.8}Br_{1.2}$/PEAI/$PC_{61}BM$/BCP/Ag/Au/$MoO_x$/PM6:Y6:$PC_{61}BM$/PFN-Br/Ag	2.067	14.27	78.84	23.26	235
2024	ITO/4PADCB/$FAMACsPbI_{1.5}Br_{1.5}$/$PC_{60}BM$/C_{60}/SnO_x/Au/PEDOT:PSS/D18:L8-BO:BTP-eC9-4F/PDINN/Ag	2.200	13.80	80.60	24.50	226
2024	ITO/NiO_x/Me-2PACz/perovskite/C_{60}/BCP/Au/MoO_x/Me-4PACz/PM6:Y6:L8-BO/C_{60}/BCP/Ag	2.126	14.38	83.62	25.56	232
2024	ITO/NiOx/2PACz/$FA_{0.8}Cs_{0.2}PbI_{1.6}Br_{1.4}$/PEAI/$C_{60}$/BCP/Ag/$MoO_3$/2PACz/D18:Cl:N3:$PC_{61}BM$/$C_{60}$/BCP/Ag	2.120	14.68	82.97	25.82	62
2025	ITO/Br-Ph-4PACz/$Cs_{0.25}FA_{0.75}PbI_{1.8}Br_{1.2}$/$C_{60}$/$SnO_x$/ITO/$MoO_x$/PM6:P2EH-2V/PDINN/Ag	2.140	15.15	82.4	26.70	260

adhesion and bending-induced delamination at functional interfaces significantly degrade the performance of devices. At present, transparent electrode optimization remains another key challenge, as conventional ITO electrodes exhibit poor mechanical stability under repeated bending.

Compared with the rigid PeTSC, the PCE of a flexible PeTSC is relatively lower. This is primarily due to mechanical degradation during bending. Grain boundary cracks and interfacial delamination necessitate improved film flexibility and self-healing properties to mitigate defect formation.[251,259] While a lower Young's modulus typically correlates with better bending durability, the fundamental mechanical trade-offs between flexibility and the performance of devices remain insufficiently understood.

6.2 Scalability and stability

Large-scale production of the PeTSC remains a critical hurdle for commercialization. Techniques such as blade-coating, roll-to-roll processing, and inject-printing indicate promise for scalable fabrication, but their efficiency in mass production still requires optimization.[262–264] Notably, the volume of technology offers advantages in reducing processing steps and costs, yet achieving high-throughput uniformity presents ongoing challenges. Additionally, industrial adoption necessitates the development of environmentally benign solvents. Conventional solvents like DMF:DMSO and chlorobenzene raise toxicity concerns and yield unstable perovskite films, further complicating large-scale manufacturing. The pursuit of green alternatives that simultaneously enhance device performance and stability remains a key research priority for sustainable PSC commercialization.[265–267]

The commercialization of PeTSCs necessitates overcoming critical stability limitations. Under operating conditions, the primary degradation mechanisms of perovskite sub-cells include ion migration, photothermal-induced oxidation, and stress-induced damage. Specifically, the migration of ions (*e.g.*, MA^+, Pb^{2+}, and I^-) disrupts local chemical stoichiometry, leading to perovskite decomposition. Furthermore, ion migration induces hysteresis effects, lattice distortion, and the formation of non-radiative recombination centers.[268–270] For instance, in wide-bandgap perovskites, phase separation is the result of ion migration. Chen *et al.* employed triphenyl phosphate (Tri-PyPA) to modulate the Br/I competitive crystallization and compositional distribution in perovskite films. Tri-PyPA interacts with the formamidinium (FA^+) cations through its π–

Table 2 Summary of all-perovskite TSCs

Year	Device structure	V_{OC} (V)	J_{SC} (mA cm^{-2})	FF (%)	PCE (%)	Ref.
2019	ITO/PTAA/$Cs_{0.05}MA_{0.05}FA_{0.9}PbI_{2.85}Br_{0.15}$/$C_{60}$/$SnO_2$/Au/PEDOT:PSS/$FA_{0.7}MA_{0.3}Pb_{0.5}Sn_{0.5}I_3$/$C_{60}$/BCP/Cu	1.965	15.60	81.00	24.80	251
2020	ITO/NiO/VNPB/$FA_{0.8}Cs_{0.2}PbI_{1.8}Br_{1.2}$/$C_{60}$/$SnO_2$/Au/PEDOT-PSS/$FA_{0.7}MA_{0.3}Pb_{0.5}Sn_{0.5}I_3$/$C_{60}$/$SnO_2$/Cu	2.013	16.00	79.80	25.60	30
2022	ITO/NiO/VNPB/$FA_{0.8}Cs_{0.2}PbI_{1.86}Br_{1.14}$/$SnO_2$/Au/PEDOT:PSS/$FA_{0.7}MA_{0.3}Pb_{0.5}Sn_{0.5}I_3$/$C_{60}$/BCP/Cu	2.048	16.54	77.90	26.40	261
2023	ITO/2PACz/$FA_{0.6}MA_{0.4}PbI_{1.8}Br_{1.2}$/$C_{60}$/BCP/Au/PEDOT:PSS/$FA_{0.7}MA_{0.3}Pb_{0.5}Sn_{0.5}I_3$/$C_{60}$/BCP/Cu	2.110	16.06	82.20	27.34	34
2024	ITO/NiO_x/Me-4PACz/$FA_{0.8}Cs_{0.2}PbI_{1.8}Br_{1.2}$/$C_{60}$/$SnO_x$/Au/PEDOT:PSS/$FA_{0.7}MA_{0.3}Pb_{0.5}Sn_{0.5}I_3$/$C_{60}$/BCP/Cu	2.130	16.27	78.94	27.35	154
2024	TCO/NiO/Me-2PACz/$FA_{0.8}Cs_{0.2}PbI_{1.89}Br_{1.11}$/$C_{60}$/$SnO_2$/Au/PEDOT:PSS/$Cs_{0.05}FA_{0.7}MA_{0.25}Sn_{0.5}Pb_{0.5}I_3$/$C_{60}$/$SnO_2$/Ag	2.180	15.71	79.90	27.41	149
2024	ITO/Me-4PACz/Al_2O_3/$FA_{0.8}Cs_{0.2}PbI_{1.8}Br_{1.2}$/$PDAI_2$/$C_{60}$/$SnO_2$/Au/PEDOT:PSS/$Al_2O_3$/$FA_{0.7}MA_{0.3}Pb_{0.7}Sn_{0.3}I_3$/BDA-$EDAI_2$/$C_{60}$/BCP/Ag	2.123	16.00	83.88	28.49	167
2025	ITO/NiOx/SAM/$FA_{0.8}Cs_{0.2}PbI_{1.8}Br_{1.2}$/$C_{60}$/$SnO_2$/Au/PEDOT:PSS/$FA_{0.7}MA_{0.3}Pb_{0.5}Sn_{0.5}I_3$/$C_{60}$/BCP/Cu	2.151	16.51	82.00	29.10	35

π conjugated system, effectively immobilizing them. This interaction significantly suppresses non-radiative recombination and increases the energy barrier for ion migration, thereby greatly enhancing device stability. As a result, the unencapsulated device retained 95% of its initial efficiency after 1100 hours of continuous light soaking.[271] Permanent suppression of phase segregation through tailored additives could substantially enhance the long-term stability of devices. Grain boundary defects generated during perovskite crystallization contribute to carrier recombination and V_{OC} loss, while interfacial reactions such as photocatalytic oxidation at the HTL/perovskite interface further degrade performance. Effective mitigation approaches focus on advanced encapsulation technologies utilizing cross-linked polymers or high-performance barrier materials to prevent moisture and oxygen penetration. Currently, ultraviolet-curable epoxy, butyl rubber, and silicone adhesives are widely employed as encapsulation materials in perovskite solar cells. However, high-energy ultraviolet irradiation can accelerate the decomposition of the perovskite layer and degrade device performance.[237] The photopolymerization process is highly exothermic, and releases significant amounts of heat inducing thermal stress within the perovskite film. This stress can lead to cracking or interfacial delamination due to mismatched thermal expansion coefficients among adjacent layers.[272] Equally important is the development of low-temperature compatible packaging solutions to minimize thermal stress effects in tandem device architectures. The combined strategies address the fundamental stability challenges while preserving the performance of devices. The development of robust encapsulation systems alongside optimized interfacial engineering represents a promising pathway toward achieving commercially viable perovskite photovoltaics.

Furthermore, recent studies have improved the stability of tandem devices using self-packaging techniques. For example, in all-perovskite TSCs, self-encapsulation is achieved by depositing NBG PSCs before WBG PSCs. Similarly, the organic rear cell functions as a self-packaging layer, which can provide additional protection against moisture and oxygen, thereby enhancing the stability of PO-TSCs.

6.3 Commercialization and application

In PeTSCs with 4T architecture, configurations using c-Si or CIGS as the rear cell have shown promising commercial scalability. However, the commercial development of Si and CIGS-based technologies is constrained by their inherent processing limitations.[273] Additionally, the 4T structure requires complex interconnection strategies and additional circuitry for grid integration, which generates significant economic challenges for large-scale photovoltaic deployment.

In practice, sunlight enters the device through the glass substrate. The light reflection at the glass interface is unavoidable, and the incorporation of an anti-reflection layer can mitigate optical losses and enhance light absorption. However, the PCE of PO-TSCs exhibits significant angular dependence, deteriorating under oblique light incidence. This is primarily attributed to increased optical losses and non-radiative recombination in PSCs under wide-angle illumination. Currently, most studies focus on normal incidence conditions, with a limited investigation into angular-dependent performance. To enable the commercial viability of PO-TSCs, it is imperative to develop effective approaches that minimize both wide-angle optical losses and non-radiative recombination.

By contrast, PeTSCs based on a 2T structure demonstrate superior PCE alongside a relatively simple device interconnect. Both all-perovskite TSCs and PO-TSCs exhibit advantageous attributes including lightweight design, a low-cost fabrication process, low-temperature processing compatibility, and mechanical flexibility, which make them attractive for next-generation photovoltaics. The all-perovskite TSCs have achieved certified PCE exceeding 24.4% in flexible configurations, but their operational lifetime remains constrained by inherent material instability. In comparison, PO-TSCs exhibit superior environmental stability nearing industrial requirements, alongside rapid efficiency gains in recent years. These divergent characteristics highlight the necessity for targeted material stabilization strategies and advanced interfacial engineering to bridge the gap between laboratory breakthroughs and commercial viability.[274,275]

PO-TSCs, through the use of a rich variety of materials and processing technology of low-temperature high flux, can overcome these problems; at present, the efficiency of PO-TSCs is less than that of other PeTSCs, and further optimization is needed. PO-TSCs have the characteristics of flexibility, self-packaging, and light weight, which can be applied in many aspects (*e.g.* agriculture photoelectric, building photovoltaics, transportation, indoor photovoltaics, and other aspects). The flexible characteristics of PO-TSCs make them suitable for curved or special-shaped building surfaces, and they can be integrated into the exterior walls, windows or roofs of buildings, directly replacing traditional building materials, and realizing the integration of solar power generation and architectural design and can also be used for energy supply for mobile power sources, outdoor charging devices, smart clothing, or flexible electronic devices such as smart watches, health monitoring devices, and display screens. Their thin and flexible characteristics are suitable for fitting the surface of portable electronics or equipment. The future PO-TSCs will have lightweight characteristics, which are suitable for unmanned aerial vehicle (UAV) energy systems to extend the flight time. Perovskite/organic tandem cells have the potential to transform the fields of construction, transportation, consumer electronics and distributed energy, and their technological breakthroughs will promote the development of the photovoltaic industry in the direction of efficiency, light weight, and diversification.

Author contributions

J. L. and L. L. prepared the manuscript with contributions from all the co-authors. All authors revised the manuscript.

Conflicts of interest

The authors declare no conflict of interest.

Note added after first publication

This article replaces the version published on 8th September 2025, where a footnote from the author list had been missed, this has now been resolved.

Data availability

No primary research results, software or code have been included and no new data were generated or analysed as part of this review.

Acknowledgements

This work was supported by the National Key R&D Program of China: Strategic International Innovation Cooperation (2024YFE0209400), the National Natural Science Foundation of China (NSFC) (52473261 and 52333006), the Young Elite Scientists Sponsorship Program by CAST (YESS20230261), the "Double Thousand Plan" Science and Technology Innovation High-end Talent Project of Jiangxi Province (jxsq2023101111), and the Natural Science Foundation of Jiangxi Province (20242BAB23031, 20231ZDH04036, and 20232BAB214028).

References

1 Z. Huang, L. Li, T. Wu, T. Xue, W. Sun, Q. Pan, H. Wang, H. Xie, J. Chi, T. Han, X. Hu, M. Su, Y. Chen and Y. Song, Wearable perovskite solar cells by aligned liquid crystal elastomers, *Nat. Commun.*, 2023, **14**, 1204.

2 M. Kaltenbrunner, G. Adam, E. D. Głowacki, M. Drack, R. Schwödiauer, L. Leonat, D. H. Apaydin, H. Groiss, M. C. Scharber, M. S. White, N. S. Sariciftci and S. Bauer, Flexible high power-per-weight perovskite solar cells with chromium oxide–metal contacts for improved stability in air, *Nat. Mater.*, 2015, **14**, 1032–1039.

3 X. Meng, Z. Cai, Y. Zhang, X. Hu, Z. Xing, Z. Huang, Z. Huang, Y. Cui, T. Hu, M. Su, X. Liao, L. Zhang, F. Wang, Y. Song and Y. Chen, Bio-inspired vertebral design for scalable and flexible perovskite solar cells, *Nat. Commun.*, 2020, **11**, 3016.

4 M. Batmunkh, Y. L. Zhong and H. Zhao, Recent advances in perovskite-based building-integrated photovoltaics, *Adv. Mater.*, 2020, **32**, 2000631.

5 I. C. Smith, E. T. Hoke, D. Solis-Ibarra, M. D. McGehee and H. I. Karunadasa, A layered hybrid perovskite solar-cell absorber with enhanced moisture stability, *Angew. Chem., Int. Ed.*, 2014, **53**, 11232–11235.

6 G. E. Eperon, G. M. Paternò, R. J. Sutton, A. Zampetti, A. A. Haghighirad, F. Cacialli and H. J. Snaith, Inorganic caesium lead iodide perovskite solar cells, *Adv. Mater.*, 2015, **3**, 19688–19695.

7 D. Weber, CH3NH3PbX3, ein Pb (II)-system mit kubischer perowskitstruktur/CH3NH3PbX3, a Pb (II)-system with cubic perovskite structure, *Z. Naturforsch.*, 1978, **33**, 1443–1445.

8 W. Yin, T. Shi and Y. Yan, Unique properties of halide perovskites as possible origins of the superior solar cell performance, *Adv. Mater.*, 2014, **26**, 4653–4658.

9 A. Kojima, K. Teshima, Y. Shirai and T. Miyasaka, Organometal halide perovskites as visible-light sensitizers for photovoltaic cells, *J. Am. Chem. Soc.*, 2009, **131**, 6050–6051.

10 M. A. Green, E. D. Dunlop, M. Yoshita, N. Kopidakis, K. Bothe, G. Siefer, X. Hao and J. Y. Jiang, Solar Cell Efficiency Tables (Version 66), *Prog. Photovoltaics Res. Appl.*, 2025, **33**, 795–810.

11 S. Wu, M. Liu and A. K. Y. Jen, Prospects and challenges for perovskite-organic tandem solar cells, *Joule*, 2023, **7**, 484–502.

12 M. Yao, S. Cong, S. Arab, N. Huang, M. L. Povinelli, S. B. Cronin, P. D. Dapkus and C. Zhou, Tandem solar cells using GaAs nanowires on Si: design, fabrication, and observation of voltage addition, *Nano Lett.*, 2015, **15**, 7217–7224.

13 C. Luo, H. Gu, B. Zhang, S. M. Park, M. Wei and Y. Hou, Perovskite Tandems: the Next Big Leap in Photovoltaic Technology, *Adv. Mater.*, 2025, e08331.

14 Y. An, N. Zhang, Q. Liu, W. Jiang, G. Du, D. Chen, M. Liu, X. Huang, T. Lei, Q. Qiu, F. R. Lin, X. C. Zeng, A. K. Y. Jen and H.-L. Yip, Balancing carrier transport in interconnection layer for efficient perovskite/organic tandem solar cells, *Nat. Commun.*, 2025, **16**, 2759.

15 G. E. Eperon, M. T. Hörantner and H. J. Snaith, Metal halide perovskite tandem and multiple-junction photovoltaics, *Nat. Rev. Chem.*, 2017, **1**, 0095.

16 J. Werner, G. Dubuis, A. Walter, P. Löper, S.-J. Moon, S. Nicolay, M. Morales-Masis, S. De Wolf, B. Niesen and C. Ballif, Sputtered rear electrode with broadband transparency for perovskite solar cells, *Sol. Energy Mater. Sol. Cells*, 2015, **141**, 407–413.

17 C. D. Bailie, M. G. Christoforo, J. P. Mailoa, A. R. Bowring, E. L. Unger, W. H. Nguyen, J. Burschka, N. Pellet, J. Z. Lee, M. Grätzel, R. Noufi, T. Buonassisi, A. Salleo and M. D. McGehee, Semi-transparent perovskite solar cells for tandems with silicon and CIGS, *Energy Environ. Sci.*, 2015, **8**, 956–963.

18 F. Fu, T. Feurer, T. Jäger, E. Avancini, B. Bissig, S. Yoon, S. Buecheler and A. N. Tiwari, Low-temperature-processed efficient semi-transparent planar perovskite solar cells for bifacial and tandem applications, *Nat. Commun.*, 2015, **6**, 8932.

19 L. Esaki, New phenomenon in narrow germanium p–n junctions, *Phys. Rev.*, 1958, **109**, 603.

20 M. Bonnet-Eymard, M. Boccard, G. Bugnon, F. Sculati-Meillaud, M. Despeisse and C. Ballif, Optimized short-circuit current mismatch in multi-junction solar cells, *Sol. Energy Mater. Sol. Cells*, 2013, **117**, 120–125.

21 J. Werner, C.-H. Weng, A. Walter, L. Fesquet, J. P. Seif, S. De Wolf, B. Niesen and C. Ballif, Efficient monolithic perovskite/silicon tandem solar cell with cell area> 1 cm2, *J. Phys. Chem. Lett.*, 2016, **7**, 161–166.

22 H. Fujiwara, *Hybrid perovskite solar cells: Characteristics and Operation*, John Wiley & Sons, 2022.

23 Best Research-Cell Efficiency Chart(03/2025), **https://www.nrel.gov/pv/cell-efficiency.html**.

24 M. Zhang and Z. Lin, Efficient interconnecting layers in monolithic all-perovskite tandem solar cells, *Energy Environ. Sci.*, 2022, **15**, 3152–3170.

25 E. T. Hoke, D. J. Slotcavage, E. R. Dohner, A. R. Bowring, H. I. Karunadasa and M. D. McGehee, Reversible photo-induced trap formation in mixed-halide hybrid perovskites for photovoltaics, *Chem. Sci.*, 2015, **6**, 613–617.

26 G. Yang, Z. Ni, Z. J. Yu, B. W. Larson, Z. Yu, B. Chen, A. Alasfour, X. Xiao, J. M. Luther, Z. C. Holman and J. Huang, Defect engineering in wide-bandgap perovskites for efficient perovskite–silicon tandem solar cells, *Nat. Photonics*, 2022, **16**, 588–594.

27 L. Xu, X. Feng, W. Jia, W. Lv, A. Mei, Y. Zhou, Q. Zhang, R. Chen and W. Huang, Recent advances and challenges of inverted lead-free tin-based perovskite solar cells, *Energy Environ. Sci.*, 2021, **14**, 4292–4317.

28 X. Jiang, S. Qin, L. Meng, G. He, J. Zhang, Y. Wang, Y. Zhu, T. Zou, Y. Gong, Z. Chen, G. Sun, M. Liu, X. Li, F. Lang and Y. Li, Isomeric diammonium passivation for perovskite–organic tandem solar cells, *Nature*, 2024, **635**, 860–866.

29 Q. Zeng, L. Liu, Z. Xiao, F. Liu, Y. Hua, Y. Yuan and L. Ding, A two-terminal all-inorganic perovskite/organic tandem solar cell, *Sci. Bull.*, 2019, **64**, 885–887.

30 K. Xiao, R. Lin, Q. Han, Y. Hou, Z. Qin, H. T. Nguyen, J. Wen, M. Wei, V. Yeddu, M. I. Saidaminov, Y. Gao, X. Luo, Y. Wang, H. Gao, C. Zhang, J. Xu, J. Zhu, E. H. Sargent and H. Tan, All-perovskite tandem solar cells with 24.2% certified efficiency and area over 1 cm2 using surface-anchoring zwitterionic antioxidant, *Nat. Energy*, 2020, **5**, 870–880.

31 W. Chen, Y. Zhu, J. Xiu, G. Chen, H. Liang, S. Liu, H. Xue, E. Birgersson, J. W. Ho, X. Qin, J. Lin, R. Ma, T. Liu, Y. He, A. M.-C. Ng, X. Guo, Z. He, H. Yan, A. B. Djurišić and Y. Hou, Monolithic perovskite/organic tandem solar cells with 23.6% efficiency enabled by reduced voltage losses and optimized interconnecting layer, *Nat. Energy*, 2022, **7**, 229–237.

32 L. Li, Y. Wang, X. Wang, R. Lin, X. Luo, Z. Liu, K. Zhou, S. Xiong, Q. Bao, G. Chen, Y. Tian, Y. Deng, K. Xiao, J. Wu, M. I. Saidaminov, H. Lin, C.-Q. Ma, Z. Zhao, Y. Wu, L. Zhang and H. Tan, Flexible all-perovskite tandem solar cells approaching 25% efficiency with molecule-bridged hole-selective contact, *Nat. Energy*, 2022, **7**, 708–717.

33 K. O. Brinkmann, T. Becker, F. Zimmermann, C. Kreusel, T. Gahlmann, M. Theisen, T. Haeger, S. Olthof,

C. Tückmantel, M. Günster, T. Maschwitz, F. Göbelsmann, C. Koch, D. Hertel, P. Caprioglio, F. Peña-Camargo, L. Perdigón-Toro, A. Al-Ashouri, L. Merten, A. Hinderhofer, L. Gomell, S. Zhang, F. Schreiber, S. Albrecht, K. Meerholz, D. Neher, M. Stolterfoht and T. Riedl, Perovskite–organic tandem solar cells with indium oxide interconnect, *Nature*, 2022, **604**, 280–286.

34 S. Zhou, S. Fu, C. Wang, W. Meng, J. Zhou, Y. Zou, Q. Lin, L. Huang, W. Zhang, G. Zeng, D. Pu, H. Guan, C. Wang, K. Dong, H. Cui, S. Wang, T. Wang, G. Fang and W. Ke, Aspartate all-in-one doping strategy enables efficient all-perovskite tandems, *Nature*, 2023, **624**, 69–73.

35 Z. Liu, R. Lin, M. Wei, M. Yin, P. Wu, M. Li, L. Li, Y. Wang, G. Chen, V. Carnevali, L. Agosta, V. Slama, N. Lempesis, Z. Wang, M. Wang, Y. Deng, H. Luo, H. Gao, U. Rothlisberger, S. M. Zakeeruddin, X. Luo, Y. Liu, M. Grätzel and H. Tan, All-perovskite tandem solar cells achieving >29% efficiency with improved (100) orientation in wide-bandgap perovskites, *Nat. Mater.*, 2025, **24**, 252–259.

36 X. Chen, Z. Jia, Z. Chen, T. Jiang, L. Bai, F. Tao, J. Chen, X. Chen, T. Liu, X. Xu, C. Yang, W. Shen, W. E. I. Sha, H. Zhu and Y. Yang, Efficient and Reproducible Monolithic Perovskite/Organic Tandem Solar Cells with Low-Loss Interconnecting Layers, *Joule*, 2020, **4**, 1594–1606.

37 A. Filippetti and A. Mattoni, Hybrid perovskites for photovoltaics: Insights from first principles, *Phys. Rev. B*, 2014, **89**, 125203.

38 H. Sun, S. Liu, X. Liu, Y. Gao, J. Wang, C. Shi, H. Raza, Z. Sun, Y. Pan, Y. Cai, S. Zhang, D. Sun, W. Chen and Z. Liu, Suppressed Phase Segregation with Small A-Site and Large X-Site Incorporation for Photostable Wide-Bandgap Perovskite Solar Cells, *Small Methods*, 2024, **8**, 2400067.

39 D. P. McMeekin, G. Sadoughi, W. Rehman, G. E. Eperon, M. Saliba, M. T. Hörantner, A. Haghighirad, N. Sakai, L. Korte, B. Rech, M. B. Johnston, L. M. Herz and H. J. Snaith, A mixed-cation lead mixed-halide perovskite absorber for tandem solar cells, *Science*, 2016, **351**, 151–155.

40 Z. Li, M. Yang, J.-S. Park, S.-H. Wei, J. J. Berry and K. Zhu, Stabilizing perovskite structures by tuning tolerance factor: formation of formamidinium and cesium lead iodide solid-state alloys, *Chem. Mat.*, 2016, **28**, 284–292.

41 W. Travis, E. Glover, H. Bronstein, D. Scanlon and R. Palgrave, On the application of the tolerance factor to inorganic and hybrid halide perovskites: a revised system, *Chem. Sci.*, 2016, **7**, 4548–4556.

42 S. Fu, S. Zhou, W. Meng, G. Li, K. Dong, D. Pu, J. Zhou, C. Wang, H. Guan, W. Shao, L. Huang, Z. Su, C. Wang, G. Chen, P. Jia, J. Wang, Z. Xu, X. Gao, H. Cong, T. Wang, C. Xiao, G. Fang and W. Ke, Piracetam shapes wide-bandgap perovskite crystals for scalable perovskite tandems, *Nat. Nanotechnol.*, 2025, 1–8.

43 Y. Tong, A. Najar, L. Wang, L. Liu, M. Du, J. Yang, J. Li, K. Wang and S. Liu, Wide-bandgap organic–inorganic lead halide perovskite solar cells, *Adv. Sci.*, 2022, **9**, 2105085.

44 Z. Fang, N. Yan and S. Liu, Modulating preferred crystal orientation for efficient and stable perovskite solar cells—From progress to perspectives, *InfoMat*, 2022, **4**, e12369.

45 L. Liu, D. Zheng, M. Du, J. Liu, J. Liu, Z. Li, X. Dong, C. Xu, Y. He, K. Wang and S. Liu, Advancements and Challenges in Wide-Bandgap Perovskite Solar Cells: From Single Junction to Tandem Solar Cells, *Sol. RRL*, 2024, **8**, 2400359.

46 K. L. Svane, A. C. Forse, C. P. Grey, G. Kieslich, A. K. Cheetham, A. Walsh and K. T. Butler, How strong is the hydrogen bond in hybrid perovskites?, *J. Phys. Chem. Lett.*, 2017, **8**, 6154–6159.

47 N. J. Jeon, J. H. Noh, W. S. Yang, Y. C. Kim, S. Ryu, J. Seo and S. I. Seok, Compositional engineering of perovskite materials for high-performance solar cells, *Nature*, 2015, **517**, 476–480.

48 X. Li, Y. Li, Y. Feng, J. Qi, J. Shen, G. Shi, S. Yang, M. Yuan and T. He, Strain Regulation of Mixed-Halide Perovskites Enables High-Performance Wide-Bandgap Photovoltaics, *Adv. Mater.*, 2024, **36**, 2401103.

49 T. S. Dongxu Lin, H. Xie, F. Wan, X. Ren, K. Liu, Z. Yuan, L. Ke, Y. Lin, Y. Gao, X. Xu, W. Xie, P. Liu and Y. Yuan, Ion Migration Accelerated Reaction between Oxygen and Metal Halide Perovskites in Light and Its Suppression by Cesium Incorporation, *Adv. Energy Mater.*, 2021, **11**, 2002552.

50 D. J. Kubicki, D. Prochowicz, A. Hofstetter, M. Saski, P. Yadav, D. Bi, N. Pellet, J. Lewinski, S. M. Zakeeruddin, M. Gratzel and L. Emsley, Formation of stable mixed guanidinium–methylammonium phases with exceptionally long carrier lifetimes for high-efficiency lead iodide-based perovskite photovoltaics, *J. Am. Chem. Soc.*, 2018, **140**, 3345–3351.

51 B. Walker, G. H. Kim and J. Y. Kim, Pseudohalides in lead-based perovskite semiconductors, *Adv. Mater.*, 2019, **31**, 1807029.

52 W. Ke, C. Xiao, C. Wang, B. Saparov, H.-S. Duan, D. Zhao, Z. Xiao, P. Schulz, S. P. Harvey, W. Liao, W. Meng, Y. Yu, A. J. Cimaroli, C.-S. Jiang, K. Zhu, M. Al-Jassim, G. Fang, D. B. Mitzi and Y. Yan, Employing lead thiocyanate additive to reduce the hysteresis and boost the fill factor of planar perovskite solar cells, *Adv. Mater.*, 2016, **28**, 5214.

53 X. Zhou, X. Li, B. Shi, P. Wang, X. Du, Y. Zhao and X. Zhang, Regulating Crystallization for Pure-Iodide 1.68 eV Bandgap Perovskite Solar Cells with a Fill Factor over 86%, *ACS Nano*, 2025, **19**, 11187–11196.

54 X. Shen, B. M. Gallant, P. Holzhey, J. A. Smith, K. A. Elmestekawy, Z. Yuan, P. Rathnayake, S. Bernardi, A. Dasgupta, E. Kasparavicius, T. Malinauskas, P. Caprioglio, O. Shargaieva, Y.-H. Lin, M. M. McCarthy, E. Unger, V. Getautis, A. Widmer-Cooper, L. M. Herz and H. J. Snaith, Chloride-based additive engineering for efficient and stable wide-bandgap perovskite solar cells, *Adv. Mater.*, 2023, **35**, 2211742.

55 S. Kim, J.-H. Kim, P. Ramming, Y. Zhong, K. Schötz, S. J. Kwon, S. Huettner, F. Panzer and N.-G. Park, How antisolvent miscibility affects perovskite film wrinkling and photovoltaic properties, *Nat. Commun.*, 2021, **12**, 1554.

56 Z. Li, X. Li, X. Chen, X. Cui, C. Guo, X. Feng, D. Ren, Y. Mo, M. Yang, H. Huang, R. Jia, X. Liu, L. Han, S. Dai and M. Cai, In situ epitaxial growth of blocking structure in mixed-halide wide-band-gap perovskites for efficient photovoltaics, *Joule*, 2023, **7**, 1363–1381.

57 M. C. Brennan, A. Ruth, P. V. Kamat and M. Kuno, Photoinduced anion segregation in mixed halide perovskites, *Trends Chem.*, 2020, **2**, 282–301.

58 L. A. Muscarella and B. Ehrler, The influence of strain on phase stability in mixed-halide perovskites, *Joule*, 2022, **6**, 2016–2031.

59 J. Diekmann, F. Peña-Camargo, N. Tokmoldin, J. Thiesbrummel, J. Warby, E. Gutierrez-Partida, S. Shah, D. Neher and M. Stolterfoht, Determination of mobile ion densities in halide perovskites *via* low-frequency capacitance and charge extraction techniques, *J. Phys. Chem. Lett.*, 2023, **14**, 4200–4210.

60 J. Haruyama, K. Sodeyama, L. Han and Y. Tateyama, First-principles study of ion diffusion in perovskite solar cell sensitizers, *J. Am. Chem. Soc.*, 2015, **137**, 10048–10051.

61 H. Zhang, Y. Luo, T. A. Dela Peña, R. Ma, H. Yan, M. Li, M. Suryawanshi, J. Wu and A. Uddin, Latest Strategies Promoting Stable and Efficient Perovskite, Organic, and Perovskite-Organic Tandem Solar Cells, *Adv. Mater. Interfaces*, 2025, **12**, 2500204.

62 Z. Zhang, W. Chen, X. Jiang, J. Cao, H. Yang, H. Chen, F. Yang, Y. Shen, H. Yang, Q. Cheng, X. Chen, X. Tang, S. Kang, X.-m. Ou, C. J. Brabec, Y. Li and Y. Li, Suppression of phase segregation in wide-bandgap perovskites with thiocyanate ions for perovskite/organic tandems with 25.06% efficiency, *Nat. Energy*, 2024, **9**, 592–601.

63 Z. Shen, Q. Han, X. Luo, Y. Shen, Y. Wang, Y. Yuan, Y. Zhang, Y. Yang and L. Han, Efficient and stable perovskite solar cells with regulated depletion region, *Nat. Photonics*, 2024, **18**, 450–457.

64 L. A. Muscarella, E. M. Hutter, F. Wittmann, Y. W. Woo, Y.-K. Jung, L. McGovern, J. Versluis, A. Walsh, H. J. Bakker and B. Ehrler, Lattice compression increases the activation barrier for phase segregation in mixed-halide perovskites, *ACS Energy Lett.*, 2020, **5**, 3152–3158.

65 H. Xue, G. Brocks and S. Tao, Intrinsic defects in primary halide perovskites: A first-principles study of the thermodynamic trends, *Phys. Rev. Mater.*, 2022, **6**, 055402.

66 N. Li, Y. Jia, Y. Guo and N. Zhao, Ion migration in perovskite light-emitting diodes: mechanism, characterizations, and material and device engineering, *Adv. Mater.*, 2022, **34**, 2108102.

67 D. Luo, R. Su, W. Zhang, Q. Gong and R. Zhu, Minimizing non-radiative recombination losses in perovskite solar cells, *Nat. Rev. Mater.*, 2020, **5**, 44–60.

68 H. Cho, S.-H. Jeong, M.-H. Park, Y.-H. Kim, C. Wolf, C.-L. Lee, J. H. Heo, A. Sadhanala, N. Myoung, S. Yoo, S. H. Im, R. H. Friend and T.-W. Lee, Overcoming the electroluminescence efficiency limitations of perovskite light-emitting diodes, *Science*, 2015, **350**, 1222–1225.

69 J. Luo, X. Wang, S. Li, J. Liu, Y. Guo, G. Niu, L. Yao, Y. Fu, L. Gao, Q. Dong, C. Zhao, M. Leng, F. Ma, W. Liang, L. Wang, S. Jin, J. Han, L. Zhang, J. Etheridge, J. Wang, Y. Yan, E. H. Sargent and J. Tang, Efficient and stable emission of warm-white light from lead-free halide double perovskites, *Nature*, 2018, **563**, 541–545.

70 B. Gholipour, G. Adamo, D. Cortecchia, H. N. Krishnamoorthy, M. D. Birowosuto, N. I. Zheludev and C. Soci, Organometallic perovskite metasurfaces, *Adv. Mater.*, 2017, **29**, 1604268.

71 N. Pourdavoud, S. Wang, A. Mayer, T. Hu, Y. Chen, A. Marianovich, W. Kowalsky, R. Heiderhoff, H. C. Scheer and T. Riedl, Photonic Nanostructures Patterned by Thermal Nanoimprint Directly into Organo-Metal Halide Perovskites, *Adv. Mater.*, 2017, **29**, 1605003.

72 I. L. Braly, D. W. DeQuilettes, L. M. Pazos-Outón, S. Burke, M. E. Ziffer, D. S. Ginger and H. W. Hillhouse, Hybrid perovskite films approaching the radiative limit with over 90% photoluminescence quantum efficiency, *Nat. Photonics*, 2018, **12**, 355–361.

73 W. Yin, T. Shi and Y. Yan, Unusual defect physics in CH3NH3PbI3 perovskite solar cell absorber, *Appl. Phys. Lett.*, 2014, **104**, 063903.

74 T. Leijtens, G. E. Eperon, A. J. Barker, G. Grancini, W. Zhang, J. M. Ball, A. R. S. Kandada, H. J. Snaith and A. Petrozza, Carrier trapping and recombination: the role of defect physics in enhancing the open circuit voltage of metal halide perovskite solar cells, *Energy Environ. Sci.*, 2016, **9**, 3472–3481.

75 E. Aydin, M. De Bastiani and S. De Wolf, Defect and contact passivation for perovskite solar cells, *Adv. Mater.*, 2019, **31**, 1900428.

76 Q. Jiang, Y. Zhao, X. Zhang, X. Yang, Y. Chen, Z. Chu, Q. Ye, X. Li, Z. Yin and J. You, Surface passivation of perovskite film for efficient solar cells, *Nat. Photonics*, 2019, **13**, 460–466.

77 Z. Li, A. Sun, C. Tian, R. Zhuang, Y. Zheng, X. Wu, B. Ouyang, J. Du, J. Cai, J. Chen, T. Xue, R. Li, T. Cen, Y. Zhao, K. Zhao, Q. Chen and C.-C. Chen, Sustainable Molecular Passivation *via* Heat-Induced Disaggregation and Redox Reactions for Inverted Perovskite Solar Cells, *ACS Energy Lett.*, 2024, **9**, 5471–5482.

78 W. Luo, H. Wen, Y. Guo, T. Yin, H. Tan, Z. Zhang, S. Si, Z. Zhang, H. Wu and S. Huang, Simultaneous ultraviolet conversion and defect passivation stabilize efficient and operational durable perovskite solar cells, *Adv. Funct. Mater.*, 2024, **34**, 2400474.

79 Z. Iqbal, F. Zu, A. Musiienko, E. Gutierrez-Partida, H. Köbler, T. W. Gries, G. V. Sannino, L. Canil, N. Koch, M. Stolterfoht, D. Neher, M. Pavone, A. B. Munoz-Garcia, A. Abate and Q. Wang, Interface modification for energy level alignment and charge extraction in CsPbI3 perovskite solar cells, *ACS Energy Lett.*, 2023, **8**, 4304–4314.

80 R. Azmi, D. S. Utomo, B. Vishal, S. Zhumagali, P. Dally, A. M. Risqi, A. Prasetio, E. Ugur, F. Cao, I. F. Imran, A. A. Said, A. R. Pininti, A. S. Subbiah, E. Aydin, C. Xiao, S. I. Seok and S. De Wolf, Double-side 2D/3D

heterojunctions for inverted perovskite solar cells, *Nature*, 2024, **628**, 93–98.

81 A. Krishna, S. Gottis, M. K. Nazeeruddin and F. Sauvage, Mixed dimensional 2D/3D hybrid perovskite absorbers: the future of perovskite solar cells?, *Adv. Funct. Mater.*, 2019, **29**, 1806482.

82 J. Wen, Y. Zhao, P. Wu, Y. Liu, X. Zheng, R. Lin, S. Wan, K. Li, H. Luo, Y. Tian, L. Li and H. Tan, Heterojunction formed *via* 3D-to-2D perovskite conversion for photostable wide-bandgap perovskite solar cells, *Nat. Commun.*, 2023, **14**, 7118.

83 R. He, Z. Yi, Y. Luo, J. Luo, Q. Wei, H. Lai, H. Huang, B. Zou, G. Cui, W. Wang, C. Xiao, S. Ren, C. Chen, C. Wang, G. Xing, F. Fu and D. Zhao, Pure 2D Perovskite Formation by Interfacial Engineering Yields a High Open-Circuit Voltage beyond 1.28 V for 1.77-eV Wide-Bandgap Perovskite Solar Cells, *Adv. Sci.*, 2022, **9**, 2203210.

84 C. A. R. Perini, E. Rojas-Gatjens, M. Ravello, A. F. Castro-Mendez, J. Hidalgo, Y. An, S. Kim, B. Lai, R. Li, C. Silva-Acuña and J. P. Correa-Baena, Interface Reconstruction from Ruddlesden–Popper Structures Impacts Stability in Lead Halide Perovskite Solar Cells, *Adv. Mater.*, 2022, **34**, 2204726.

85 S. M. Park, M. Wei, J. Xu, H. R. Atapattu, F. T. Eickemeyer, K. Darabi, L. Grater, Y. Yang, C. Liu, S. Teale, B. Chen, H. Chen, T. Wang, L. Zeng, A. Maxwell, Z. Wang, K. R. Rao, Z. Cai, S. M. Zakeeruddin, J. T. Pham, C. M. Risko, A. Amassian, M. G. Kanatzidis, K. R. Graham, M. Gratzel and E. H. Sargent, Engineering ligand reactivity enables high-temperature operation of stable perovskite solar cells, *Science*, 2023, **381**, 209–215.

86 Y. Yang, S. Chen, Z. Dai, H. Wei, S. Wan, Y. Chen, J. Sun, Z. Liu, L. Ding, H. Xia, R. Chen and H. Wang, Bridged Carbolong Modulating Interfacial Charge Transfer Enhancement for High-Performance Inverted Perovskite Solar Cells, *Angew. Chem., Int. Ed.*, 2025, **137**, e202420262.

87 Z. Xiong, X. Chen, B. Zhang, G. O. Odunmbaku, Z. Ou, B. Guo, K. Yang, Z. Kan, S. Lu, S. Chen, N. A. N. Ouedraogo, Y. Cho, C. Yang, J. Chen and K. Sun, Simultaneous Interfacial Modification and Crystallization Control by Biguanide Hydrochloride for Stable Perovskite Solar Cells with PCE of 24.4%, *Adv. Mater.*, 2022, **34**, 2106118.

88 F. Pei, Q. Wang, Z. Wei, X. Zhuang, X. Cheng, K. Li, Y. Cui, L. Wang, Z. Huang, Z. Zhang, T. Xu, Y. Zhang, T. Cheng, J. Tang, G. Liu, C. Zhu, Y. Huo, S. Li, C. Wu, X. Wang, H. Zhou, Y. Chen and Q. Chen, Tailoring Perovskite/C60 Interface by Reactive Passivators for Stable Tandem Solar Cells, *Adv. Funct. Mater.*, 2024, **34**, 2410737.

89 D. Menzel, A. Al-Ashouri, A. Tejada, I. Levine, J. A. Guerra, B. Rech, S. Albrecht and L. Korte, Field Effect Passivation in Perovskite Solar Cells by a LiF Interlayer, *Adv. Energy Mater.*, 2022, **12**, 2201109.

90 S.-G. Choi, S.-K. Jung, J.-H. Lee, J.-H. Kim, W. Zheng and J.-W. Lee, LiF in Inverted Perovskite Solar Cells: Dipole or Doping?, *ACS Energy Lett.*, 2024, **9**, 5360–5363.

91 H. Dong, C. Zhang, W. Nie, S. Duan, C. N. Saggau, M. Tang, M. Zhu, Y. S. Zhao, L. Ma and O. G. Schmidt, Interfacial Chemistry Triggers Ultrafast Radiative Recombination in Metal Halide Perovskites, *Angew. Chem., Int. Ed.*, 2022, **61**, e202115875.

92 W. Peng, K. Mao, F. Cai, H. Meng, Z. Zhu, T. Li, S. Yuan, Z. Xu, X. Feng and J. Xu, Reducing nonradiative recombination in perovskite solar cells with a porous insulator contact, *Science*, 2023, **379**, 683–690.

93 I. Levine, A. Al-Ashouri, A. Musiienko, H. Hempel, A. Magomedov, A. Drevilkauskaite, V. Getautis, D. Menzel, K. Hinrichs, T. Unold, S. Albrecht and T. Dittrich, Charge transfer rates and electron trapping at buried interfaces of perovskite solar cells, *Joule*, 2021, **5**, 2915–2933.

94 H. Xu, Y. Miao, N. Wei, H. Chen, Z. Qin, X. Liu, X. Wang, Y. Qi, T. Zhang and Y. Zhao, CsI enhanced buried interface for efficient and UV-robust perovskite solar cells, *Adv. Energy Mater.*, 2022, **12**, 2103151.

95 X. Zuo, B. Kim, B. Liu, D. He, L. Bai, W. Wang, C. Xu, Q. Song, C. Jia, Z. Zang, D. Lee, X. Li and J. Chen, Passivating buried interface *via* self-assembled novel sulfonium salt toward stable and efficient perovskite solar cells, *Chem. Eng. J.*, 2022, **431**, 133209.

96 Y. Dong, W. Shen, W. Dong, C. Bai, J. Zhao, Y. Zhou, F. Huang, Y. B. Cheng and J. Zhong, Chlorobenzenesulfonic Potassium Salts as the Efficient Multifunctional Passivator for the Buried Interface in Regular Perovskite Solar Cells, *Adv. Energy Mater.*, 2022, **12**, 2200417.

97 J. Chen and N. G. Park, Causes and solutions of recombination in perovskite solar cells, *Adv. Mater.*, 2019, **31**, 1803019.

98 L. K. Ono, S. Liu and Y. Qi, Reducing detrimental defects for high-performance metal halide perovskite solar cells, *Angew. Chem., Int. Ed.*, 2020, **59**, 6676–6698.

99 X. Jiang, B. Liu, X. Wu, S. Zhang, D. Zhang, X. Wang, S. Gao, Z. Huang, H. Wang, B. Li, Z. Xiao, T. Chen, A. K. Y. Jen, S. Xiao, S. Yang and Z. Zhu, Top-Down Induced Crystallization Orientation toward Highly Efficient p-i-n Perovskite Solar Cells, *Adv. Mater.*, 2024, **36**, 2313524.

100 J. Wang, S. Luo, Y. Lin, Y. Chen, Y. Deng, Z. Li, K. Meng, G. Chen, T. Huang, S. Xiao, H. Huang, C. Zhou, L. Ding, J. He, J. Huang and Y. Yuan, Templated growth of oriented layered hybrid perovskites on 3D-like perovskites, *Nat. Commun.*, 2020, **11**, 582.

101 Z. Cai, Z. Yao, Z. Xing, R. Dai, Z. Huang, X. Meng, X. Hu and Y. Chen, A Buried Interface Fastening Approach for Efficient and Flexible Perovskite Photovoltaics, *Adv. Funct. Mater.*, 2025, 2505921.

102 D. Liu, D. Luo, A. N. Iqbal, K. W. P. Orr, T. A. S. Doherty, Z.-H. Lu, S. D. Stranks and W. Zhang, Strain analysis and engineering in halide perovskite photovoltaics, *Nat. Mater.*, 2021, **20**, 1337–1346.

103 H. Zhang and N. G. Park, Strain control to stabilize perovskite solar cells, *Angew. Chem., Int. Ed.*, 2022, **134**, e202212268.

104 C. Zhu, X. Niu, Y. Fu, N. Li, C. Hu, Y. Chen, X. He, G. Na, P. Liu, H. Zai, Y. Ge, Y. Lu, X. Ke, Y. Bai, S. Yang, P. Chen, Y. Li, M. Sui, L. Zhang, H. Zhou and Q. Chen, Strain engineering in perovskite solar cells and its impacts on carrier dynamics, *Nat. Commun.*, 2019, **10**, 815.

105 Q. Du, C. Zhu, Z. Yin, G. Na, C. Cheng, Y. Han, N. Liu, X. Niu, H. Zhou, H. Chen, L. Zhang, S. Jin and Q. Chen, Stacking Effects on Electron–Phonon Coupling in Layered Hybrid Perovskites *via* Microstrain Manipulation, *ACS Nano*, 2020, **14**, 5806–5817.

106 G. Zheng, C. Zhu, J. Ma, X. Zhang, G. Tang, R. Li, Y. Chen, L. Li, J. Hu, J. Hong, Q. Chen, X. Gao and H. Zhou, Manipulation of facet orientation in hybrid perovskite polycrystalline films by cation cascade, *Nat. Commun.*, 2018, **9**, 2793.

107 D. Xue, Y. Hou, S.-C. Liu, M. Wei, B. Chen, Z. Huang, Z. Li, B. Sun, A. H. Proppe, Y. Dong, M. I. Saidaminov, S. O. Kelley, J.-S. Hu and E. H. Sargent, Regulating strain in perovskite thin films through charge-transport layers, *Nat. Commun.*, 2020, **11**, 1514.

108 Q. Zhou, D. He, Q. Zhuang, B. Liu, R. Li, H. Li, Z. Zhang, H. Yang, P. Zhao, Y. He, Z. Zang and J. Chen, Revealing Steric-Hindrance-Dependent Buried Interface Defect Passivation Mechanism in Efficient and Stable Perovskite Solar Cells with Mitigated Tensile Stress, *Adv. Funct. Mater.*, 2022, **32**, 2205507.

109 A. Al-Ashouri, A. Magomedov, M. Roß, M. Jošt, M. Talaikis, G. Chistiakova, T. Bertram, J. A. Márquez, E. Köhnen, E. Kasparavičius, S. Levcenco, L. Gil-Escrig, C. J. Hages, R. Schlatmann, B. Rech, T. Malinauskas, T. Unold, C. A. Kaufmann, L. Korte, G. Niaura, V. Getautis and S. Albrecht, Conformal monolayer contacts with lossless interfaces for perovskite single junction and monolithic tandem solar cells, *Energy Environ. Sci.*, 2019, **12**, 3356–3369.

110 J. Zhang, J. Long, Z. Huang, J. Yang, X. Li, R. Dai, W. Sheng, L. Tan and Y. Chen, Obstructing interfacial reaction between NiOx and perovskite to enable efficient and stable inverted perovskite solar cells, *Chem. Eng. J.*, 2021, **426**, 131357.

111 F. H. Isikgor, S. Zhumagali, L. V. T. Merino, M. De Bastiani, I. McCulloch and S. De Wolf, Molecular engineering of contact interfaces for high-performance perovskite solar cells, *Nat. Rev. Mater.*, 2023, **8**, 89–108.

112 X. Deng, F. Qi, F. Li, S. Wu, F. R. Lin, Z. Zhang, Z. Guan, Z. Yang, C. S. Lee and A. K. Y. Jen, Co-assembled monolayers as hole-selective contact for high-performance inverted perovskite solar cells with optimized recombination loss and long-term stability, *Angew. Chem., Int. Ed.*, 2022, **134**, e202203088.

113 A. Al-Ashouri, E. Köhnen, B. Li, A. Magomedov, H. Hempel, P. Caprioglio, J. A. Márquez, A. B. Morales Vilches, E. Kasparavicius, J. A. Smith, N. Phung, D. Menzel, M. Grischek, L. Kegelmann, D. Skroblin, C. Gollwitzer, T. Malinauskas, M. Jost, G. Matic, B. Rech, R. Schlatmann, M. Topic, L. Korte, A. Abate, B. Stannowski, D. Neher, M. Stolterfoht, T. Unold, V. Getautis and S. Albrecht, Monolithic perovskite/silicon tandem solar cell with> 29% efficiency by enhanced hole extraction, *Science*, 2020, **370**, 1300–1309.

114 H. Bi, Y. Fujiwara, G. Kapil, D. Tavgeniene, Z. Zhang, L. Wang, C. Ding, S. R. Sahamir, A. K. Baranwal, Y. Sanehira, K. Takeshi, G. Shi, T. Bessho, H. Segawa, S. Grigalevicius, Q. Shen and S. Hayase, Perovskite Solar Cells Consisting of PTAA Modified with Monomolecular Layer and Application to All-Perovskite Tandem Solar Cells with Efficiency over 25%, *Adv. Funct. Mater.*, 2023, **33**, 2300089.

115 Z. Yi, W. Wang, R. He, J. Zhu, W. Jiao, Y. Luo, Y. Xu, Y. Wang, Z. Zeng, K. Wei, J. Zhang, S.-W. Tsang, C. Chen, W. Tang and D. Zhao, Achieving a high open-circuit voltage of 1.339 V in 1.77 eV wide-bandgap perovskite solar cells via self-assembled monolayers, *Energy Environ. Sci.*, 2024, **17**, 202–209.

116 H. Tang, Z. Shen, Y. Shen, G. Yan, Y. Wang, Q. Han and L. Han, Reinforcing self-assembly of hole transport molecules for stable inverted perovskite solar cells, *Science*, 2024, **383**, 1236–1240.

117 S. Wang, T. Sakurai, W. Wen and Y. Qi, Energy Level Alignment at Interfaces in Metal Halide Perovskite Solar Cells, *Adv. Mater. Interfaces*, 2018, **5**, 1800260.

118 F. Zhang, D. Zheng, D. Yu, S. Wu, K. Wang, L. Peng, S. F. Liu and D. Yang, Perovskite photovoltaic interface: From optimization towards exemption, *Nano Energy*, 2024, **124**, 109503.

119 B. Lyu, L. Yang, Y. Luo, X. Zhang and J. Zhang, Counter electrodes for perovskite solar cells: materials, interfaces and device stability, *J. Mater. Chem. C*, 2022, **10**, 10775–10798.

120 L. Liang, Y. Cai, X. Li, M. K. Nazeeruddin and P. Gao, All that glitters is not gold: Recent progress of alternative counter electrodes for perovskite solar cells, *Nano Energy*, 2018, **52**, 211–238.

121 H. Back, G. Kim, J. Kim, J. Kong, T. K. Kim, H. Kang, H. Kim, J. Lee, S. Lee and K. Lee, Achieving long-term stable perovskite solar cells via ion neutralization, *Energy Environ. Sci.*, 2016, **9**, 1258–1263.

122 S. Guo, X. Sun, C. Ding, R. Huang, M. Tan, L. Zhang, Q. Luo, F. Li, J. Jin and C.-Q. Ma, Non-uniform chemical corrosion of metal electrode of p–i–n type of perovskite solar cells caused by the diffusion of CH3NH3I, *Energy Technol.*, 2020, **8**, 2000250.

123 J. Yang, Q. Cao, T. Wang, B. Yang, X. Pu, Y. Zhang, H. Chen, I. Tojiboyev, Y. Li, L. Etgar, X. Li and A. Hagfeldt, Inhibiting metal-inward diffusion-induced degradation through strong chemical coordination toward stable and efficient inverted perovskite solar cells, *Energy Environ. Sci.*, 2022, **15**, 2154–2163.

124 Y. Yuan, Q. Wang, Y. Shao, H. Lu, T. Li, A. Gruverman and J. Huang, Electric-Field-Driven Reversible Conversion Between Methylammonium Lead Triiodide Perovskites and Lead Iodide at Elevated Temperatures, *Adv. Energy Mater.*, 2016, **6**, 1501803.

125 D. Yang, W. Ming, H. Shi, L. Zhang and M.-H. Du, Fast diffusion of native defects and impurities in perovskite solar cell material CH3NH3PbI3, *Chem. Mat.*, 2016, **28**, 4349–4357.

126 A. Agresti, A. Pazniak, S. Pescetelli, A. Di Vito, D. Rossi, A. Pecchia, M. Auf der Maur, A. Liedl, R. Larciprete, D. V. Kuznetsov, D. Saranin and A. Di Carlo, Titanium-carbide MXenes for work function and interface engineering in perovskite solar cells, *Nat. Mater.*, 2019, **18**, 1228–1234.

127 M. Li, C. Zhao, Z. K. Wang, C. C. Zhang, H. K. H. Lee, A. Pockett, J. Barbé, W. C. Tsoi, Y. G. Yang, M. J. Carnie, X. Y. Gao, W. X. Yang, J. R. Durrant, L. S. Liao and S. M. Jain, Interface Modification by Ionic Liquid: A Promising Candidate for Indoor Light Harvesting and Stability Improvement of Planar Perovskite Solar Cells, *Adv. Energy Mater.*, 2018, **8**, 1801509.

128 C. Chen, S. Zhang, S. Wu, W. Zhang, H. Zhu, Z. Xiong, Y. Zhang and W. Chen, Effect of BCP buffer layer on eliminating charge accumulation for high performance of inverted perovskite solar cells, *RSC Adv.*, 2017, **7**, 35819–35826.

129 P. Chen, Y. Xiao, J. Hu, S. Li, D. Luo, R. Su, P. Caprioglio, P. Kaienburg, X. Jia, N. Chen, J. Wu, Y. Sui, P. Tang, H. Yan, T. Huang, M. Yu, Q. Li, L. Zhao, C.-H. Hou, Y.-W. You, J.-J. Shyue, D. Wang, X. Li, Q. Zhao, Q. Gong, Z.-H. Lu, H. J. Snaith and R. Zhu, Multifunctional ytterbium oxide buffer for perovskite solar cells, *Nature*, 2024, **625**, 516–522.

130 T. D. Nguyen, D. Yeo, R. K. Chitumalla, S. J. Kim, G. H. Jeong, D. G. Kwun, J. Jang, I. H. Jung and J. Y. Seo, Tailor-Made Buffer Materials: Advancing Uniformity and Stability in Perovskite Solar Cells, *Adv. Energy Mater.*, 2025, **15**, 2403633.

131 B. Gupta, M. A. Hossain, A. Riaz, A. Sharma, D. Zhang, H. H. Tan, C. Jagadish, K. Catchpole, B. Hoex and S. Karuturi, Recent advances in materials design using atomic layer deposition for energy applications, *Adv. Funct. Mater.*, 2022, **32**, 2109105.

132 R. Singh, S. Ghosh, A. S. Subbiah, N. Mahuli and S. K. Sarkar, ALD Al2O3 on hybrid perovskite solar cells: Unveiling the growth mechanism and long-term stability, *Sol. Energy Mater. Sol. Cells*, 2020, **205**, 110289.

133 J. A. Raiford, S. T. Oyakhire and S. F. Bent, Applications of atomic layer deposition and chemical vapor deposition for perovskite solar cells, *Energy Environ. Sci.*, 2020, **13**, 1997–2023.

134 H. Li, G. Xie, J. Fang, X. Wang, S. Li, D. Lin, D. Wang, N. Huang, H. Peng and L. Qiu, Holistic dielectric and buffer interfacial layers enable high-efficiency perovskite solar cells and modules, *Nano Energy*, 2024, **124**, 109507.

135 D. Choi, D. Shin, C. Li, Y. Liu, A. S. R. Bati, D. E. Kachman, Y. Yang, J. Li, Y. J. Lee, M. Li, S. Penukula, D. B. Kim, H. Shin, C.-H. Chen, S. M. Park, C. Liu, A. Maxwell, H. Wan, N. Rolston, E. H. Sargent and B. Chen, Carboxyl-functionalized perovskite enables ALD growth of a compact and uniform ion migration barrier, *Joule*, 2025, **9**, 101801.

136 M. Jošt, L. Kegelmann, L. Korte and S. Albrecht, Monolithic Perovskite Tandem Solar Cells: A Review of the Present Status and Advanced Characterization Methods Toward 30% Efficiency, *Adv. Energy Mater.*, 2020, **10**, 1904102.

137 R. He, S. Ren, C. Chen, Z. Yi, Y. Luo, H. Lai, W. Wang, G. Zeng, X. Hao, Y. Wang, J. Zhang, C. Wang, L. Wu, F. Fu and D. Zhao, Wide-bandgap organic–inorganic hybrid and all-inorganic perovskite solar cells and their application in all-perovskite tandem solar cells, *Energy Environ. Sci.*, 2021, **14**, 5723–5759.

138 S. Zhumagali, C. Li, M. Marcinskas, P. Dally, Y. Liu, E. Ugur, C. E. Petoukhoff, M. Ghadiyali, A. Prasetio, M. Marengo, A. R. Pininti, R. Azmi, U. Schwingenschlögl, F. Laquai, V. Getautis, T. Malinauskas, E. Aydin, E. H. Sargent and S. De Wolf, Efficient Narrow Bandgap Pb-Sn Perovskite Solar Cells Through Self-Assembled Hole Transport Layer with Ionic Head, *Adv. Energy Mater.*, 2025, **15**, 2404617.

139 M. I. Saidaminov, I. Spanopoulos, J. Abed, W. Ke, J. Wicks, M. G. Kanatzidis and E. H. Sargent, Conventional Solvent Oxidizes Sn(II) in Perovskite Inks, *ACS Energy Lett.*, 2020, **5**, 1153–1155.

140 S. Wang, H. Yao, W. Zhu, C. Wu, Z. Tang, J. Liu, L. Ding and F. Hao, Stabilization of perovskite lattice and suppression of Sn2+/Sn4+ oxidation via formamidine acetate for high efficiency tin perovskite solar cells, *Adv. Funct. Mater.*, 2023, **33**, 2215041.

141 F. Hao, C. C. Stoumpos, R. P. H. Chang and M. G. Kanatzidis, Anomalous Band Gap Behavior in Mixed Sn and Pb Perovskites Enables Broadening of Absorption Spectrum in Solar Cells, *J. Am. Chem. Soc.*, 2014, **136**, 8094–8099.

142 C. T. Crespo, Contributions to Optical Properties and Efficiencies of Methyl–Ammonium Lead, Tin, and Germanium Iodide Perovskites, *J. Phys. Chem. C*, 2020, **124**, 12305–12310.

143 D. Yu, M. Pan, G. Liu, X. Jiang, X. Wen, W. Li, S. Chen, W. Zhou, H. Wang, Y. Lu, M. Ma, Z. Zang, P. Cheng, Q. Ji, F. Zheng and Z. Ning, Electron-withdrawing organic ligand for high-efficiency all-perovskite tandem solar cells, *Nat. Energy*, 2024, **9**, 298–307.

144 R. Lin, Y. Wang, Q. Lu, B. Tang, J. Li, H. Gao, Y. Gao, H. Li, C. Ding, J. Wen, P. Wu, C. Liu, S. Zhao, K. Xiao, Z. Liu, C. Ma, Y. Deng, L. Li, F. Fan and H. Tan, All-perovskite tandem solar cells with 3D/3D bilayer perovskite heterojunction, *Nature*, 2023, **620**, 994–1000.

145 Q. Zhang, X. Chen, E. L. Lim, L. Shi and Z. Wei, Advancing all-perovskite two-terminal tandem solar cells: optimization of wide- and narrow-bandgap perovskites and interconnecting layers, *Energy Environ. Sci.*, 2025, **18**, 3060–3084.

146 M. Konstantakou and T. Stergiopoulos, A critical review on tin halide perovskite solar cells, *J. Mater. Chem. A*, 2017, **5**, 11518–11549.

147 L. E. Mundt, J. Tong, A. F. Palmstrom, S. P. Dunfield, K. Zhu, J. J. Berry, L. T. Schelhas and E. L. Ratcliff,

Surface-Activated Corrosion in Tin–Lead Halide Perovskite Solar Cells, *ACS Energy Lett.*, 2020, **5**, 3344–3351.

148 W. Zhang, H. Liu, Y. Qu, J. Cui, W. Zhang, T. Shi and H. L. Wang, B-Site Co-Doping Coupled with Additive Passivation Pushes the Efficiency of Pb–Sn Mixed Inorganic Perovskite Solar Cells to Over 17%, *Adv. Mater.*, 2024, **36**, 2309193.

149 C. Li, L. Chen, F. Jiang, Z. Song, X. Wang, A. Balvanz, E. Ugur, Y. Liu, C. Liu, A. Maxwell, H. Chen, Y. Liu, Z. Wang, P. Xia, Y. Li, S. Fu, N. Sun, C. R. Grice, X. Wu, Z. Fink, Q. Hu, L. Zeng, E. Jung, J. Wang, S. M. Park, D. Luo, C. Chen, J. Shen, Y. Han, C. A. R. Perini, J.-P. Correa-Baena, Z.-H. Lu, T. P. Russell, S. De Wolf, M. G. Kanatzidis, D. S. Ginger, B. Chen, Y. Yan and E. H. Sargent, Diamine chelates for increased stability in mixed Sn–Pb and all-perovskite tandem solar cells, *Nat. Energy*, 2024, **9**, 1388–1396.

150 Z. Zhang, J. Liang, J. Wang, Y. Zheng, X. Wu, C. Tian, A. Sun, Y. Huang, Z. Zhou, Y. Yang, Y. Liu, C. Tang and C. C. Chen, DMSO-Free Solvent Strategy for Stable and Efficient Methylammonium-Free Sn–Pb Alloyed Perovskite Solar Cells, *Adv. Energy Mater.*, 2023, **13**, 2300181.

151 Y. J. Heo, H. J. Jang, J. H. Lee, S. B. Jo, S. Kim, D. H. Ho, S. J. Kwon, K. Kim, I. Jeon, J. M. Myoung, J. Y. Lee, J.-W. Lee and J. H. Cho, Enhancing performance and stability of tin halide perovskite light emitting diodes via coordination engineering of Lewis acid–base adducts, *Adv. Funct. Mater.*, 2021, **31**, 2106974.

152 Y. Zhang, B. Zhao, L. Liu, J. Zhou, X. Ma and N. Wang, Efficient Tin perovskite solar cells via suppressing autoxidation in inert atmosphere, *Small*, 2024, **20**, 2306115.

153 M. Yang, Y. Bai, Y. Meng, R. Tian, K. Sun, X. Lu, H. Pan, J. Wang, S. Zhou, J. Zhang, Z. Song, Y. Wang, C. Liu and Z. Ge, Sn-Pb Perovskite with Strong Light and Oxygen Stability for All-Perovskite Tandem Solar Cells, *Adv. Mater.*, 2025, **37**, 2415627.

154 J. Zhou, S. Fu, S. Zhou, L. Huang, C. Wang, H. Guan, D. Pu, H. Cui, C. Wang, T. Wang, W. Meng, G. Fang and W. Ke, Mixed tin-lead perovskites with balanced crystallization and oxidation barrier for all-perovskite tandem solar cells, *Nat. Commun.*, 2024, **15**, 2324.

155 X. Hu, Y. Pan, J. Wang, Z. Liu and W. Chen, Reducing energy disorder by stabilizing octahedral lattice with thiocyanate for efficient and stable Sn-Pb mixed perovskite solar cells, *Nano Energy*, 2023, **118**, 108937.

156 G. Liu, G. Yang, W. Feng, H. Li, M. Yang, Y. Zhong, X. Jiang and W. Q. Wu, Regulating Surface Metal Abundance via Lattice-Matched Coordination for Versatile and Environmentally-Viable Sn-Pb Alloying Perovskite Solar Cells, *Adv. Mater.*, 2024, **36**, 2405860.

157 W. Liao, D. Zhao, Y. Yu, C. R. Grice, C. Wang, A. J. Cimaroli, P. Schulz, W. Meng, K. Zhu, R. G. Xiong and Y. Yan, Lead-Free Inverted Planar Formamidinium Tin Triiodide Perovskite Solar Cells Achieving Power Conversion Efficiencies up to 6.22%, *Adv. Mater.*, 2016, **28**, 9333–9340.

158 K. J. Savill, A. M. Ulatowski, M. D. Farrar, M. B. Johnston, H. J. Snaith and L. M. Herz, Impact of Tin Fluoride Additive on the Properties of Mixed Tin-Lead Iodide Perovskite Semiconductors, *Adv. Funct. Mater.*, 2020, **30**, 2005594.

159 W. Yan, C. Li, C. Peng, S. Tan, J. Zhang, H. Jiang, F. Xin, F. Yue and Z. Zhou, Hot-Carrier Cooling Regulation for Mixed Sn-Pb Perovskite Solar Cells, *Adv. Mater.*, 2024, **36**, 2312170.

160 Q. Tai, X. Guo, G. Tang, P. You, T. W. Ng, D. Shen, J. Cao, C. K. Liu, N. Wang, Y. Zhu, C.-S. Lee and F. Yan, Antioxidant grain passivation for air-stable tin-based perovskite solar cells, *Angew. Chem., Int. Ed.*, 2019, **58**, 806–810.

161 J. Chen, J. Du, J. Cai, B. Ouyang, Z. Li, X. Wu, C. Tian, A. Sun, R. Zhuang, X. Wu, C. Chen, T. Cen, R. Li, T. Xue, Y. Zhao, K. Zhao, Q. Chen and C.-C. Chen, Lewis Base Strategy for Crystallization Control and Buried Interface Passivation on Hydrophobic PTAA Substrate for Efficient Tin–Lead Perovskite and All-Perovskite Tandem Solar Cells, *ACS Energy Lett.*, 2025, **10**, 1117–1128.

162 H. Wang, X. Wan, F. Li, X. He, G. Xu, C. Xu, Z. Jiang, Z. Dai, S. Zhang and Q. Song, Chelating Dual Interface for Efficient and Stable Crystal Growth and Iodine Defect Management in Sn–Pb Perovskite Solar Cells, *ACS Nano*, 2024, **18**, 16867–16877.

163 Y. Chen, K. Wang, W. Chen, T. Li, H. Tu, F. Yang, Z. Kang, Y. Tong and H. Wang, Defects Mitigation and Charge Transport Promotion via a Multifunctional Lewis Base for Efficient 2D/3D Tin Perovskite Solar Cells, *Adv. Energy Mater.*, 2025, 2406024.

164 R. K. Gunasekaran, J. Jung, S. W. Yang, D. Im, W. C. Choi, Y. Yun and S. Lee, Regulating Surface Heterogeneity Maximizes Photovoltage and Operational Stability in Tin–Lead Perovskite Solar Cells, *ACS Energy Lett.*, 2023, **9**, 102–109.

165 K. Zhang, A. Späth, O. Almora, V. M. Le Corre, J. Wortmann, J. Zhang, Z. Xie, A. Barabash, M. S. Hammer, T. Heumüller, J. Min, R. Fink, L. Lüer, N. Li and C. J. Brabec, Suppressing Nonradiative Recombination in Lead–Tin Perovskite Solar Cells through Bulk and Surface Passivation to Reduce Open Circuit Voltage Losses, *ACS Energy Lett.*, 2022, **7**, 3235–3243.

166 T. Zhang, F. Qian, H. Chen, H. Zheng, L. Wang, S. Yuan, Y. Wu, Z. D. Chen and S. Li, Critical role of post-treatment induced surface reconstruction for high performance inorganic tin-lead perovskite solar cells, *Chem. Eng. J.*, 2024, **479**, 147554.

167 Y. Pan, J. Wang, Z. Sun, J. Zhang, Z. Zhou, C. Shi, S. Liu, F. Ren, R. Chen, Y. Cai, H. Sun, B. Liu, Z. Zhang, Z. Zhao, Z. Cai, X. Qin, Z. Zhao, Y. Ji, N. Li, W. Huang, Z. Liu and W. Chen, Surface chemical polishing and passivation minimize non-radiative recombination for all-perovskite tandem solar cells, *Nat. Commun.*, 2024, **15**, 7335.

168 J. Cao, C. k. Liu, Y. Xu, H. L. Loi, T. Wang, M. G. Li, L. Liu and F. Yan, High-Performance Ideal Bandgap Sn-Pb Mixed Perovskite Solar Cells Achieved by MXene Passivation, *Small*, 2024, **20**, 2403920.

169 A. W. Ho-Baillie, J. Zheng, M. A. Mahmud, F.-J. Ma, D. R. McKenzie and M. A. Green, Recent progress and future prospects of perovskite tandem solar cells, *Appl. Phys. Rev.*, 2021, **8**, 041307.

170 C. Yan, S. Barlow, Z. Wang, H. Yan, A. K. Y. Jen, S. R. Marder and X. Zhan, Non-fullerene acceptors for organic solar cells, *Nat. Rev. Mater.*, 2018, **3**, 18003.

171 Y. Guo, G. Han and Y. Yi, The Intrinsic Role of the Fusion Mode and Electron-Deficient Core in Fused-Ring Electron Acceptors for Organic Photovoltaics, *Angew. Chem., Int. Ed.*, 2022, **61**, e202205975.

172 Y. Gong, S. Tan, X. Li, S. Qin, X. Li, T. Zou, Y. Li, M. Yuan, Z. Zhang, H. Hu, T. Liang, J. Zhang, L. Meng, F. Liu and Y. Li, Molecular Geometry-Property Relationship of Benzodipyrrole-Based A-DA'D-A Type Acceptors for High-Performance Organic Solar Cells, *Angew. Chem., Int. Ed.*, 2025, **64**, e202505366.

173 W. Liu, Y. Nai, W. Chen, G. Zhen, S. Liang, X. Guo, J. Yuan and Y. Zou, Effect of semi-perfluoroalkyl chains on A-DA′D-A type small molecule acceptor in organic solar cells, *Sci. China Mater.*, 2024, **68**, 1445–1451.

174 Z. Jia, S. Qin, L. Meng, Q. Ma, I. Angunawela, J. Zhang, X. Li, Y. He, W. Lai, N. Li, H. Ade, C. J. Brabec and Y. Li, High performance tandem organic solar cells via a strongly infrared-absorbing narrow bandgap acceptor, *Nat. Commun.*, 2021, **12**, 178.

175 C. Li, J. Song, H. Lai, H. Zhang, R. Zhou, J. Xu, H. Huang, L. Liu, J. Gao, Y. Li, M. H. Jee, Z. Zheng, S. Liu, J. Yan, X.-K. Chen, Z. Tang, C. Zhang, H. Y. Woo, F. He, F. Gao, H. Yan and Y. Sun, Non-fullerene acceptors with high crystallinity and photoluminescence quantum yield enable >20% efficiency organic solar cells, *Nat. Mater.*, 2025, **24**, 433–443.

176 I. V. Dyadishchev, A. V. Bakirov, S. M. Peregudova, S. A. Ponomarenko and Y. N. Luponosov, NIR-absorbing donor–acceptor molecules based on fused thienopyrroloindole, *Mendeleev Commun.*, 2023, **33**, 393–396.

177 M. H. Tahir, T. Mubashir, T. U. H. Shah and A. Mahmood, Impact of electron-withdrawing and electron-donating substituents on the electrochemical and charge transport properties of indacenodithiophene-based small molecule acceptors for organic solar cells, *J. Phys. Org. Chem.*, 2019, **32**, e3909.

178 Y. Gong, T. Zou, X. Li, S. Qin, G. Sun, T. Liang, R. Zhou, J. Zhang, J. Zhang, L. Meng, Z. Wei and Y. Li, C-shaped ortho-benzodipyrrole-based acceptors with different electronic effects of top substituents for as-cast green-solvent processed high-performance organic solar cells, *Energy Environ. Sci.*, 2024, **17**, 6844–6855.

179 Y. Zou, H. Chen, X. Bi, X. Xu, H. Wang, M. Lin, Z. Ma, M. Zhang, C. Li, X. Wan, G. Long, Y. Zhaoyang and Y. Chen, Peripheral halogenation engineering controls molecular stacking to enable highly efficient organic solar cells, *Energy Environ. Sci.*, 2022, **15**, 3519–3533.

180 W. Xiong, Y. Cui, Z. Zhang, S. Zhu, Z. Wang, Z. Chai, H. Hu and Y. Chen, Manipulating σ-Hole Interactions in Halogenated Additives for High-Performance Organic Solar Cells with 19.8% Efficiency, *Angew. Chem., Int. Ed.*, 2025, e202500085.

181 Q. Xie, C. Qiao, J. Fang, D. Xia, F. Ding, Q. Wang, G. Xu, S. Shan, X. Liao and Y. Chen, Optimizing Active Layer Morphology of Organic Solar Cells by Constructing Random Copolymers with Simple Third Units, *Macromol. Rapid Commun.*, 2025, **46**, 2400458.

182 C. Zhu, S. Chung, J. Zhao, Y. Sun, B. Zhao, Z. Zhao, S. Kim, K. Cho and Z. Kan, Vertical Phase Regulation with 1,3,5-Tribromobenzene Leads to 18.5% Efficiency Binary Organic Solar Cells, *Adv. Sci.*, 2023, **10**, 2303105.

183 Z. Xia, C. Gao, Z. Xie, M. Wu, H. Chen, T. Li, J. Zhou, T. Cai, H. Hu, J. Shuai, C. Xie, G. Zhang, W. Chen and S. Liu, Isomerization-Controlled Aggregation in Photoactive Layer: An Additive Strategy for Organic Solar Cells with Over 19.5% Efficiency, *Angew. Chem., Int. Ed.*, 2025, **64**, e202421953.

184 A. Liang, Y. Sun, S. Chung, J. Shin, K. Sun, C. Zhu, J. Zhao, Z. Zhao, Y. Zhong, G. Zhang, K. Cho and Z. Kan, Dual-Donor-Induced Crystallinity Modulation Enables 19.23% Efficiency Organic Solar Cells, *Nano-Micro Lett.*, 2025, **17**, 72.

185 Y. Zhang, Y. Zhang, X. Liu, Z. Geng, H. Wang, Z. Xu, Z. Miao, Q. Liang and J. Liu, Controlling the Third Component Distribution Toward High-Efficient Ternary Organic Solar Cells, *Adv. Energy Mater.*, 2025, 2406136.

186 Y. Zhu, A. Gadisa, Z. Peng, M. Ghasemi, L. Ye, Z. Xu, S. Zhao and H. Ade, Rational strategy to stabilize an unstable high-efficiency binary nonfullerene organic solar cells with a third component, *Adv. Energy Mater.*, 2019, **9**, 1900376.

187 E. Trippodo, V. Campisciano, L.-W. Feng, Y. Chen, W. Huang, J. M. Alzola, D. Zheng, V. K. Sangwan, M. C. Hersam, M. R. Wasielewski, B. Pignataro, F. Giacalone, T. J. Marks and A. Facchetti, Air-stable ternary organic solar cells achieved by using fullerene additives in non-fullerene acceptor-polymer donor blends, *J. Mater. Chem. C*, 2023, **11**, 8074–8083.

188 J. Xin, C. Zhao, Z. Geng, W. Xue, Z. Chen, C. Song, H. Yan, Q. Liang, Z. Miao, W. Ma and J. Liu, Elucidate the Thermal Degradation Mechanism of Y6-Based Organic Solar Cells by Establishing Structure-Property Correlation, *Adv. Energy Mater.*, 2024, **14**, 2401433.

189 Y. Cai, Q. Li, G. Lu, H. S. Ryu, Y. Li, H. Jin, Z. Chen, Z. Tang, G. Lu, X. Hao, H. Y. Woo, C. Zhang and Y. Sun, Vertically optimized phase separation with improved exciton diffusion enables efficient organic solar cells with thick active layers, *Nat. Commun.*, 2022, **13**, 2369.

190 S. Cataldo and B. Pignataro, Polymeric Thin Films for Organic Electronics: Properties and Adaptive Structures, *Materials*, 2013, **6**, 1159–1190.

191 L. Zhang, X. Xing, L. Zheng, Z. Chen, L. Xiao, B. Qu and Q. Gong, Vertical phase separation in bulk heterojunction solar cells formed by in situ polymerization of fulleride, *Sci. Rep.*, 2014, **4**, 5071.

192 Y. Wang, S. Zhang, J. Wang, J. Ren, J. Qiao, Z. Chen, Y. Yu, X.-T. Hao and J. Hou, Optimizing Phase Separation and

Vertical Distribution via Molecular Design and Ternary Strategy for Organic Solar Cells with 19.5% Efficiency, *ACS Energy Lett.*, 2024, **9**, 2420–2427.

193 H. Zhuo, X. Li, J. Zhang, S. Qin, J. Guo, R. Zhou, X. Jiang, X. Wu, Z. Chen, J. Li, L. Meng and Y. Li, Giant Molecule Acceptor Enables Highly Efficient Organic Solar Cells Processed Using Non-halogenated Solvent, *Angew. Chem., Int. Ed.*, 2023, **62**, e202303551.

194 X. Xu, L. Yu, H. Meng, L. Dai, H. Yan, R. Li and Q. Peng, Polymer solar cells with 18.74% efficiency: from bulk heterojunction to interdigitated bulk heterojunction, *Adv. Funct. Mater.*, 2022, **32**, 2108797.

195 J. Wang, X. Jiang, H. Wu, G. Feng, H. Wu, J. Li, Y. Yi, X. Feng, Z. Ma, W. Li, K. Vandewal and Z. Tang, Increasing donor-acceptor spacing for reduced voltage loss in organic solar cells, *Nat. Commun.*, 2021, **12**, 6679.

196 Y. Xie, Y. Cai, L. Zhu, R. Xia, L. Ye, X. Feng, H. L. Yip, F. Liu, G. Lu, S. Tan and Y. Sun, Fibril Network Strategy Enables High-Performance Semitransparent Organic Solar Cells, *Adv. Funct. Mater.*, 2020, **30**, 2002181.

197 L. Zhao, S. Zhao, Z. Xu, W. Gong, Q. Yang, X. Fan and X. Xu, Influence of morphology of PCDTBT: PC71BM on the performance of solar cells, *Appl. Phys. A:Mater. Sci. Process.*, 2014, **114**, 1361–1368.

198 Y. Wang, K. Sun, C. Li, C. Zhao, C. Gao, L. Zhu, Q. Bai, C. Xie, P. You, J. Lv, X. Sun, H. Hu, Z. Wang, H. Hu, Z. Tang, B. He, M. Qiu, S. Li and G. Zhang, A Novel Upside-Down Thermal Annealing Method Toward High-Quality Active Layers Enables Organic Solar Cells with Efficiency Approaching 20%, *Adv. Mater.*, 2024, **36**, 2411957.

199 S. Liu, J. Yuan, W. Deng, M. Luo, Y. Xie, Q. Liang, Y. Zou, Z. He, H. Wu and Y. Cao, High-efficiency organic solar cells with low non-radiative recombination loss and low energetic disorder, *Nat. Photonics*, 2020, **14**, 300–305.

200 H. Yin, Y. Cui, D. Chen, S. Liu, T. Wu, M. Yu, L. Ye, A. Liang and Y. Chen, Preparation of Dual-Asymmetric Acceptors via Selenium Substitution Combined with Terminal Group Optimization Strategy for High Efficiency Organic Solar Cells, *J. Am. Chem. Soc.*, 2025, **147**, 8796–8808.

201 J. Yao, T. Kirchartz, M. S. Vezie, M. A. Faist, W. Gong, Z. He, H. Wu, J. Troughton, T. Watson, D. Bryant and J. Nelson, Quantifying losses in open-circuit voltage in solution-processable solar cells, *Phys. Rev. Appl.*, 2015, **4**, 014020.

202 D. Qian, Z. Zheng, H. Yao, W. Tress, T. R. Hopper, S. Chen, S. Li, J. Liu, S. Chen, J. Zhang, X.-K. Liu, B. Gao, L. Ouyang, Y. Jin, G. Pozina, I. A. Buyanova, W. M. Chen, O. Inganäs, V. Coropceanu, J.-L. Bredas, H. Yan, J. Hou, F. Zhang, A. A. Bakulin and F. Gao, Design rules for minimizing voltage losses in high-efficiency organic solar cells, *Nat. Mater.*, 2018, **17**, 703–709.

203 X. Kong, N. Yang, X. Zhang, J. Zhang, Z. Li, X. Li, Y. Wu, R. Sun, J. Li, A. Li, J. Min, G. Yang and C. Sun, Suppressed non-radiative loss and efficient hole transfer at a small highest occupied molecular orbital offset endows binary organic solar cells with 19.73% efficiency and a small efficiency-cost gap, *Energy Environ. Sci.*, 2025, **18**, 386–396.

204 C. Sun, F. Pan, S. Chen, R. Wang, R. Sun, Z. Shang, B. Qiu, J. Min, M. Lv, L. Meng, C. Zhang, M. Xiao, C. Yang and Y. Li, Achieving fast charge separation and low nonradiative recombination loss by rational fluorination for high-efficiency polymer solar cells, *Adv. Mater.*, 2019, **31**, 1905480.

205 M. Zhang, X. Guo, W. Ma, S. Zhang, L. Huo, H. Ade and J. Hou, An easy and effective method to modulate molecular energy level of the polymer based on benzodithiophene for the application in polymer solar cells, *Adv. Mater.*, 2014, **26**, 2089–2095.

206 D. Xie, L. Pan, T. Liu, S. Pang, W. Deng, J. Oh, X. Liu, C. Yang, H. Wu and C. Duan, Terpolymers Containing Difluorobenzoxadiazole Enable Suppressed Energy Losses and Optimal Batch-to-Batch Reproducibility for High-Efficiency Organics Solar Cells, *Sol. RRL*, 2023, **7**, 2300182.

207 R. Zeng, S. Xu, J. Deng, S. Tan, G. Zhou, M. Zhang, L. Zhu, F. Han, X. Xue, A. Zhang, H. Tan, L. Zhang, C. Zhu, C. Wang, X. Wu, Z. Fink, T. P. Russell, Y. Zhang and F. Liu, Molecular Precision Engineering for Efficient Binary Organic Photovoltaics through Energy Level and Fibrillar Structure Modulation, *Adv. Energy Mater.*, 2024, **14**, 2401561.

208 H. Zhang, Y. Liu, G. Ran, H. Li, W. Zhang, P. Cheng and Z. Bo, Sequentially Processed Bulk-Heterojunction-Buried Structure for Efficient Organic Solar Cells with 500 nm Thickness, *Adv. Mater.*, 2024, **36**, 5400521.

209 F. Sun, X. Zheng, T. Hu, J. Wu, M. Wan, Y. Xiao, T. Cong, Y. Li, B. Xiao, J. Shan, E. Wang, X. Wang and R. Yang, 1,5-Diiodocycloctane: a cyclane solvent additive that can extend the exciton diffusion length in thick film organic solar cells, *Energy Environ. Sci.*, 2024, **17**, 1916–1930.

210 Z. Ge, J. Qiao, J. Song, X. Li, J. Fu, Z. Fu, J. Gao, X. Tang, L. Jiang, Z. Tang, G. Lu, X. Hao and Y. Sun, Suppressing Trap-Assisted Nonradiative Recombination via Interface Modification for Achieving Efficient Organic Solar Cells, *Adv. Energy Mater.*, 2024, **14**, 2400203.

211 A. Ullah, K. H. Park, Y. Lee, S. Park, A. B. Faheem, H. D. Nguyen, Y. Siddique, K. K. Lee, Y. Jo, C. H. Han, S. Ahn, I. Jeong, S. Cho, B. Kim, Y. S. Park and S. Hong, Versatile hole selective molecules containing a series of heteroatoms as self-assembled monolayers for efficient p-i-n perovskite and organic solar cells, *Adv. Funct. Mater.*, 2022, **32**, 2208793.

212 Q. Wu, J. Zhu and D. Zhao, Progress and prospects for all-perovskite tandem solar cells, *J. Energy Chem.*, 2024, **103**, 90–96.

213 M. Zhang, Z. Ying, X. Li, S. Li, L. Chen, X. Guo, L. Liu, Y. Sun, J. Wu, Y. Zeng, C. Xiao, J. Wu, X. Yang and J. Ye, Hole-selective Transparent In Situ Passivation Contacts for Efficient and Stable n–i–p Graded Perovskite/Silicon Tandem Solar Cells, *Adv. Mater.*, 2025, **37**, 2416530.

214 H. Li, Y. Wang, H. Gao, M. Zhang, R. Lin, P. Wu, K. Xiao and H. Tan, Revealing the output power potential of bifacial

monolithic all-perovskite tandem solar cells, *eLight*, 2022, **2**, 21.

215 Y. Ge, L. Zheng, H. Wang, J. Gao, F. Yao, C. Wang, G. Li, H. Guan, S. Wang, H. Cui, F. Ye, W. Shao, Z. Zheng, Z. Yu, J. Wang, Z. Xu, C. Dai, Y. Ma, Y. Yang, Z. Guan, Y. Liu, J. Wang, Q. Lin, Z. Li, X. Li, W. Ke, M. Grätzel and G. Fang, Suppressing wide-angle light loss and non-radiative recombination for efficient perovskite solar cells, *Nat. Photonics*, 2025, **19**, 170–177.

216 A. Luque and S. Hegedus, *Handbook of photovoltaic science and engineering*, John Wiley & Sons, 2011.

217 X. Ren, Z. Wang, W. E. Sha and W. C. Choy, Exploring the way to approach the efficiency limit of perovskite solar cells by drift-diffusion model, *ACS Photonics*, 2017, **4**, 934–942.

218 J. Frenkel, On the Transformation of Light into Heat in Solids. II, *Phys. Rev.*, 1931, **37**, 1276–1294.

219 H. Li, C. Chen, H. Hu, Y. Li, Z. Shen, F. Li, Y. Liu, R. Liu, J. Chen, C. Dong, S. Mabrouk, R. S. Bobba, A. Baniya, M. Wang and Q. Qiao, Strategies for high-performance perovskite solar cells from materials, film engineering to carrier dynamics and photon management, *InfoMat*, 2022, **4**, e12322.

220 Y. Lin, W. Yang, H. Gu, F. Du, J. Liao, D. Yu, J. Xia, H. Wang, S. Yang, G. Fang and C. Liang, Transparent Recombination Layers Design and Rational Characterizations for Efficient Two-Terminal Perovskite-Based Tandem Solar Cells, *Adv. Mater.*, 2024, **36**, 2405684.

221 Y. Bao, J. Zeng, Y. Xu, G. Xie, H. Hu, X. Lei, D. Wang, J. Zhang, W. Peng, Z. Liu, P. Zhu, G. Qu, L. Qiu, L. Yan, Y. Zhang, X. Wang and B. Xu, Dual-Site Anchors Enabling Vertical Molecular Orientation for Efficient All-Perovskite Tandem Solar Cells, *Adv. Energy Mater.*, 2024, **15**, 2403186.

222 Z. Wu, Y. Zhao, C. Wang, T. Ma, C. Chen, Y. Liu, T. Jia, Y. Zhai, C. Chen, C. Zhang, G. Cao, Z. Yang, D. Zhao and X. Li, Enhancing Photovoltaically Preferred Orientation in Wide-Bandgap Perovskite for Efficient All-Perovskite Tandem Solar Cells, *Adv. Mater.*, 2025, **37**, 2412943.

223 D. Gao, B. Li, Q. Liu, C. Zhang, Z. Yu, S. Li, J. Gong, L. Qian, F. Vanin, K. Schutt, M. A. Davis, A. F. Palmstrom, S. P. Harvey, N. J. Long, J. M. Luther, X. C. Zeng and Z. Zhu, Long-term stability in perovskite solar cells through atomic layer deposition of tin oxide, *Science*, 2024, **386**, 187–192.

224 R. He, W. Wang, Z. Yi, F. Lang, C. Chen, J. Luo, J. Zhu, J. Thiesbrummel, S. Shah, K. Wei, Y. Luo, C. Wang, H. Lai, H. Huang, J. Zhou, B. Zou, X. Yin, S. Ren, X. Hao, L. Wu, J. Zhang, J. Zhang, M. Stolterfoht, F. Fu, W. Tang and D. Zhao, All-perovskite tandem 1 cm2 cells with improved interface quality, *Nature*, 2023, **618**, 80–86.

225 G. Xie, H. Li, J. Fang, X. Wang, H. Peng, D. Lin, N. Huang, L. Gan, W. Li, R. Jiang, T. Bu, F. Huang, S. He and L. Qiu, Crystallization Thermodynamics Regulation of 1.85 eV Wide-Bandgap Perovskite for Efficient and Stable Perovskite-Organic Tandem Photovoltaics, *Angew. Chem., Int. Ed.*, 2025, **64**, e202501764.

226 X. Cui, G. Xie, Y. Liu, X. Xie, H. Zhang, H. Li, P. Cheng, G. Lu, L. Qiu and Z. Bo, Boosting the Efficiency of Perovskite/Organic Tandem Solar Cells via Enhanced Near-Infrared Absorption and Minimized Energy Losses, *Adv. Mater.*, 2024, **36**, 2408646.

227 J. Benduhn, K. Tvingstedt, F. Piersimoni, S. Ullbrich, Y. Fan, M. Tropiano, K. A. McGarry, O. Zeika, M. K. Riede, C. J. Douglas, S. Barlow, S. R. Marder, D. Neher, D. Spoltore and K. Vandewal, Intrinsic non-radiative voltage losses in fullerene-based organic solar cells, *Nat. Energy*, 2017, **2**, 17053.

228 Y. Jiang, K. Liu, F. Liu, G. Ran, M. Wang, T. Zhang, R. Xu, H. Liu, W. Zhang, Z. Wei, Y. Cui, X. Lu, J. Hou and X. Zhu, 20.6% Efficiency Organic Solar Cells Enabled by Incorporating a Lower Bandgap Guest Nonfullerene Acceptor Without Open-Circuit Voltage Loss, *Adv. Mater.*, 2025, **37**, 2500282.

229 S. Qin, C. Lu, Z. Jia, Y. Wang, S. Li, W. Lai, P. Shi, R. Wang, C. Zhu, J. Du, J. Zhang, L. Meng and Y. Li, Constructing Monolithic Perovskite/Organic Tandem Solar Cell with Efficiency of 22.0% via Reduced Open-Circuit Voltage Loss and Broadened Absorption Spectra, *Adv. Mater.*, 2022, **34**, 2108829.

230 D. Wang, H. Cui, G. Hou, Z. Zhu, Q. Yan and G. Su, Highly efficient light management for perovskite solar cells, *Sci. Rep.*, 2016, **6**, 18922.

231 Q. Luo, X. Deng, C. Zhang, M. Yu, X. Zhou, Z. Wang, X. Chen and S. Huang, Enhancing photovoltaic performance of perovskite solar cells with silica nanosphere antireflection coatings, *Sol. Energy*, 2018, **169**, 128–135.

232 X. Wu, D. Zhang, B. Liu, Y. Wang, X. Wang, Q. Liu, D. Gao, N. Wang, B. Li, L. Wang, Z. Yu, X. Li, S. Xiao, N. Li, M. Stolterfoht, Y. H. Lin, S. Yang, X. C. Zeng and Z. Zhu, Optimization of Charge Extraction and Interconnecting Layers for Highly Efficient Perovskite/Organic Tandem Solar Cells with High Fill Factor, *Adv. Mater.*, 2024, **36**, 2410692.

233 X. Liu, L. Chen, Y. Yu, D. He, X. Shai, S. Zhang, Z. Zhang, J. Feng, J. Yi and J. Chen, Advancements of highly efficient perovskite based tandem solar cells, *Sci. China Mater.*, 2024, **68**, 691–708.

234 C. Wang, W. Shao, J. Liang, C. Chen, X. Hu, H. Cui, C. Liu, G. Fang and C. Tao, Suppressing Phase Segregation in Wide Bandgap Perovskites for Monolithic Perovskite/Organic Tandem Solar Cells with Reduced Voltage Loss, *Small*, 2022, **18**, 2204081.

235 R. Wang, J. Zhang, J. Zhao, Y. Wang, Y. Ding, Y. Zhao, X. Zhang and G. Hou, Promoted monolithic perovskite/organic tandem solar cells through elaborate manipulation of light transmission and carrier tunneling in interconnect junction, *Sci. China:Chem.*, 2024, **67**, 3131–3139.

236 Z. Ma, Y. Dong, R. Wang, Z. Xu, M. Li and Z. a. Tan, Transparent Recombination Electrode with Dual-Functional Transport and Protective Layer for Efficient

and Stable Monolithic Perovskite/Organic Tandem Solar Cells, *Adv. Mater.*, 2023, **35**, 2307502.
237 S. Yao, C. Liu, J. Lv, H. Li, C. Gong, Q. Ye, Y. Zhou, R. Dai, X. Hu, Z. Huang and Y. Chen, Efficient and stable perovskite/organic tandem solar cells via molecules-assisted iodine capture under ultraviolet light, *Sci. China:Chem.*, 2025, DOI: **10.1007/s11426-025-2587-9**.
238 C. Li, G. Yao, X. Gu, J. Lv, Y. Hou, Q. Lin, N. Yu, M. S. Abbasi, X. Zhang, J. Zhang, Z. Tang, Q. Peng, C. Zhang, Y. Cai and H. Huang, Highly efficient organic solar cells enabled by suppressing triplet exciton formation and non-radiative recombination, *Nat. Commun.*, 2024, **15**, 8872.
239 W. Miao, Y. Liu, Y. Wu, J. Liang, J. Xiong, T. Hu, Y. He, L. Chen, J. Shan, X. Wang and R. Yang, Energy Disorder Suppression, Charge Transport Channel Establishment by Integrating Four-Arm Donor Molecule for High-Performance Organic Solar Cells, *Adv. Funct. Mater.*, 2025, **35**, 2501143.
240 P. C. Dastoor, C. R. McNeill, H. Frohne, C. J. Foster, B. Dean, C. J. Fell, W. J. Belcher, W. M. Campbell, D. L. Officer, I. M. Blake, P. Thordarson, M. J. Crossley, N. S. Hush and J. R. Reimers, Understanding and improving solid-state polymer/C60-fullerene bulk-heterojunction solar cells using ternary porphyrin blends, *J. Phys. Chem. C*, 2007, **111**, 15415–15426.
241 Y. J. Cheng, C. H. Hsieh, P. J. Li and C. S. Hsu, Morphological stabilization by in situ polymerization of fullerene derivatives leading to efficient, thermally stable organic photovoltaics, *Adv. Funct. Mater.*, 2011, **21**, 1723–1732.
242 B. M. Savoie, S. Dunaisky, T. J. Marks and M. A. Ratner, The Scope and Limitations of Ternary Blend Organic Photovoltaics, *Adv. Energy Mater.*, 2015, **5**, 1400891.
243 Y. Wang, J. Yu, R. Zhang, J. Yuan, S. Hultmark, C. E. Johnson, N. P. Gallop, B. Siegmund, D. Qian, H. Zhang, Y. Zou, M. Kemerink, A. A. Bakulin, C. Mueller, K. Vandewal, X.-K. Chen and F. Gao, Origins of the open-circuit voltage in ternary organic solar cells and design rules for minimized voltage losses, *Nat. Energy*, 2023, **8**, 978–988.
244 S. Yoon, E.-Y. Shin, N.-K. Cho, S. Park, H. Y. Woo and H. J. Son, Progress in morphology control from fullerene to nonfullerene acceptors for scalable high-performance organic photovoltaics, *J. Mater. Chem. A*, 2021, **9**, 24729–24758.
245 Y. Fang, Q. Dong, Y. Shao, Y. Yuan and J. Huang, Highly narrowband perovskite single-crystal photodetectors enabled by surface-charge recombination, *Nat. Photonics*, 2015, **9**, 679–686.
246 G. Yu, J. Gao, J. C. Hummelen, F. Wudl and A. J. Heeger, Polymer photovoltaic cells: enhanced efficiencies via a network of internal donor-acceptor heterojunctions, *Science*, 1995, **270**, 1789–1791.
247 J. Zhu and D. Zhao, All-perovskite tandem solar cells gallop ahead, *The Innovation*, 2023, **4**, 100493.
248 H. Liu, Y. Zhu, W. Xiong, Y. Yang, S. Li and S. Bai, Transparent Conductive Oxide Films and Their Applications in Silicon Heterojunction and Perovskite/Silicon Tandem Photovoltaics, *ACS Appl. Energy Mater.*, 2025, **8**, 4032–4047.
249 E. Aydin, E. Ugur, B. K. Yildirim, T. G. Allen, P. Dally, A. Razzaq, F. Cao, L. Xu, B. Vishal, A. Yazmaciyan, M. Babics, A. Fell, C. Xiao and S. De Wolf, Enhanced optoelectronic coupling for perovskite/silicon tandem solar cells, *Nature*, 2023, **623**, 732–738.
250 M. R. Fitzsimmons, B. Roose, Y. Han, T. Kang, Y.-H. Chiang, C.-S. Huang, Y. Lu, T. C.-J. Yang, C. Chosy, S. Guan, M. Anaya and S. D. Stranks, Optimized Graphene-Oxide-Based Interconnecting Layer in All-Perovskite Tandem Solar Cells, *ACS Energy Lett.*, 2025, **10**, 713–725.
251 R. Lin, K. Xiao, Z. Qin, Q. Han, C. Zhang, M. Wei, M. I. Saidaminov, Y. Gao, J. Xu, M. Xiao, A. Li, J. Zhu, E. H. Sargent and H. Tan, Monolithic all-perovskite tandem solar cells with 24.8% efficiency exploiting comproportionation to suppress Sn (ii) oxidation in precursor ink, *Nat. Energy*, 2019, **4**, 864–873.
252 T. Wu, Z. Huang, L. Li, W. Sun, T. Xue, Q. Pan, H. Xie, S. Chen, L. Guo, J. Chi, H. Wang, Z. Zhang, T. Han, M. Su and Y. Song, Wearable Perovskite-Based Shadow Recognition Sensor for Ambient and Nonobtrusive Human–Computer Interaction, *Adv. Intell. Syst.*, 2023, **5**, 2200307.
253 Z. Huang, J. Long, R. Dai, X. Hu, L. Le, X. Meng, L. Tan and Y. Chen, Ultra-flexible and waterproof perovskite photovoltaics for washable power source applications, *Chem. Commun.*, 2021, **57**, 6320–6323.
254 Z. Chu, B. Fan, W. Shi, Z. Xing, C. Gong, J. Li, L. Li, X. Meng, M. B. K. Niazi, X. Hu and Y. Chen, Synergistic Macroscopic–Microscopic Regulation: Dual Constraints of the Island Effect and Coffee-Ring Effect in Printing Efficient Flexible Perovskite Photovoltaics, *Adv. Funct. Mater.*, 2025, 2424191.
255 X. Meng, Z. Xing, X. Hu, Z. Huang, T. Hu, L. Tan, F. Li and Y. Chen, Stretchable perovskite solar cells with recoverable performance, *Angew. Chem., Int. Ed.*, 2020, **59**, 16602–16608.
256 X. Duan, X. Li, L. Tan, Z. Huang, J. Yang, G. Liu, Z. Lin and Y. Chen, Controlling crystal growth via an autonomously longitudinal scaffold for planar perovskite solar cells, *Adv. Mater.*, 2020, **32**, 2000617.
257 Z. Huang, X. Hu, C. Liu, L. Tan and Y. Chen, Nucleation and Crystallization Control via Polyurethane to Enhance the Bendability of Perovskite Solar Cells with Excellent Device Performance, *Adv. Funct. Mater.*, 2017, **27**, 1703061.
258 X. Hu, Z. Huang, X. Zhou, P. Li, Y. Wang, Z. Huang, M. Su, W. Ren, F. Li, M. Li, Y. Chen and Y. Song, Wearable large-scale perovskite solar-power source via nanocellular scaffold, *Adv. Mater.*, 2017, **29**, 1703236.
259 G. Lee, M.-c. Kim, Y. W. Choi, N. Ahn, J. Jang, J. Yoon, S. M. Kim, J.-G. Lee, D. Kang, H. S. Jung and M. Choi, Ultra-flexible perovskite solar cells with crumpling

durability: toward a wearable power source, *Energy Environ. Sci.*, 2019, **12**, 3182–3191.

260 Z. Jia, X. Guo, X. Yin, M. Sun, J. Qiao, X. Jiang, X. Wang, Y. Wang, Z. Dong, Z. Shi, C.-H. Kuan, J. Hu, Q. Zhou, X. Jia, J. Chen, Z. Wei, S. Liu, H. Liang, N. Li, L. K. Lee, R. Guo, S. V. Roth, P. Müller-Buschbaum, X. Hao, X. Du and Y. Hou, Efficient near-infrared harvesting in perovskite–organic tandem solar cells, *Nature*, 2025, **643**, 104–110.

261 R. Lin, J. Xu, M. Wei, Y. Wang, Z. Qin, Z. Liu, J. Wu, K. Xiao, B. Chen, S. M. Park, G. Chen, H. R. Atapattu, K. R. Graham, J. Xu, J. Zhu, L. Li, C. Zhang, E. H. Sargent and H. Tan, All-perovskite tandem solar cells with improved grain surface passivation, *Nature*, 2022, **603**, 73–78.

262 Y. Miao, M. Ren, Y. Chen, H. Wang, H. Chen, X. Liu, T. Wang and Y. Zhao, Green solvent enabled scalable processing of perovskite solar cells with high efficiency, *Nat. Sustain.*, 2023, **6**, 1465–1473.

263 Z. Yao, Q. Xia, J. Li, X. Meng, Z. Huang, M. B. K. Niazi, S. Zhang, X. Hu and Y. Chen, A Refined Dual-Fiber Network Morphology as Printable Hole Transport Layers for High-Performance Perovskite Solar Mini-Modules, *Aggregate*, 2025, e70017.

264 N.-G. Park and K. Zhu, Scalable fabrication and coating methods for perovskite solar cells and solar modules, *Nat. Rev. Mater.*, 2020, **5**, 333–350.

265 K. Xu, Z. Xing, D. Li, C. Du, Y. Gao, X. Hu, T. Hu and Y. Chen, Boosting Efficiency to 22.73%: Unraveling the Role of Solvent Environment in Low-Dimensional Perovskites Through Competitive Bonding Interactions, *Adv. Funct. Mater.*, 2025, **35**, 2415429.

266 J. Shan, Z. Zhang, J. Zhou, W. Zhang, H. Guan, J. Zhang, Y. Zhang, C. Xiao, M. Yang and Z. Ge, Modulating Crystal Growth with Sacrificial Coordination for High-Performance Perovskite Solar Cells via Intense Pulsed Light Annealing, *Adv. Mater.*, 2025, **37**, 2502710.

267 C. Duan, H. Gao, K. Xiao, V. Yeddu, B. Wang, R. Lin, H. Sun, P. Wu, Y. Ahmed, A. D. Bui, X. Zheng, Y. Wang, J. Wen, Y. Wang, W. Ou, C. Liu, Y. Zhang, H. Nguyen, H. Luo, L. Li, Y. Liu, X. Luo, M. I. Saidaminov and H. Tan, Scalable fabrication of wide-bandgap perovskites using green solvents for tandem solar cells, *Nat. Energy*, 2025, **10**, 318–328.

268 P. Calado, A. M. Telford, D. Bryant, X. Li, J. Nelson, B. C. O'Regan and P. R. F. Barnes, Evidence for ion migration in hybrid perovskite solar cells with minimal hysteresis, *Nat. Commun.*, 2016, **7**, 13831.

269 S. Qu, H. Huang, J. Wang, P. Cui, Y. Li, M. Wang, L. Li, F. Yang, C. Sun, Q. Zhang, P. Zhu, Y. Wang and M. Li, Revealing and Inhibiting the Facet-related Ion Migration for Efficient and Stable Perovskite Solar Cells, *Angew. Chem., Int. Ed.*, 2024, **64**, e202415949.

270 Y. Bao, T. Ma, Y. Zhang, L. Shi, L. Qin, C. Wang, G. Cao, X. Li and Z. Yang, Insight into ion-induced stability degradation in all-perovskite tandem photovoltaics: quantitative characterization and effective manipulation strategies, *Sci. Bull.*, 2025, **70**, 2285–2296.

271 Q. Ye, B. Fan, Y. Zhou, S. Liu, S. Yao, J. Lv, C. Wang, R. Dai, D. Chen, X. Meng, Z. Huang, X. Hu and Y. Chen, Competitive Crystallization Modulated Phase-Homogeneous Wide-Bandgap Perovskites for Monolithic Perovskite-Organic Tandem Solar Cells, *Adv. Mater.*, 2025, e11781.

272 B. Dong, M. Wei, Y. Li, Y. Yang, W. Ma, Y. Zhang, Y. Ran, M. Cui, Z. Su, Q. Fan, Z. Bi, T. Edvinsson, Z. Ding, H. Ju, S. You, S. M. Zakeeruddin, X. Li, A. Hagfeldt, M. Grätzel and Y. Liu, Self-assembled bilayer for perovskite solar cells with improved tolerance against thermal stresses, *Nat. Energy*, 2025, **10**, 342–353.

273 P. Zhu, C. Chen, J. Dai, Y. Zhang, R. Mao, S. Chen, J. Huang and J. Zhu, Toward the commercialization of perovskite solar modules, *Adv. Mater.*, 2024, **36**, 2307357.

274 Z. Huang, X. Hu, Z. Zhao, X. Meng, M. Su, T. Xue, J. Chi, H. Xie, Z. Cai, Y. Chen and Y. Song, Releasing nanocapsules for high-throughput printing of stable perovskite solar cells, *Adv. Energy Mater.*, 2021, **11**, 2101291.

275 F. Li, C. Gong, B. Fan, Z. Xing, X. Meng, S. Zhang, X. Hu and Y. Chen, 3D Network-Assisted Crystallization for Fully Printed Perovskite Solar Cells with Superior Irradiation Stability, *Adv. Funct. Mater.*, 2022, **32**, 2206412.